BRYNTRN: A Baryon Transport Model

John W. Wilson, Lawrence W. Townsend,
and John E. Nealy
Langley Research Center
Hampton, Virginia

Sang Y. Chun, B. S. Hong,
and Warren W. Buck
Hampton University
Hampton, Virginia

S. L. Lamkin
PRC Kentron, Inc.
Aerospace Technologies Division
Hampton, Virginia

Barry D. Ganapol
University of Arizona
Tucson, Arizona

Ferdous Khan and Francis A. Cucinotta
Old Dominion University
Norfolk, Virginia

Summary

This report describes the development of an interaction data base and a numerical solution to the transport of baryons through an arbitrary shield material based on a straight ahead approximation of the Boltzmann equation. The code is most accurate for continuous-energy boundary values but gives reasonable results for discrete spectra at the boundary using even a relatively coarse energy grid (30 points) and large spatial increments (1 cm in H$_2$O). The resulting computer code is self-contained, efficient, and easy to use. The code requires only a very small fraction of the computer resources required for Monte Carlo codes.

1. Introduction

As NASA continues to develop a vigorous space program, tools for the analysis of optimum shielding against space radiation are a continuing requirement. The tools must ultimately account for the very complex mixture of radiations in the space environment and be complete in the physical description of the processes involved. An incomplete model must, by necessity, have restricted capabilities that are not always appreciated at the engineering level and may cause errors in vehicle design. Still, a complete model must be computationally efficient in order to provide a useful tool for design work. In order for the model to be used with confidence, some effort toward model validation must be made.

Space contains the most complicated mixture of diverse radiation components known. When these components interact with materials, many new and varied radiations are produced. This places enormous demands on tools for model development analysis. Furthermore, a common basis for assessing risk from such an environment is in itself a challenge to model development. The model must likewise allow for all potential elemental materials and allow inhomogeneous configurations. The present work is the beginning of this task.

Monte Carlo computer codes have been written that meet many of the above requirements (ref. 1). However, the enormous computational requirements have caused their use to be avoided in the space program. In an earlier report (ref. 2), we presented a relatively complete transport code for high-energy nucleons. The data base for that code was complete but somewhat inaccurate. The purpose of the present report is to describe both the improved computer programs developed for the calculation of the transport and the interaction of high-energy nucleons (baryons) with materials. The methods, based on the direct solution of the Boltzmann equation, have been developed over the last several years (refs. 2 to 5). The present goal is to document a relatively complete description of the basic physical processes and an improved input data base. Future work will concentrate on improving the data base and validating the computational procedures.

2. Theoretical Considerations—The Boltzmann Equation

In moving through bulk material, particles give up energy to the medium through atomic/molecular and nuclear interaction. These processes are described by a Boltzmann-like equation that we use in a time-independent form. The equations in the straight ahead approximation to be solved (ref. 1) are

$$\left[\frac{\partial}{\partial x} - \frac{\partial}{\partial E}S(E) + \sigma_p(E)\right]\phi_p(x,E) = \sum_j \int_E^\infty f_{pj}(E,E')\,\phi_j(x,E')\,dE' \qquad (2.1)$$

$$\left[\frac{\partial}{\partial x} + \sigma_n(E)\right]\phi_n(x,E) = \sum_j \int_E^\infty f_{nj}(E,E')\,\phi_j(x,E')\,dE' \qquad (2.2)$$

$$\left[\frac{\partial}{\partial x} - \frac{\partial}{\partial E}\nu_t\,S(E)\right]\phi_t(x,E) = \sum_j \int_0^\infty f_{tj}(E,E')\,\phi_j(x,E')\,dE' \qquad (2.3)$$

where $\phi_j(x,E)$ is the differential flux density of type j particle at x with energy E; $S(E)$ is the proton stopping power; ν_t is the ion-range scaling parameter; $\sigma_p(E)$ and $\sigma_n(E)$ are proton

\

and neutron total cross sections, respectively; and $f_{ij}(E, E')$ represents the differential cross sections for elastic and nonelastic processes. It is convenient to define new field quantities as

$$r = \int_0^E dE'/S(E') \tag{2.4}$$

$$\psi_j(x, r) = S(E)\,\phi_j(x, E) \tag{2.5}$$

$$\bar{f}_{ij}(r, r') = S(E)\,f_{ij}(E, E') \tag{2.6}$$

so that

$$\left[\frac{\partial}{\partial x} - \frac{\partial}{\partial r} + \sigma_p(r)\right]\psi_p(x, r) = \sum_j \int_r^\infty \bar{f}_{pj}(r, r')\,\psi_j(x, r')\,dr' \tag{2.7}$$

$$\left[\frac{\partial}{\partial x} + \sigma_n(r)\right]\psi_n(x, r) = \sum_j \int_r^\infty \bar{f}_{nj}(r, r')\,\psi_j(x, r')\,dr' \tag{2.8}$$

$$\left[\frac{\partial}{\partial x} - \nu_j\frac{\partial}{\partial r}\right]\psi_t(x, r) = \sum_j \int_0^\infty \bar{f}_{tj}(r, r')\,\psi_j(x, r')\,dr' \tag{2.9}$$

which can be rewritten as integral equations with the boundary at $x = 0$. The following results are given:

$$\psi_p(x, r) = \exp\left[-\int_0^x \sigma_p(r + z)dz\right]\psi_p(0, r + x)$$
$$+ \int_0^x dz \exp\left[-\int_0^z \sigma_p(r + w)\,dw\right]\sum_j \int_{r+z}^\infty \bar{f}_{pj}(r + z, r')\,\psi_j(x - z, r')\,dr' \tag{2.10}$$

$$\psi_n(x, r) = \exp\left[-\sigma_n(r)x\right]\psi_n(0, r)$$
$$+ \int_0^x dz \exp[-\sigma_n(r)z]\sum_j \int_r^\infty \bar{f}_{nj}(r, r')\,\psi_j(x - z, r')\,dr' \tag{2.11}$$

$$\psi_t(x, r) = \int_0^x dz \sum_j \int_0^\infty \bar{f}_{tj}(r + \nu_t z, r')\,\psi_j(x - z, r')\,dr' \tag{2.12}$$

The functions and coefficients of equations (2.1) to (2.12) are presented in the next section.

3. Transport Coefficients

3.1. Stopping Power

In passing through a material, an ion loses the larger fraction of its energy to electronic excitation of the material. Although a satisfactory theory of high-energy, ion-electron interaction is available in the form of Bethe's theory utilizing the Born approximation, an equally satisfactory theory for low energies is not available. Bethe's high-energy approximation to the energy loss per unit path (that is, stopping power) is given as

$$S_e = \frac{4\pi N Z_p^2 Z_t e^4}{mv^2}\left\{\ln\left[\frac{2mv^2}{(1 - \beta^2)I_t}\right] - \beta^2 - \frac{C}{Z_t}\right\} \tag{3.1.1}$$

where Z_p is the projectile charge, N is the number of target molecules per unit volume, Z_t is the number of electrons per target molecule, m is the electron mass, v is the projectile velocity,

2

$\beta = v/c$, c is the velocity of light, C is the velocity-dependent shell correction term (ref. 6), and I_t is the mean excitation energy given by

$$Z_t \ln(I_t) = \sum_n f_n \ln(E_n) \tag{3.1.2}$$

where f_n represents the electric dipole oscillator strengths of the target and E_n represents the corresponding excitation energies. Note that the sum in equation (3.1.2) includes discrete and continuum levels. Empirically, it has been observed that molecular stopping power is reasonably approximated by the sum of the corresponding empirically derived "atomic" stopping powers for which equations (3.1.1) and (3.1.2) imply that

$$Z \ln(I) = \sum_j n_j Z_j \ln(I_j) \tag{3.1.3}$$

where Z and I pertain to the molecule, Z_j and I_j are the corresponding atomic values, and n_j represents the stoichiometric coefficients. This additive rule (eq. (3.1.3)) is usually called Bragg's rule (ref. 7).

Sources of deviations from Bragg's additive rule for molecules and for the condensed phase are discussed by Platzman (ref. 8). Aside from shifts in excitation energies and adjustments in line strengths as a result of molecular bonding, new terms in the stopping power appear to be due to coupling between vibrational and rotational modes. Additionally, in the condensed phase, some discrete transitions are moved into the continuum, and collective modes among valence electrons in adjacent atoms produce new terms in the absorption spectrum that must be considered. It is usually assumed that the experimentally observed additive rule shows that molecular stopping power is the sum of atomic processes. In contrast, Platzman proposes that molecular bond shifts for covalent bonded molecules are relatively independent of the molecular combination, thus resulting in an additive rule. On the basis of such arguments, Platzman suggested that ionic bonded substances should be studied as a rigid test of the additive rule because of the radical difference in bonding type. He further estimated that ionic bond shifts could change the stopping power by as much as 50 percent. Recent results of molecular bond shifts on mean excitation energies are discussed in references 9 to 11. Effects of the physical state have likewise been studied (ref. 12).

The electronic stopping power for protons is adequately described by equation (3.1.1) for energies above 500 keV for which the shell or "tight binding" correction C makes an important contribution below 10 MeV (ref. 13). For proton energies below 500 keV, charge exchange (electron transfer) reactions alter the proton charge over much of its path, so that equation (3.1.1) is to be understood in terms of an average over the proton charge states. Normally, an average over the charge states is introduced into equation (3.1.1) so that the effective charge is the root-mean-square ion charge and not the average ion charge. At any ion energy, charge equilibrium is established very quickly in all materials. Utilizing the effective charge in equation (3.1.1) appears to make only a modest improvement below 500 keV, an indication presumably of the failure of this theory based on an empirical basis (refs. 13 and 14). We have utilized empirical fits to the proton data; the resultant stopping power for protons in water is shown in comparison with the evaluated data to Bichsel (ref. 15) in figure 1.

The electronic stopping power for alpha particles requires terms in equation (3.1.1) of higher order in the projectile charge Z_p resulting from corrections to the Born approximation. The alpha stopping power cannot be related to the proton stopping power through the effective charges. Parametric fits to experimental data are given by Ziegler in reference 16 for all elements in both the gaseous and condensed phases.

The electronic stopping power for heavier ions is related to the alpha stopping power through the corresponding effective charges. The effective charge suggested by Barkas (ref. 17) is used:

$$Z^* = Z_p \left[1 - \exp\left(-125\beta / Z_p^{2/3} \right) \right] \tag{3.1.4}$$

where Z_p in equation (3.1.4) is the atomic number of the ion.

At sufficiently low energies, the energy lost by an ion in a nuclear collision becomes important. The nuclear stopping theory used in this paper is a modification of the theory of Lindhard, Scharff, and Schiott (ref. 18). The reduced energy (dimensionless) is given as

$$\epsilon = \frac{32.53 A_p A_t E}{Z_p Z_t (A_p + A_t) \left(Z_p^{2/3} + Z_t^{2/3} \right)^{1/2}} \tag{3.1.5}$$

where E is in units of keV/nucleon and A_p and A_t are the atomic masses of the projectile and target, respectively. The nuclear stopping power S_n in reduced units (ref. 16) is

$$S_n = \begin{cases} 1.59\epsilon^{1/2} & (\epsilon < 0.01) \\ \frac{1.7\epsilon^{1/2} \ln(\epsilon + e^1)}{1 + 6.8\epsilon + 3.4\epsilon^{3/2}} & (0.01 < \epsilon < 10) \\ \frac{\ln(0.47\epsilon)}{2\epsilon} & (10 < \epsilon) \end{cases} \tag{3.1.6}$$

and the conversion factor f to units of eV/10^{15} atoms/cm^2 is

$$f = \frac{8.426 Z_p A_t A_p}{(A_p + A_t) \left(Z_p^{2/3} + Z_t^{2/3} \right)^{1/2}} \tag{3.1.7}$$

The total stopping power S_j is obtained by summing the electronic and nuclear contributions. Other processes of energy transfer such as Bremsstrahlung and pair production are unimportant.

For energies above a few MeV/nucleon, Bethe's equation is adequate provided that appropriate corrections to Bragg's rule (refs. 9 to 11), shell corrections (refs. 6, 13, and 14), and an effective charge are included. Electronic stopping power for protons is calculated from the parametric formulas of Andersen and Ziegler (ref. 13). The calculated stopping power for protons above a few MeV in water is shown in figure 1 in comparison with data given by Bichsel (ref. 15).

Because alpha stopping power is not derivable from the proton stopping power formula using the effective charge at low energy, the parametric fits to empirical alpha stopping powers given by Ziegler (ref. 16) are used. Applying his results for condensed-phase water poorly represented the data of references 19 and 20. Considering that physical state and molecular binding effects are most important for hydrogen (ref. 9), the water stopping power was approximated by using the condensed-phase parameters for hydrogen and the gas-phase parameters for oxygen (which are known experimentally). These results are compared with experimental data for condensed-phase water (refs. 19 and 20) in figure 1. It appears that Ziegler overestimated the condensed-phase effects for oxygen, since the gas-phase oxygen data gave satisfactory results as seen in figure 1.

Electronic stopping powers for ions with a charge greater than 2 are related to the alpha stopping power through the effective charge given by equation (3.1.4). For water, the condensed-phase formula of Ziegler for alpha particles gives probably the best stopping powers for heavier ions. Calculated results for ^{16}O and ^{56}Fe ions in water are shown in figure 1 in comparison with the Northcliffe and Schilling data (ref. 21). Good agreement with Northcliffe and Schilling for ^{56}Fe ions is especially important since their data seem to agree with the range experiments of J. H. Chan in Lexan material, a polycarbonate resin developed by The General Electric Company (ref. 22). The stopping powers in Lexan resin and tissue-equivalent material can be calculated in a way similar to the procedure given above for calculating the stopping powers in water.

4

Although the above methods are the best yet available, they do not adequately represent the data at all energies and elements. The energy loss per unit path length is given by

$$S_e = \frac{4\pi N Z_p^2 Z_t e^4}{mv^2} B \qquad (3.1.8)$$

where an approximate representation of true stopping number B is given in the braces of equation (3.1.1). The determination of S_e then rests upon the accurate knowledge of the mean excitation energy I_t and the shell corrections C. In practice, one invokes some sort of parameter fitting involving the experimental data on stopping power and the quantities I_t and C.

We have recently initiated a different approach of calculating the stopping power of atoms. The main thrust of this approach is to calculate exactly, in the context of the Born approximation and nonrelativistic wave functions, the stopping number B with no assumptions such as those underlying the Bethe theory leading to equation (3.1.1). Thus, the knowledge of B would rest on knowing the radial integrals for the process of excitation as well as ionization when a projectile passes through matter. To the best of our knowledge, this approach seems not to have been tried even for the helium atom. We have recently calculated the radial integral for the optically allowed transitions in the He atom and helium-like ions using the screened hydrogenic model. The model describes the atom by single-particle hydrogenic wave functions and treats the initial state and the final state by two different, effective charge parameters Z_i and Z_f, respectively. The model is able to reasonably reproduce the existing dipole oscillator strength values with little effort, and nonrelativistic numerical values for bound-bound and for bound-continuum transitions are available for many target helium-like ions. The model has also been successful in reproducing the known dipole polarizability values and in predicting the other unknown values. Once the radial integral is evaluated for all momentum transfers, it is an easy matter to obtain the stopping power of the helium atom for a projectile such as a proton or a heavy ion. The same approach then could be extended to include other atoms.

This approach is an ambitious undertaking but is more satisfying in that the calculations are made directly for each atom, thereby avoiding the inherent approximations underlying the Bethe equation (3.1.1). Thus, the calculations do not involve the apparent fittings involving parameters such as I_t and C. Furthermore, the ejected electron distribution in energy and angle as well as the atom excitation spectrum should also be available through this approach.

3.2. Total Nuclear Cross Sections

After many decades of experimental activity at various accelerators with ever-increasing energies, the cross sections for two-nucleon interactions are reasonably well-defined. Although recent advances in the theory of the two-nucleon interaction in terms of phenomenological meson exchange models (ref. 23) show considerable success, a simple parameterization of the experimental data is sufficient for our purposes. For $E \geq 25$ MeV, the proton-proton (pp) total cross section (mb) is found to be reasonably approximated by

$$\sigma_{pp}(E) = \left(1 + \frac{5}{E}\right)\left\{40 + 109\cos(0.199\sqrt{E})\exp\left[-0.451(E - 25)^{0.258}\right]\right\} \qquad (3.2.1)$$

and for lower energies, by

$$\sigma_{pp}(E) = e^{6.51e^{-(E/134)^{0.7}}} \qquad (3.2.2)$$

These forms are compared with experiments (ref. 24) in figure 2. For $E \geq 0.1$ MeV, the neutron-proton (np) cross section is taken as

$$\sigma_{np}(E) = 38 + 12\,500\exp\left[-1.187(E - 0.1)^{0.35}\right] \qquad (3.2.3)$$

and at lower energies, by

$$\sigma_{np}(E) = 26\,000e^{-(E/0.282)^{0.3}} \qquad (3.2.4)$$

These forms are compared with experiments (ref. 24) in figure 3.

The low-energy, neutron-nucleus total cross sections exhibit a complicated fine-resonance structure over a broad, slowly varying background. This background is marked by very broad Ramsauer resonances that persist even to neutron energies of 100 MeV. Although a simple fundamental theory for the Ramsauer resonances is not available, a semiempirical formalism is given by Angeli and Csikai (refs. 25 and 26). Their formalism starts with the usual partial-wave expansion as

$$\sigma_t = 2\pi\lambda^2 \sum_\ell (2\ell + 1)[1 - \mathrm{Re}(\eta_\ell)] \tag{3.2.5}$$

with

$$\eta_\ell = e^{i\delta_\ell} \tag{3.2.6}$$

where δ_ℓ is the complex phase shift for the ℓth partial wave and $\mathrm{Re}(Z)$ denotes the real part of Z. In the opaque nucleus model, the fact that $n_\ell \approx 1$ for all values of $\ell > R/\lambda$, where R is the nuclear radius, leads Angeli and Csikai to assume that

$$\sigma_t \approx 2\pi(R + \lambda)^2[1 - \mathrm{Re}(\eta)] \tag{3.2.7}$$

where $\eta = 0$ gives the usual, opaque nucleus result such that

$$\mathrm{Re}(\eta) = e^{-\mathrm{Im}(\delta)} \cos[\mathrm{Re}(\delta)]$$

$$\equiv p \cos\left(qA_t^{1/3} - r\right) \tag{3.2.8}$$

is a reasonable starting point to parameterize the total cross sections, where $\mathrm{Im}(\delta)$ denotes the imaginary part of δ. Their complete parameterization is

$$\sigma_t = 2\pi(r_0 A_t^{1/3} + \lambda)^2[a - p\cos(qA_t^{1/3} - r)] \tag{3.2.9}$$

where $r_0 = 1.4$ fm, and the neutron wavelength is

$$\lambda = \frac{4.55}{\sqrt{E}}\frac{A_t + 1}{A_t} \tag{3.2.10}$$

The parameters of Angeli and Csikai are adequately approximated by

$$a = \frac{1}{1 + [2/(3.8E + 0.1E\sqrt{E} + 0.1E^3\sqrt{E})]} \tag{3.2.11}$$

$$p = 0.15 - 0.0066\sqrt{E} \tag{3.2.12}$$

$$q = 2.72 - 0.203\sqrt{E} \tag{3.2.13}$$

$$r = \min\{-5.3 + 1.66\sqrt{E}; 1.3\} \tag{3.2.14}$$

Strictly speaking, equations (3.2.9) to (3.2.14) apply only to $A_t \geq 40$ and $0.5 \leq E \leq 40$ MeV. A simple extension to all values of A_t and $0.1 \leq E \leq 100$ MeV gives qualitatively similar results to the experimental data and provides a starting point to representing the total cross section. The cross sections given by equations (3.2.9) to (3.2.14) are shown in figure 4. This should be compared with the experimental data (ref. 27) shown in figure 5. Note that the data in figure 5 have only the broad resonances shown. The very narrow resonances have been averaged. We now seek some modification to the Angeli-Csikai cross sections to better approximate the total cross sections.

Our modifications to the Angeli-Csikai formalism are as follows:

1. If $A_t > 75$, then a is taken as 0.18 for values of equation (3.2.11) less than 0.18.

2. The value of p is taken to be greater than $0.4a$ unless $A_t > 76$ for which p can be as small as $0.3a$.

3. A modifying factor of $1 + De^{-\alpha E}$ is used with

$$D = \begin{cases} 0.5 & (145 < A_t < 235) \\ 1.0 & (\text{Otherwise}) \end{cases}$$

and

$$\alpha = \begin{cases} 1.0 & (205 < A_t < 235) \\ 2.0 & (\text{Otherwise}) \end{cases}$$

4. An additional modifying factor is applied as

$$F_1 \left\{ 1 - 0.5 \exp\left[-(A_t - 63.54)^2/20 \right] \right.$$

$$\left. - 0.45 \exp\left[-(A_t - 58.71)^2/4 \right] \exp(-2E) + F_2 \right\}$$

where

$$F_1 = \begin{cases} 0.7 & (A_t \le 63; E \le 0.8) \\ 1.0 & (\text{Otherwise}) \end{cases}$$

$$F_2 = \begin{cases} 0 & (E > 0.5) \\ -4.95 e^{-18E} & (40 \le A_t < 42) \\ -1.79 e^{-15E} & (32 \le A_t < 34) \end{cases}$$

5. If $A_t < 30$, then numerical interpolation between experimental values is used.

The final cross sections as modified above are shown in figure 6 and should be compared with figure 5.

The total cross sections above 100 MeV have been taken from reference 28. The high-energy cross sections of reference 28 have been approximated by

$$\sigma_{\text{tot}}(A_t, E) = 52.5 A_t^{0.758} \left[1 + (0.8 + 2.4 e^{-A_t/30}) e^{-E/135} \sin \Theta_E \right] \tag{3.2.15}$$

where the phase angle is given by

$$\Theta_E = \begin{cases} 14.41 & (E \le 40 \text{ MeV}) \\ 1.29 \ln^2(E) - \pi & (E > 40 \text{ MeV}) \end{cases} \tag{3.2.16}$$

The expressions (3.2.15) and (3.2.16) are shown in comparison with the theory of Townsend, Wilson, et al. (ref. 28) and a compilation of experiments in figures 7 to 10. Equations (3.2.9) to (3.2.14) are connected smoothly at 70 MeV to the results of equations (3.2.15) and (3.2.16) at 130 MeV with an assumed exponential dependence on energy. The total cross section is used to calculate the scattering cross section as

$$\sigma_s(E) = \sigma_{\text{tot}}(E) - \sigma_{\text{abs}}(E) \tag{3.2.17}$$

The total (tot) neutron-nucleus cross section is shown in comparison with experimental data (ref. 27) in figures 11 to 14. (Experimental data are shown as the dashed curve.) Also shown are the cross sections (listed as "prior") used in reference 2. Clearly, the present result is a great improvement.

3.3. Nuclear-Absorption Cross Sections

Qualitatively, the nuclear-absorption cross sections show an energy dependence similar to that observed for the total nuclear cross sections. An analytic formula for protons was derived

by Letaw et al. (ref. 29) by first fitting the cross sections of Bobchenko et al. (ref. 30) with the formula

$$\sigma_A = 45A_t^{0.7}\{1 + 0.016\sin[5.3 - 2.63\ln(A_t)]\} \tag{3.3.1}$$

where A_t is the mass number of the target nucleus. Equation (3.3.1) reproduces the Bobchenko data to within ± 2 percent (ref. 29). A somewhat better fit to the Bobchenko data is given by

$$\sigma_A = 45A_t^{0.7}(1 - 0.018\sin\Theta_A) \tag{3.3.2}$$

where the angle Θ_A is

$$\Theta_A = 2.94\ln(A_t) + 0.63\sin[3.92\ln(A_t) - 2.329] - 0.176 \tag{3.3.3}$$

Equation (3.3.2) fits the Bobchenko data to within the 1.2-percent difference, which is on the order of the quoted experimental uncertainty (ref. 30). Although the Bobchenko data represent a consistent set of measurements for many different targets and probably define well the A-dependence of the high-energy cross sections, they may nonetheless be in error in absolute value as suggested by many other independent experiments (refs. 31 and 32).

Letaw et al. (ref. 29) assume the energy dependence for all nuclei to be the same and to be approximated by

$$f(E) = 1 - 0.62e^{-E/200}\sin(10.9E^{-0.28}) \tag{3.3.4}$$

where the nucleon kinetic energy is in units of MeV. We observe oscillations according to the quantum-mechanical calculations of Townsend and Wilson (ref. 31) with phase angle

$$\Theta_E = \left\{ \begin{matrix} 1.44 & (E < 25 \text{ MeV}) \\ 1.33\ln(E) - 2.84 & (\text{Otherwise}) \end{matrix} \right\} \tag{3.3.5}$$

but with an A-dependent amplitude given by

$$f(E) = 1(0.3E^{-0.22} + 0.76e^{-E/135})(0.4 + 0.9e^{-A_t/30})\sin\Theta_E \tag{3.3.6}$$

The absorption cross section as given by equations (3.3.3), (3.3.5), and (3.3.6) is shown in comparison with the fit of Letaw et al. and experimental results in figures 15 to 19. As one can see from the figures, it is difficult to assign a figure of merit to the fit, since great scatter in the data obscures the result. Generally, above 20 MeV the results are on the order of ± 10 percent accurate as estimated from the scatter in the experiments.

Below 20 MeV, the neutron cross sections are represented by numerical data sets at discrete energies of 1, 3, 5, 10, 14, and 20 MeV as taken from references 27, 32, and 33. Interpolated values between data points at the available target masses are shown in figures 20 to 25. Intermediate energy values are found according to

$$\sigma(A_t, E) = \sigma(A_t, E_i)e^{-a(E-E_i)} \tag{3.3.7}$$

where E_i and a are taken according to the appropriate subinterval. The cross sections are assumed to be zero at energies below 0.5 MeV. The absorption cross sections for elements from lithium to plutonium for energies between 1 and 100 MeV are displayed in figure 26.

3.4. Fragmentation Cross Sections

The local distribution of ions and radicals produced in ionizing radiation events is known to be an indicator of biological response. The fact that such distributions for high-energy nuclear radiation are vastly altered by local nuclear-reaction events has been studied in nuclear emulsion (refs. 34 and 35) and is a regular component in risk assessments in high-energy neutron and proton radiation fields (refs. 36 and 37). Risk assessments have generally depended on the

8

results of calculational models of these reactions, since the detailed study of such reactions was largely inaccessible to experimental study until the advent of high-energy, heavy ion beams.

The first detailed, relativistic, heavy ion beam experiments were performed by the Heckman group at the Lawrence Berkeley Laboratory (LBL) (refs. 38, 39, and 40) in which beams of carbon and oxygen were fragmented on a series of targets ranging from hydrogen to lead. The momentum distribution of the projectile fragments relative to the projectile rest frame was measured for all the isotopes produced. These results will be analyzed to ascertain relevant biological factors with their corresponding implications on radiation-risk assessment in high-energy, nucleonic radiation fields. An ion fragmentation model will be recommended for use in radiological protection and studies.

Individual nuclear constituents are ejected in the collision of high-energy neutrons and protons by direct collision (ref. 41). The remaining nuclear structure is left in an excited state that seeks an equilibrium minimum-energy configuration through particle emission (ref. 42). This is the basis of Rudstam's study of the systematics of spallation products produced in such collisions in which he assumes that the resultant isotopes are distributed in a bell-shaped distribution near the nuclear stability line. The total change in nuclear mass and the dependence on the incident projectile energy are treated empirically in Rudstam's formalism.

The fragment charge distribution for a given fragment mass A_f is given as

$$f(Z_f) = \exp(\rho A_f - r|Z_f - sA_f + vA_f^2|) \tag{3.4.1}$$

where the coefficients show a slight energy and fragment-mass dependence as

$$r = 11.8 A_f^{-0.45} \tag{3.4.2}$$

$$s = 0.486 \tag{3.4.3}$$

$$v = 3.8 \times 10^{-4} \tag{3.4.4}$$

$$\rho = \left\{ \begin{array}{ll} 20E^{-0.77} & (E < 2100\,\text{MeV}) \\ 0.056 & (E \geq 2100\,\text{MeV}) \end{array} \right\} \tag{3.4.5}$$

where E is the nucleon energy. The complete Rudstam cross section is given by

$$\sigma(A_f, Z_f) = \left[F_1 F_2 \rho A_t^{-0.3} f(Z_f) \right] / D \tag{3.4.6}$$

where

$$D = 1.79 \left[e^{\rho A_t} \left(1 - \frac{0.3}{\rho A_t} \right) - \frac{0.3}{A_t} + \frac{0.3}{\rho A_t} \right] \tag{3.4.7}$$

$$F_1 = 5.18 \exp(-0.25 + 0.0074 A_t) \tag{3.4.8}$$

$$F_2 = \left\{ \begin{array}{ll} \exp(1.73 - 0.0071E) & (E < 240\text{ MeV}) \\ 1 & (E \geq 240\text{ MeV}) \end{array} \right\} \tag{3.4.9}$$

We have applied a simple mass-dependent correction factor to Rudstam's formula as shown in table 3.4.1 and renormalized his cross sections to the total absorption cross section. Many corrective factors have been added to Rudstam's formalism by Silberberg, Tsao, et al. (ref. 43). Estimates have also been made by Guzik (ref. 44) for some of the isotopes produced in connection with cosmic-ray propagation studies with some attempts at experimental verification (ref. 45).

From a nuclear-model point of view, isotope production at low energy results from the formation of a compound nuclear state that decays through particle emission. At higher energies, the direct ejection of particles from the nucleus becomes important, and intranuclear

cascades represented as sequences of two body scatterings within the nucleus with Pauli blocking are the usual means of evaluation (refs. 46 and 47). Subsequent to the cascade, the residual nucleus is assumed to be in thermal equilibrium and seeks to minimize its internal energy through particle emission (ref. 46).

The measurement of isotope-production cross sections at proton accelerators does not allow the direct observation of the fragment products. Customary measurements used $\dot{\gamma}$ or β counting techniques to identify the isotopes produced. Stable and short-lived isotopes produced in the reactions were either not observed or their number was greatly distorted by loss through decay. This is particularly true for light-mass targets such as those that are important to biological health considerations. Consequently, the fragmentation of carbon and oxygen nuclei by protons remained shrouded in experimental obscurity until the advent of heavy ion accelerators.

One of the earliest experiments performed at the LBL Bevatron, when the ions of carbon and oxygen could be accelerated to relativistic energies, used detectors able to measure the energy and charge of an ion beam in conjunction with a bending magnet for momentum analysis (ref. 38). In this way, the density in phase space was measured for each isotope produced in collision with a fixed target.

The isobar cross sections (σ_{LBL}) measured by Lindstrom et al. (ref. 40) for 2.1A GeV oxygen fragmentation on hydrogen targets are given in table 3.4.2 in comparison with the results of Bertini (ref. 47), Rudstam (ref. 42), and Silberberg, Tsao, et al. (ref. 43). Note that the Rudstam results contain the correction factors in table 3.4.1 and are renormalized as described above.

The oxygen-fragmentation cross sections as represented by three parametric forms are shown in figures 27 to 31 in comparison with the Bertini results and various experiments. The baryon-15 isobaric cross sections in figure 27 show that experiments favor the curve of Silberberg, Tsao, et al. Although the Bertini model provides an overestimate, the other parametric curves provide improved estimates compared with the Bertini code. The baryon-14 isobaric experimental cross sections are in reasonable agreement with the three parametric curves as well as with the Bertini model as seen in figure 28. Again, the experiments show no clear advantage of one parametric curve over another for the baryon-13 cross section as seen in figure 29, although the Bertini results appear somewhat low. We show experimental results for baryon numbers between 9 and 13 of Lindstrom et al. in table 3.4.2. Clearly, the equally good agreement for the Rudstam parameterization and the Silberberg, Tsao, et al. parameterization is obtained by baryon numbers 12, 11, and 10. The Bertini cross section is far too low to represent the cross section for baryon-11. The baryon-9 cross sections are shown in figure 30. (The results of Yiou are reported in ref. 45.) The Silberberg, Tsao, et al. parameterization is too high by a factor of 2 or more. The baryon-7 cross sections are shown in figure 31. At energies below 300 MeV, the baryon-7 results of Silberberg, Tsao, et al. are favored.

The measurements of Lindstrom et al. (ref. 40) for relativistic carbon beams are shown in comparison with the results from Rudstam (ref. 42) and Silberberg, Tsao, et al. (ref. 43) in table 3.4.3 for two beam energies. The good agreement with the results of Silberberg, Tsao, et al. is no surprise, since their parameterization was fit to these experimental data sets. Note, however, that the Silberberg, Tsao, et al. cross section for mass 8 fragments needs to be suppressed.

3.5. Differential Nuclear Cross Sections

3.5.1. Nucleon-nucleon spectrum. The nucleon-nucleon differential cross sections are represented (ref. 48) by

$$f(E, E') = B \left[e^{-B(E'-E)} + e^{-BE} \right] \Big/ \left(1 - e^{-BE'} \right) \qquad (3.5.1)$$

where

$$B = 2mc^2 b/10^6 \qquad (3.5.2)$$

10

In the above equation, mc^2 is the nucleon rest energy (938 MeV) and b is the usual slope parameter, given by (in units of GeV^{-2})

$$b = \left\{ \begin{array}{ll} 3 + 14e^{-E'/200} & \text{(For } pp) \\ 3.5 + 30e^{-E'/200} & \text{(For } np) \end{array} \right\} \tag{3.5.3}$$

where E' is the initial nucleon energy in the rest frame of the target. The differential spectrum is defined (nonrelativistically) over the energy interval $0 \leq E \leq E'$. Note that the expression (3.5.1) reduces to the usual result for low-energy scattering:

$$f(E, E') \approx 1/E' \tag{3.5.4}$$

The forward-to-backward scattering ratio is required for neutron scattering and is given by (ref. 46)

$$F_B(E') = 0.12 - 0.015E' + 0.41 \Big/ \left[1 + e^{4(E'-1.2)} \right] \tag{3.5.5}$$

where E' in equation (3.5.5) is the laboratory energy (in GeV) before collision.

The differential cross sections are normalized such that

$$\frac{d\sigma}{dE} = \sigma(E')f(E, E') \tag{3.5.6}$$

where $\sigma(E')$ is the "appropriate" nucleon-nucleon total cross section. Obviously, we have neglected the inelastic processes that must yet be included so that $\sigma(E')$ in equation (3.5.6) is set equal to the total cross section to ensure particle conservation. The center of the mass angular distributions θ_{cm} is related to the energy change in the laboratory system by

$$\frac{d\sigma}{d\Omega} = \frac{E'}{4\pi} \frac{d\sigma}{dE} \tag{3.5.7}$$

(where Ω denotes a solid angle) and is compared with the compilation of experimental data (ref. 49) in figures 32 and 33. These comparisons indicate that the present functions are reasonable.

3.5.2. Nucleon-nucleus spectrum.
The nucleon-nucleus differential cross section in Chew's form of the impulse approximation (note that this is just the Born term of the optical model in ref. 50) is given by

$$\begin{aligned} \frac{d\sigma}{dq^2} &= ce^{-2bq^2} |F_A(q^2)|^2 \\ &\approx ce^{-2bq^2} e^{-2a^2q^2/3} \end{aligned} \tag{3.5.8}$$

where b is the slope parameter of equation (3.5.2) averaged among nuclear constituents, q is the magnitude of momentum transfer, and a is the nuclear root-mean-square (rms) radius. The nuclear rms radius (ref. 50) in terms of the rms charge radius (in fermi) is given as

$$a = \left(\sqrt{a_c^2 - 0.64} \right)^{1/2} \tag{3.5.9}$$

where the rms charge radius (in fermi) is

$$a_c = \begin{cases} 0.84 & (A_t = 1) \\ 2.17 & (A_t = 2) \\ 1.78 & (A_t = 3) \\ 1.63 & (A_t = 4) \\ 2.4 & (6 \le A_t \le 14) \\ 0.82 A_t^{1/3} + 0.58 & (A_t \ge 16) \end{cases} \qquad (3.5.10)$$

The nuclear form factor is the Fourier transform of the nuclear matter distribution. Note that the above equation assumes that the nuclear-matter distribution is a Gaussian function. Such an approximation is reasonable for the light-mass nuclei but is less valid for $A_t \gg 20$.

The energy transferred to the nucleus E_t is restricted by kinematics to

$$0 \le E_t \le (1 - \alpha)E' \qquad (3.5.11)$$

where

$$\alpha = (A_t - 1)^2 / (A_t + 1)^2 \qquad (3.5.12)$$

The energy-transfer spectrum is given as

$$f(E_t, E') = \frac{4 A_t mc^2 (B + \frac{a^2}{3}) \exp\left[-4 A_t mc^2 (B + \frac{a^2}{3}) E_t\right]}{1 - \exp\left[-4 A_t mc^2 (1 - \alpha)(B + \frac{a^2}{3}) E'\right]} \qquad (3.5.13)$$

Similarly, the nucleon energy after scattering E is restricted to

$$\alpha E' \le E \le E' \qquad (3.5.14)$$

The nucleon spectrum is given by

$$f(E, E') = \frac{4 A_t mc^2 (B + \frac{a^2}{3}) \exp\left[-4 A_t mc^2 (B + \frac{a^2}{3})(E' - E)\right]}{1 - \exp\left[-4 A_t mc^2 (1 - \alpha)(B + \frac{a^2}{3}) E'\right]} \qquad (3.5.15)$$

One should note that both equations (3.5.13) and (3.5.15) reduce to the usual isotropic scattering result at low incident energy. The differential spectrum is normalized as

$$\frac{d\sigma_s}{dE} = \sigma_s(E') f(E, E') \qquad (3.5.16)$$

where $\sigma_s(E')$ is the total scattering cross section obtained from equation (3.2.16).

The results of equation (3.5.16) are compared with experiment (refs. 51 and 52) in figures 34 to 37 (where θ_{lab} is the scattering angle in the laboratory). The comparison is rather good at the small angles when considering the simplicity of the present results. Also, shown in the figures are prior results from reference 2 showing considerable improvement in representing forward-scattered neutrons over the prior results. Much of the present discrepancy near forward scattering is due to errors in $\sigma_s(E)$ to which the present spectra are normalized in equation (3.5.16). At broader angles, additional differences are due to the neglect of higher-order corrections to the impulse term.

3.5.3. Nucleon nonelastic spectrum.

The nonelastic differential cross sections (the inelastic process in which the nucleus is raised to an excited level that is ignored) use the results

of Bertini's MECC-7 program (ref. 47). The nucleon multiplicities are given in tables 3.5.1 and 3.5.2. We have required the multiplicities to be monotonic in energy, and thus the values in parentheses, which were obtained by scaling from lower and higher energies, are correct values and are used in the calculations. The results below 400 MeV were taken from Alsmiller et al. (ref. 53), and the results for carbon, calcium, bromine, cesium, and holmium above 400 MeV are obtained by interpolation. The nonelastic spectra are represented as

$$f(E, E') = \sum_{i=1}^{3} \frac{N_i}{\alpha_i} \frac{e^{-E'/\alpha_i}}{1 - e^{-E'/\alpha_i}} + \frac{N_Q}{E' \left[1 + e^{-20(1-E/E')}\right]} \tag{3.5.17}$$

The first term of the summation represents the evaporation peak so that N_1 (the number of evaporation nucleons) is taken from table 3.5.1 and the spectral parameter α_1 (in GeV) is taken from Ranft (ref. 54) as

$$\alpha_{1p} = \left\{ \begin{array}{ll} (0.019 + 0.0017E')(1 - 0.001A_t) & (E' < 5\,\text{GeV}) \\ 0.027(1 - 0.001A_t) & (E' \geq 5\,\text{GeV}) \end{array} \right\} \tag{3.5.18}$$

$$\alpha_{1n} = \left\{ \begin{array}{ll} (0.017 + 0.0017E')(1 - 0.001A_t) & (E' < 5\,\text{GeV}) \\ 0.023(1 - 0.001A_t) & (E' \geq 5\,\text{GeV}) \end{array} \right\} \tag{3.5.19}$$

The second term is taken from Ranft (ref. 54) to represent the low-energy cascade particles as

$$n_{2p} = \left\{ \begin{array}{ll} 0.0035\sqrt{A_t} & (E' \leq 0.1\,\text{GeV}) \\ 0.007\sqrt{A_t}[0.5 + (1 + \log_{10} E')^2] & (0.1 < E' < 5\,\text{GeV}) \\ 0.0245\sqrt{A_t} & (E' \geq 5\,\text{GeV}) \end{array} \right\} \tag{3.5.20}$$

$$n_{2n} = \left\{ \begin{array}{ll} 0.0042\sqrt{A_t} & (E' \leq 0.1\,\text{GeV}) \\ 0.007\sqrt{A_t}[0.6 + 1.3(1 + \log_{10} E')^2] & (0.1 < E' < 5\,\text{GeV}) \\ 0.032\sqrt{A_t} & (E' \geq 5\,\text{GeV}) \end{array} \right\} \tag{3.5.21}$$

with the corresponding spectral parameters

$$\alpha_{2p} = \left\{ \begin{array}{ll} (0.11 + 0.01E')(1 - 0.001A_t) & (E' < 5\,\text{GeV}) \\ 0.16(1 - 0.001A_t) & (E' \geq 5\,\text{GeV}) \end{array} \right\} \tag{3.5.22a}$$

$$\alpha_{2n} = \left\{ \begin{array}{ll} (0.1 + 0.01E')(1 - 0.001A_t) & (E' < 5\,\text{GeV}) \\ 0.15(1 - 0.001A_t) & (E' \geq 5\,\text{GeV}) \end{array} \right\} \tag{3.5.22b}$$

The third term in the summation is the balance of cascade particles after the inclusion of the quasi-elastic contribution.

The quasi-elastic contribution is estimated by including the nuclear attenuation following the quasi-elastic event. The proton quasi-elastic cross section is

$$\left. \begin{array}{l} \sigma_{Q,pp} = Z_t\sigma_{pp} + (A_t - Z_t)\sigma_{np} \\ \sigma_{Q,pn} = (A_t - Z_t)\sigma_{np} \end{array} \right\} \tag{3.5.23}$$

13

and similarly for neutrons,

$$\left.\begin{array}{l} \sigma_{Q,nn} = (A_t - Z_t)\sigma_{nn} + Z_t\sigma_{np} \\[2mm] \sigma_{Q,np} = Z_t\sigma_{np} \end{array}\right\} \qquad (3.5.24)$$

The corresponding multiplicities are taken as

$$N_{Q,jk} = e^{-0.05\sqrt{A_t}}\sigma_{Q,jk}\Big/ \sum_\ell \sigma_{Q,j\ell} \qquad (3.5.25)$$

where the exponential factor accounts for the attenuation of the quasi-elastic particles before they escape the nucleus. The balance of the cascade particles is contained in N_3 as

$$N_3 = N_c - N_2 - N_Q \qquad (3.5.26)$$

with an assumed spectral coefficient given by

$$\alpha_3 = \alpha_2/0.7 \qquad (3.5.27)$$

Results of the present formalism are shown in figures 38 to 51 in comparison with the calculations of Bertini et al. (ref. 46). Some further improvements in this parameterization need to be made.

3.5.4. Light-fragment spectrum.

The light-fragment yields per event are given in table 3.5.3 as obtained from Bertini's MECC-7 calculations (ref. 47). These results are extrapolated and interpolated in energy and mass number. The corresponding mean energies are given in table 3.5.4. The mean energies are used in Ranft's formula for nucleons and are similarly used for the light ions.

3.5.5. Heavy-fragment spectrum.

Following the direct ejection of nucleons in nuclear collision, the nucleus is left in a highly excited state that decays through particle emission. From a sudden approximation point of view, as proposed by Serber (ref. 41), the momentum distribution of the decay particles is governed by the fermi distribution prior to collision. The collective momentum of decay products and nuclear fragments is thus derived on the basis of combinatorial rules on the random ways in which a given fragment mass can be formed from the nucleon distributions prior to collision (refs. 55 and 56). The formulation of Goldhaber (ref. 56) is physically meaningful and simplistic. The momentum distribution is Gaussian in momentum space with a momentum width parameter given by

$$\sigma_p = \sigma_0 \left[A_f(A_t - A_f)/(A_t - 1) \right]^{1/2} \qquad (3.5.28)$$

where σ_0 is the usual mean fermi momentum of the struck nucleus. However, the σ_0 of nuclear fragmentation is found to be about 25 percent smaller than that observed in electron scattering experiments (ref. 39). The mean fermi momentum is a slowly varying function of nuclear mass.

A slight modification of Goldhaber's result is found to adequately represent the experimental results of Greiner et al. (ref. 39) given by

$$\sigma_p = 0.8b \left[4\delta_A/20(A_t - 1) \right]^{1/2} \qquad (3.5.29)$$

where the parameters b and δ_A are given, respectively, by

$$b = \min\left(112A_t^{1/2}, 260\right) \qquad (3.5.30)$$

14

and

$$\delta_A = \left\{ \begin{array}{ll} 0.45 & (A_t = A_f) \\ A_t - A_f & (\text{Otherwise}) \end{array} \right\} \tag{3.5.31}$$

A comparison of formulas (3.5.29) to (3.5.31) with experiments and the parameterization of Greiner et al. (ref. 39) is given in table 3.5.5. Clearly, the present formulas are quite accurate.

The spectral distributions of the nuclear fragments in the rest frame of the struck nucleus prior to collision are given by

$$\frac{d\sigma_f}{dE} = \frac{\sigma_f}{(2\pi E_0^3)^{1/2}} E^{1/2} \exp(-E/2E_0) \tag{3.5.32}$$

where σ_f is the fragmentation cross section and the energy parameter is

$$E_0 = 3\,\sigma_p^2/2A_f \tag{3.5.33}$$

The average energies $\overline{E}$ of various fragments obtained by equations (3.5.29) to (3.5.33) are compared with results of the Bertini model in table 3.5.6. Generally, the average energies predicted by the Bertini model are reasonably accurate, although some specific isotopes differ by a factor of 2 or more.

3.5.6. Energy-transfer cross section. The energy-loss spectrum $\psi_j(\mathbf{x}, \mathbf{\Omega}, E)$ of an ion fragment j (ref. 57) may be written as

$$\psi_j(\mathbf{x}, \mathbf{\Omega}, E) \approx A_j\, \zeta_j(\mathbf{x}) \int_E^{E_\gamma} \left(\frac{m}{2\pi\sigma_p^2} \right)^{3/2} \sqrt{2E'} E^{-mE'/\sigma_p^2} dE' \tag{3.5.34}$$

where A_j is the fragment mass number, $\zeta_j(\mathbf{x})$ is the fragment source, and E_γ is related to the distance to the boundary along the direction $\mathbf{\Omega}$ as given elsewhere (ref. 57). For distances far from the boundary, one may take $E_\gamma = \infty$. The cumulative energy-loss spectrum far from the boundary ($E_\gamma = \infty$) is

$$D_j(\mathbf{x}, E) = 4\pi \int_E^\infty \psi_j(\mathbf{x}, \mathbf{\Omega}, E')\, dE' \tag{3.5.35}$$

from which the distribution in linear energy transfer (LET) of energy deposit can be found. The total energy absorbed is given by

$$D(\mathbf{x}) = \sum_j D_j(\mathbf{x}, 0)$$

$$\approx \sum_j E_j \sigma_j \rho \phi \tag{3.5.36}$$

where E_j is the average energy of the fragment j, σ_j is the fragmentation cross section, ρ is the target density, and ϕ is the effective nucleon flux initiating the fragmentation events. The energy-transfer cross section of the various fragment components is $E_j\sigma_j$ and is shown in table 3.5.7 for the Rudstam parameterization (present results), Bertini data (ref. 46), and experiments of the Heckman group (refs. 39 and 40) for comparison. Equations (3.5.34) to (3.5.36) also provide a basis for resolving the energy-transfer cross section into its various LET components. The LET components of equation (3.5.35) are shown in figure 52 for $\rho = \phi = 1$ for all contributions with a fragment charge greater than 1. The two curves shown in the figure are for the Bertini data and the experiments of the Heckman group. Results obtained using our modified Rudstam formalism and the parameterized momentum distributions are virtually indistinguishable from the curve based on the LBL experiments. It is clear from the results

shown in figure 52 that estimates of exposure from heavy ion recoil nuclei in tissue based on Bertini cross sections are generally low.

4. Methods of Solution

In an earlier paper (ref. 3), we proposed the use of a perturbation theory to develop a numerical method for solving the one-dimensional charged-particle transport problem. Although the resulting algorithm was greatly simplified compared with Monte Carlo algorithms, it still suffered from the need to manipulate large amounts of numerical data. In the present section, we show how the integral operators of that earlier work (ref. 3) may be numerically evaluated to eliminate the need to store and manipulate large amounts of numerical data, and at the same time we develop an algorithm that maintains a close relation to the physical field quantities. The resultant numerical solutions are compared with results obtained by analytical solutions for realistic interactions.

4.1. Energy-Independent Proton Model

The Boltzmann equation for proton transport in the straight ahead approximation is given as

$$\left[\frac{\partial}{\partial x} - \frac{\partial}{\partial E} S(E) + \sigma \right] \phi(x, E) = \int_E^\infty f(E, E') \phi(x, E') \, dE' \tag{4.1.1}$$

where $S(E)$ is the proton stopping power, σ is the macroscopic interaction cross section which we presently take as energy independent, and $f(E, E')$ is the production secondary-particle spectrum. Using the definitions

$$r = \int_0^E dE' / S(E') \tag{4.1.2}$$

$$\psi(x, r) = S(E) \phi(x, E) \tag{4.1.3}$$

and

$$\bar{f}(r, r') = S(E) f(E, E') \tag{4.1.4}$$

allows equation (4.1.1) to be rewritten as

$$\psi(x, r) = e^{-\sigma x} \psi(0, r + x) + \int_0^x dz \, e^{-\sigma z} \int_{r+z}^\infty dr' \, \bar{f}(r + z, r') \, \psi(x - z, r') \tag{4.1.5}$$

where the boundary condition is

$$\psi(0, r) = S(E) \phi(0, E) \tag{4.1.6}$$

A numerical algorithm for equation (4.1.5) is found by noting that

$$\psi(x + h, r) = e^{-\sigma h} \psi(x, r + h) + \int_0^h dz \, e^{-\sigma z} \int_r^\infty dr' \, \bar{f}(r + z, r'z) \, \psi(x + h - z, r' + z) \tag{4.1.7}$$

which can be simplified by using

$$\psi(x + h - z, r) \approx e^{-\sigma(h - z)} \psi(x, r + h - z) + 0(h) \tag{4.1.8}$$

which yields

$$\psi(x + h, r) \approx e^{-\sigma h} \psi(x, r + h) + e^{-\sigma h} \int_0^h dz \int_r^\infty dr' \, \bar{f}(r + z, r' + z) \, \psi(x, r' + h) \tag{4.1.9}$$

16

with the order of h^2 where h is the step size. Equation (4.1.9) is accurate for distances such that $\sigma h << 1$ and may be used to relate the spectrum at some point x to the spectrum at $x + h$. Therefore, one may begin at the boundary ($x = 0$) and propagate the solution to any arbitrary interior point using equation (4.1.9).

In the event that the boundary has a discrete spectrum such as

$$\phi(0, E) = \delta(E - E_0) \tag{4.1.10}$$

then

$$\psi(0, r) = \delta(r - r_0) \tag{4.1.11}$$

When discrete spectra are present at the boundary, the solution contains both singular and continuous components which we label ψ_s and ψ_c, respectively. The corresponding singular term in the solution is then

$$\psi_s(x, r) = e^{-\sigma x} \, \delta(r + x - r_0) \tag{4.1.12}$$

whereas the continuous term satisfies

$$\psi_c(x + h, r) = e^{-\sigma h} \, \psi_c(x, r + h)$$
$$+ \int_0^h dz \, e^{-\sigma z} \int_r^\infty dr' \, \bar{f}(r + z, r' + z) \left[\psi_s(x + h - z, r' + z) \right.$$
$$\left. + \psi_c(x + h - z, r' + z) \right] \tag{4.1.13}$$

The first term under the integral may be evaluated using equation (4.1.12) to obtain

$$\psi_c(x + h, r) = e^{-\sigma h} \, \psi_c(x, r + h) + e^{-\sigma(x+h)} \int_0^h dz \, \bar{f}(r + z, r_0 - x - h + z)$$
$$+ \int_0^h dz \, e^{-\sigma z} \int_r^\infty dr' \, \bar{f}(r + z, r' + z) \, \psi_c(x + h - z, r' + z) \tag{4.1.14}$$

The solution over small values of $(h - z)$ may be approximated as

$$\psi_c(x + h - z, r) \approx e^{-\sigma(h-z)} \, \psi_c(x, r + h - z) + 0(h - z) \tag{4.1.15}$$

for which (see the appendix)

$$\psi_c(x + h, r) \approx e^{-\sigma h} \left[\psi_c(x, r + h) + e^{-\sigma x} \overline{F}\left(r, h, r_0 - x - \frac{h}{2}\right) \right]$$
$$+ e^{-\sigma h} \int_r^\infty dr' \overline{F}(r, h, r') \, \psi_c(x, r' + h) \tag{4.1.16}$$

where

$$\overline{F}(r, h, r') = \int_0^h dz \, \bar{f}(r + z, r')$$
$$= F_c[\epsilon(r + h), E'] - F_c(E, E') \tag{4.1.17}$$

where $\epsilon(r)$ is the energy for range r and

$$F_c(E, E') = \int_0^E f(E, E') \, dE \tag{4.1.18}$$

17

which is the cumulative secondary-particle spectrum. Note that equation (4.1.16) requires only one numerical integration per step in x.

4.1.1. Discrete spectrum.

Nucleon-nucleon scattering can be well-approximated (see section 3.5) by

$$f(E, E') = ce^{-\alpha(E'-E)} \tag{4.1.19}$$

where $c/\alpha = \sigma$. This spectrum is related to the quasi-elastic spectrum of nucleon-nucleus reactions. Similar to this spectrum is

$$f(r, r') = ce^{-\alpha(r'-r)} \tag{4.1.20}$$

As a model problem, the spectrum of equation (4.1.20) is realistic and can be solved using perturbation theory. The first term is the uncollided beam term

$$\psi_0(x, r) = e^{-\sigma x}\delta(r_0 - r - x) \tag{4.1.21}$$

The first-generation term is

$$\psi_1(x, r) = xe^{-\sigma x}ce^{-\alpha(r_0 - r - x)} \tag{4.1.22}$$

and the higher-order terms are

$$\psi_n(x, r) = \frac{1}{n!}x^n e^{-\sigma x}\frac{c^n}{(n-1)!}(r_0 - r - x)^{n-1}e^{-\alpha(r_0 - r - x)} \tag{4.1.23}$$

This problem is solved numerically using equation (4.1.16) and is compared with the analytic solution in table 4.1.1. The incident beam is for 500 MeV protons on a water shield with $\sigma = 0.01$ cm^2/g and $\alpha \approx 0.0123$ cm^2/g.

As seen from the table, solutions with discrete spectra are limited in accuracy to 5 percent, independent of the depth of penetration. This error arises from the energy interpolation formula as the spectrum is highly discontinuous. Special interpolation methods could be developed to reduce this error greatly.

4.1.2. Continuous spectrum.

For this test, a spectrum similar to a solar proton event is taken as

$$\psi(0, r) = e^{-\beta r} \tag{4.1.24}$$

The leading term in the perturbation theory is

$$\psi_0(x, r) = e^{-\sigma x}e^{-\beta(r+x)} \tag{4.1.25}$$

with successive collision terms given by

$$\psi_n(x, r) = \frac{1}{n} \times \frac{c}{(\alpha + \beta)}\psi_{n-1}(x, r) \tag{4.1.26}$$

This problem is solved numerically and compared with the analytic result in table 4.1.2. It is seen from the table that the agreement for the two solutions in this case is generally within ± 1 percent. Clearly, high-quality numerical solutions are available for continuous spectra at the boundary.

The algorithm developed herein provides adequate solutions to proton beam problems with discrete spectral components and highly accurate solutions for typical space applications involving continuous spectra. The computation times for each of these test problems were less

than several minutes on a CYBER mainframe, thus offering a very favorable comparison with Monte Carlo or previous methods based on the perturbation theory (ref. 3).

4.2. Coupled Baryon Transport Methods

The coupled baryon transport equations are of the form

$$\left[\frac{\partial}{\partial x} - \nu_j \frac{\partial}{\partial E} S(E) + \sigma_j(E) \right] \phi_j(x, E) = \sum_k \int_0^\infty f_{jk}(E, E') \phi_k(x, E') \, dE' \qquad (4.2.1)$$

where ν_j is the range scaling parameter, $S(E)$ is the proton stopping power, $\sigma(E)$ is the total cross section, $\phi_j(x, E)$ is the differential flux spectrum of type j baryons, and $f_{jk}(E, E')$ is a differential energy cross section for redistribution of particle type and energy. Utilizing the definitions

$$r = \int_0^E dE'/S(E') \qquad (4.2.2)$$

$$\psi_j(x, r) = S(E) \, \phi_j(x, E) \qquad (4.2.3)$$

and

$$\bar{f}_{jk}(r, r') = S(E) \, f_{jk}(E, E') \qquad (4.2.4)$$

allows equation (4.2.1) to be rewritten as

$$\left[\frac{\partial}{\partial x} - \nu_j \frac{\partial}{\partial r} + \sigma_j(r) \right] \psi_j(x, r) = \sum_k \int_0^\infty \bar{f}_{jk}(r, r') \, \psi_k(x, r') \, dr' \qquad (4.2.5)$$

which may be rewritten (refs. 3 and 4) as

$$\psi_j(x, r) = e^{-\zeta_j(r, x)} \psi_j(0, r + \nu_j x)$$

$$+ \sum_k \int_0^x \int_0^\infty e^{-\zeta_j(r, z)} \bar{f}_{jk}(r + \nu_j z, r') \, \psi_k(x - t, r') \, dr' dz \qquad (4.2.6)$$

where the exponential is the integrating factor

$$\zeta_j(r, t) = \int_0^t \sigma_j(r + \nu_j t') \, dt'$$

If the interactions are such that

$$\bar{f}_{jk}(r, r') = \delta_{jk} \, g(r - r') \qquad (4.2.7)$$

where g denotes the appropriate spectral function, then the solutions to equation (4.2.5) are of the form

$$\psi_j(x, r) = \chi(x, r + \nu_j x) \qquad (4.2.8)$$

To demonstrate how remarkable equation (4.2.8) is, we note that if $\chi(x, r)$ is the solution to the neutron transport equation ($\nu_n = 0$), then $\chi(x, r + \nu_p x)$ is the solution to the proton transport problem independent of the functional form chosen for the stopping power.

Rather simple numerical procedures follow from equation (4.2.6). Noting that the first-order nature of equation (4.2.1) allows $\psi_j(x, r)$ to be taken as a boundary condition for propagation

to larger x, one may approximate equation (4.2.6) as

$$\psi_j(x+h,r) = e^{-\zeta_j(r,h)}\psi_j(x, r + \nu_j h)$$

$$+ \sum_k \int_0^h \int_0^\infty e^{-\zeta_j(r,z)} \bar{f}_{jk}(r + \nu_j z, r')\, \psi(x + h - z, r')\, dz\, dr' \qquad (4.2.9)$$

which may be used to develop a numerical stepping procedure. Equation (4.2.9) has provided the basis for a number of new transport codes for baryons of mass number greater than or equal to 1 (refs. 2, 4, and 5). These codes are now being extended to couple with the meson fields and to the negative baryon number fields.

If h is sufficiently small such that

$$\sigma_j(r')\, h << 1 \qquad (4.2.10)$$

then, according to perturbation theory (ref. 3),

$$\psi_k(x + h - z, r') \approx e^{-\zeta_k(r, h - z)}\psi_k[x, r' + \nu_k(h - z)] \qquad (4.2.11)$$

which may be used to approximate the above integral of equation (4.2.9).

For many cases of practical interest (e.g., accelerator studies), monoenergetic particle beams are used, and separation of the singular terms from the solution becomes convenient. The initial beam of type J particles of energy E_0 (where $r_0 = R(E_0)$) is taken as

$$\psi_j(0, r) = \delta_{jJ}\delta(r_0 - r) \qquad (4.2.12)$$

and the solution is written as

$$\psi_j(x, r) = \psi_{j0}(x, r) + \psi_j(x, r) \qquad (4.2.13)$$

The corresponding singular terms are

$$\psi_{k0}(x, r) = e^{-\zeta_k(r,x)}\delta(r_0 - r - \nu_k x)\, \delta_{kj} \qquad (4.2.14)$$

The regular terms of equation (4.2.9) for $k = p$ may be written as

$$\psi_p(x+h,r) = e^{\zeta_p(r,h)}\psi_p(x, r + h)$$

$$+ \int_0^h dz\, e^{-\zeta_p(r,z)} \sum_j \int_{r+z}^\infty \bar{f}_{pj}(r + z, r')[\psi_{j0}(x + h - z, r')$$

$$+ \psi_j(x + h - z, r')]\, dr' \qquad (4.2.15)$$

and the regular terms for $k = n$ are

$$\psi_n(x+h,r) = e^{-\sigma_n(r)h}\,\psi_n(x, r)$$

$$+ \int_0^h dz\, e^{-\sigma_n(r)z} \sum_j \int_r^\infty \bar{f}_{nj}(r, r')\,[\psi_{j0}(x + h - z, r')$$

$$+ \psi_j(x + h - z, r')]\, dr' \qquad (4.2.16)$$

The singular contributions under the integrals of equations (4.2.15) and (4.2.16) can be evaluated with equation (4.2.14), and the approximations in equations (4.2.10) and (4.2.11)

can be applied to find

$$\psi_p(x+h,r) = \exp[-\sigma_p(r)h]\,\psi_p(x,r+h)$$

$$+ \exp\left\{-[\sigma_p(r) + \sigma_p(r_0')]\frac{h}{2}\right\} \overline{F}_{pp}(h,r,r_0')\,\delta_{pj}\exp[-\zeta_p(r_0',x)]$$

$$+ \exp\left\{-[\sigma_p(r) + \sigma_n(r_0)]\frac{h}{2}\right\} \overline{F}_{pn}(h,r,r_0)\,\delta_{nj}\exp[-\sigma_n(r_0)\,x]$$

$$+ \int_r^\infty \exp\left\{-\left[\sigma_p(r) + \sigma_p\left(r'+\frac{h}{2}\right)\right]\frac{h}{2}\right\} \overline{F}_{pp}\left(h,r,r'+\frac{h}{2}\right)\psi_p(x,r'+h)\,dr'$$

$$+ \int_r^\infty \exp\left\{-\left[\sigma_p(r) + \sigma_n\left(r'+\frac{h}{2}\right)\right]\frac{h}{2}\right\} \overline{F}_{pn}\left(h,r,r'+\frac{h}{2}\right)\psi_n(x,r'+h)\,dr' \tag{4.2.17}$$

and

$$\psi_n(x+h,r) = \exp[-\sigma_n(r)h]\,\psi_n(x,r)$$

$$+ h\,\bar{f}_{np}(r,r_0')\exp\left\{-[\sigma_n(r) + \sigma_p(r_0')]\frac{h}{2}\right\} \delta_{pj}\exp[\zeta_p(r_0',x)]$$

$$+ h\bar{f}_{nn}(r,r_0)\exp\left\{-[\sigma_n(r) + \sigma_n(r_0)]\frac{h}{2}\right\} \delta_{nj}\exp[-\sigma_n(r_0)x]$$

$$+ h\int_r^\infty \exp\left\{-[\sigma_n(r) + \sigma_p(r')]\frac{h}{2}\right\} \bar{f}_{np}(r,r')\,\psi_p\left(x,r'+\frac{h}{2}\right)dr'$$

$$+ h\int_r^\infty \exp\left\{-[\sigma_n(r) + \sigma_n(r')]\frac{h}{2}\right\} \bar{f}_{nn}(r,r')\,\psi_n(x,r')\,dr' \tag{4.2.18}$$

where $r_0' = r_0 - x - \frac{h}{2}$ and $\overline{F}$ is related to the cumulative spectrum F as given by

$$\overline{F}_{ij}(h,r,r') = \int_0^\infty \bar{f}_{ij}(r+z,r')\,dz$$

$$\equiv F_{ij}(r+h,r') - F_{ij}(r,r') \tag{4.2.19}$$

with

$$F_{ij}(r,r') = \int_0^{\epsilon(r)} f_{ij}(E,E')\,dE \tag{4.2.20}$$

$\epsilon(r)$ is the energy associated with residual range r, and $E' = \epsilon(r')$. Equations (4.2.17) and (4.2.18) are evaluated by establishing an x-grid at which $\psi_j(x_m,r)$ is evaluated where h is the distance between each successive evaluation. The integral over r' is accomplished by establishing an r-grid (and the corresponding E-grid) and using

$$\int_{rn}^\infty g(r_n,r')\,\psi_j(x_m,r')\,dr' \approx \sum_{\ell=n}^\infty g_n(r_n,\bar{r}_\ell)\int_{r_\ell}^{r_{\ell+1}} \psi_j(x_m,r)\,dr' \tag{4.2.21}$$

where $\bar{r}_\ell = (r_\ell + r_{\ell+1})/2$ and the series terminates at the highest ℓ-value in the r-grid. There is a spatially dependent discontinuity in the proton flux spectrum which requires right- and left-hand interpolation and integration. These discontinuities have been treated in the computational procedures.

4.3. Neutron Source

The neutron transport equation in three dimensions is

$$[\boldsymbol{\Omega} \cdot \nabla + \sigma_n(E)]\,\phi_n(\mathbf{x}, \boldsymbol{\Omega}, E) = \sum_j \int_E^\infty f_{nj}(E, E', \boldsymbol{\Omega}, \boldsymbol{\Omega}')\phi_j(\mathbf{x}, \boldsymbol{\Omega}', E')\,d\boldsymbol{\Omega}'\,dE' \qquad (4.3.1)$$

Although the straight ahead approximation is adequate for most proton calculations, the neutron fields are more strongly affected by nonforward scattering components, particularly the low-energy neutrons. The reason is that the lower-energy neutrons have a greater range than the lower-energy protons because of the electric charge difference. Thus, a first-order correction to the straight ahead approximation may be applied by substituting the proton coupling in equation (4.3.1) by the straight ahead solution for $\phi_p(\mathbf{x}, \boldsymbol{\Omega}, E)$ so that

$$\xi_n(\mathbf{x}, \boldsymbol{\Omega}, E) = \int_E^\infty f_{np}(E, E', \boldsymbol{\Omega}, \boldsymbol{\Omega}_x)\,\phi_p(\mathbf{x}, E')\,dE' \qquad (4.3.2)$$

The corresponding neutron transport equation is

$$[\boldsymbol{\Omega} \cdot \nabla + \sigma_n(E)]\,\phi_n(\mathbf{x}, \boldsymbol{\Omega}, E) = \int_E^\infty f_{nn}(E, E', \boldsymbol{\Omega}, \boldsymbol{\Omega}')\,\phi_n(\mathbf{x}, \boldsymbol{\Omega}', E')\,d\boldsymbol{\Omega}'\,dE' + \xi_n(\mathbf{x}, \boldsymbol{\Omega}, E) \quad (4.3.3)$$

The neutron source integral is treated in a fashion similar to that of equation (4.2.21).

4.4. Target-Fragment Secondary Flux

The target fragmentations produced in nuclear collision with the nucleon field must now be treated. The spectral parameters of the composite fragments are relatively independent of the projectile charge, energy, or direction. This leads to some simplifying assumptions so that

$$\phi_j^T(\mathbf{x}, \boldsymbol{\Omega}, E) = \frac{1}{S_j(E)}\xi_j(\mathbf{x})\int_E^{E\gamma} f_j(E')\,dE' \qquad (4.4.1)$$

$$E\gamma = R_j^{-1}[R_j(E) + d(\boldsymbol{\Omega})] \qquad (4.4.2)$$

where $d(\boldsymbol{\Omega})$ is the distance from the boundary (ref. 57). The source of ions of type j is evaluated as

$$\xi_j(\mathbf{x}) = \sum_i \int_0^\infty \sigma_{ji}(E')\,\phi_i(\mathbf{x}, \boldsymbol{\Omega}', E')\,d\boldsymbol{\Omega}'\,dE' \qquad (4.4.3)$$

where $\sigma_{ji}(E')$ represents the fragmentation cross sections. The $f_j(E')$ represents the spectral contributions averaged over all the target atomic constituents. In the present code, the distance to the boundary is assumed to be large. One could treat not only the boundary effects but the interface effects as well.

5. Results

As an initial validation of the present code, comparisons are made both with prior calculations using Monte Carlo methods and with experimental data. Fully three-dimensional Monte Carlo calculations have been made with the Bertini code as the nuclear cross section set augmented with low-energy neutron data. (See refs. 58 and 59 for a detailed discussion.) Energy absorption in a tissue slab for normally incident neutrons of energies 0.5, 2, and 10 MeV is shown in table 5.1. Also shown are the results of the present code. The results appear remarkably good when considering the crudeness of the straight ahead approximation for low-energy neutrons and the limitations on the present data base. Results for higher-energy neutrons are shown in figures 53 to 57. In each case, reasonable agreement with the results of Zerby and Kinney

(ref. 59) are obtained. Similar results are found for energetic protons as shown in figures 58 to 61. The present data base changes the results in figures 53 to 61 by only a few percent when compared with the results in reference 2. In the present calculation, the first-generation proton spectrum is discontinuous for monoenergetic beams and is best handled by taking many energy points in the spectrum. However, the calculation time then becomes excessive. The present results were calculated using only 30 energy points. This process is adequate for space radiation, as shown in reference 60, but it is marginal for the present monoenergetic results. The use of numerical benchmark problems will allow us to understand the numerical procedures better. Such a benchmark has already provided some insight (refs. 60 to 62).

The code has been used to calculate the dose behind various shields for typical space radiation. Three major solar-particle events of solar cycles 19 and 20 are represented in figure 62. The spectra as given in reference 63 have been used. The modification of the solar-event spectra at various depths in a lunar soil model is shown in figures 63 to 65. The importance of the buildup of secondary neutrons is clearly apparent in the February 1956 and November 1960 events and does not appear at all in the August 1972 event. The neutrons of the February 1956 event reach a stationary value between 25 and 100 g/cm^2, as has been observed in our earlier calculations (ref. 37). The resulting dose within a 5-cm sphere of tissue-equivalent material is shown as a function of soil thickness in figure 66. The dose reduces only slowly for increasing the thickness beyond 20 cm.

Galactic protons and their secondary neutron spectra behind varying thicknesses of aluminum are shown in figures 67 and 68. The incident proton spectrum is that for a solar maximum according to the model of Adams et al. (ref. 64). It is clear that the neutron flux approaches a maximum near 50 g/cm^2 which is similar to the lunar soil results. Results for penetration of the martian atmosphere are indicated in figure 69. The potential use of polyethylene for controlling the neutron flux levels is indicated in figure 70. There are important geometric factors to be applied to all these results for which some detail is given elsewhere (ref. 65).

6. Concluding Remarks

The emphasis of the present code is on high-energy baryon transport, but such a code must adequately represent the low-energy neutrons in a reasonable way. It is seen from the present results that this representation has been accomplished in the present code. The calculation of 100 to 400 MeV neutrons and protons on tissue is in reasonable agreement with a more complete Monte Carlo code. The primary advantage of the present code is computer efficiency while maintaining adequate accuracy. Future work will concentrate on improving the representation of the quasi-elastic peak, the low-energy neutron transport algorithm, and adding the effects of meson production to improve the comparisons further.

NASA Langley Research Center
Hampton, VA 23665-5225
December 21, 1988

7. Appendix

Numerical Procedures

In this appendix we consider the question of the appropriate numerical procedure for evaluating equation (4.1.5). The equation being solved is

$$\psi(x,r) = e^{-\sigma x}\,\psi(0, r+x) + \int_0^x dz\, e^{-\sigma z} \int_{r+z}^\infty dr'\, \bar{f}(r+z, r')\,\psi(x-z, r') \tag{A1}$$

which may be solved using perturbation theory for a monoenergetic beam as

$$\psi_0(x,r) = e^{-\sigma x}\,\delta(r+x-r_0) \tag{A2}$$

$$\psi_1(x,r) = e^{-\sigma x} \int_0^x dz\, \bar{f}(r+z, r_0 - x + z) \tag{A3}$$

with higher-order terms being obtained by repeated substitution into equation (A1). Note that if $\bar{f}(r, r')$ is a function only of $(r - r')$, then

$$\psi_1(x,r) = x e^{-\sigma x}\, \bar{f}(r, r_0 - x) \tag{A4}$$

Equation (A4) would hold for the quasi-elastic peak distribution for which

$$\bar{f}(r, r') \approx c e^{-\alpha(r' - r)} \tag{A5}$$

where α and c are constants. Equation (A4) does not follow for the quasi-elastic recoil particles for which

$$\bar{f}(r, r') \approx c' e^{-\alpha r} \tag{A6}$$

It follows that equation (A3) can be written as

$$\psi_1(x,r) \approx e^{-\sigma x}[\overline{F}(r+x, r_0 - x - Q) - \overline{F}(r, r_0 - x - Q)] \tag{A7}$$

where the choice for Q is not entirely clear but in some way represents the average z dependence of equation (A3) on the interval 0 to x. If c' and α are strictly constants, then equation (A7) is independent of the choice of Q. In general, the spectral function $\bar{f}(r, r')$ contains terms like those in equations (A5) and (A6) simultaneously so that whatever numerical solution is implemented, the character of both solutions (A4) and (A7) must be retained.

The numerical solution to equation (A1) is rendered as

$$\psi_s(x+h, r) = e^{-\sigma h}\,\psi_s(x, r+h) \tag{A8}$$

for the singular part and as

$$\psi_c(x+h, r) = e^{-\sigma h}\bigg[\psi_c(x, r+h) + \int_0^h dz\, \overline{F}(r+z, r_0 - x - Q)\, e^{-\sigma x}$$

$$+ \int_0^h dz \int_r^\infty \overline{F}(r+z, r'+z)\,\psi_s(x, r'+h)\, dr'\bigg] \tag{A9}$$

for the continuous spectral components. The first two terms of equation (A9) correspond to $\psi(x,r)$ of the perturbation theory, and the requirement

$$\psi_1(x+h, r) = e^{-\sigma h}\bigg[\psi_s(x, r+h) + \int_0^h dz\, \overline{F}(r-z, r_0 - x - Q)\, e^{-\sigma x}\bigg] \tag{A10}$$

24

must be met by any numerical procedure. One may show equation (A10) to be an identity for $Q = h - z$. We now inquire as to a suitable choice for Q. Clearly, computational accuracy of equation (A10) depends entirely on exactness to which the integral in (A10) is evaluated.

We first note that the integral in equation (A10) for the quasi-elastic peak has the value

$$\int_0^h \overline{F}(r + z, r_0 - x - h - z)\, dz = hc \exp[-\alpha(r_0 - x - h - r)] \tag{A11}$$

for the exact value of Q. Assuming Q to be some fixed value results in

$$\int_0^h \overline{F}(r + z, r_0 - x - Q)\, dz = \frac{c}{\alpha} \exp[-\alpha(r_0 - x - h - r)][e^{\alpha Q} - e^{\alpha(Q-h)}]$$

$$= hc \exp[-\alpha(r_0 - x - h - r)]\left[1 + \alpha Q - \frac{1}{2}\alpha h + 0(h^2)\right] \tag{A12}$$

Clearly, the error of equation (A12) is minimized by taking $Q = h/2$. Note that this value of Q would also be chosen on intuition, since it represents the values at the midpoint of the interval.

The above question was investigated using the numerical calculations and an analytic solution for the quasi-elastic peak form of the secondary spectrum. The analytic solution is graphically presented in figure A1. The numerical solutions for $Q = 0$ and $Q = h$ are shown, respectively, in figures A2 and A3. The corresponding errors are shown in figures A4 and A5. In each case, the errors mainly occur near the upper energy limit of the spectrum at each depth x. The $Q = 0$ solution is a slight overestimate of the flux at the highest energies and $Q = h$ is a slight underestimate. In accordance with the result of equation (A12), we expect the errors of figures A4 and A5 to nearly cancel if the value $Q = h/2$ is used. The solution for $Q = h/2$ is shown in figure A6 with the corresponding errors in figures A7 and A8. Clearly, an adequate approximation is obtained using $Q = h/2$, although it is clear from the present analysis that even greater improvements can be made.
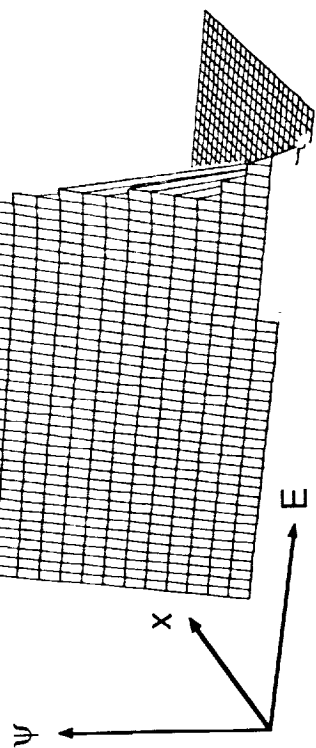
Figure A1. Analytic solution of proton-scaled flux for monoenergetic beam of incident protons of 100 MeV.
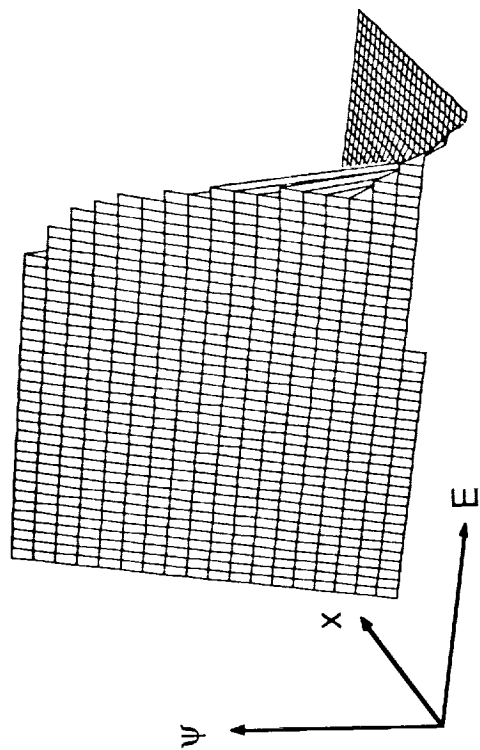
Figure A2. Numerical solution with $Q = 0$ of proton-scaled flux for monoenergetic beam of incident protons of 100 MeV.
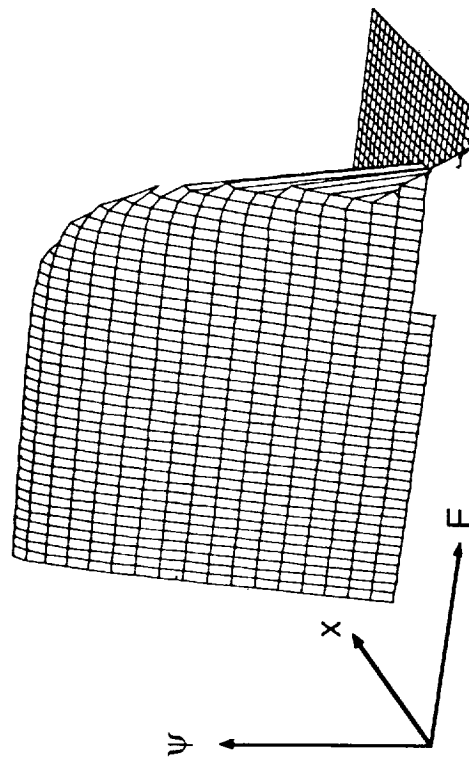
Figure A3. Numerical solution with $Q = h$ of proton-scaled flux for monoenergetic beam of incident protons of 100 MeV.
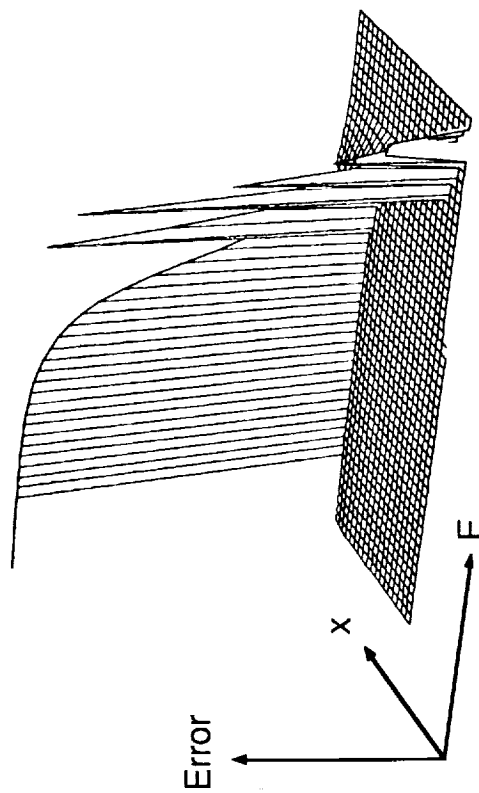
Figure A4. Numerical solution with $Q = 0$ of error in proton-scaled flux.
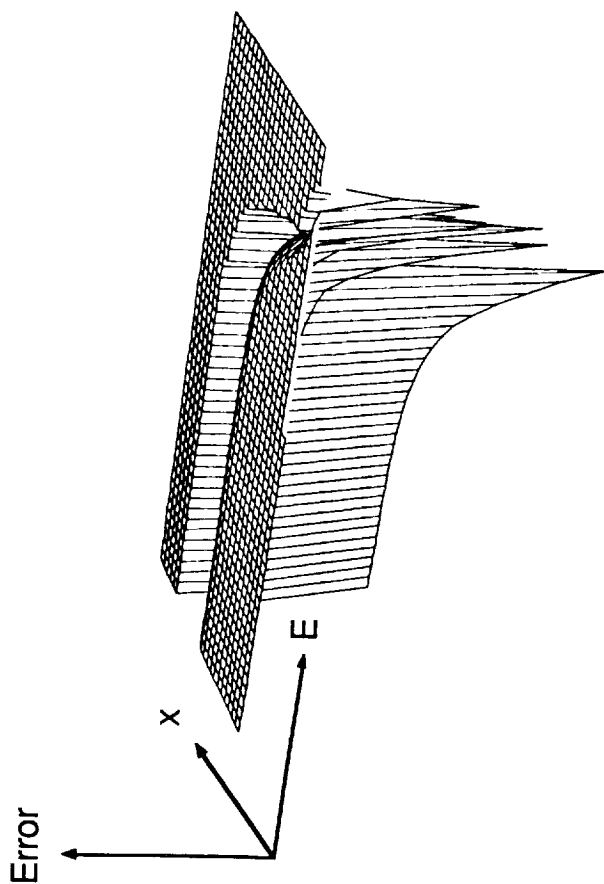
Figure A5. Error in proton-scaled flux solution with $Q = h$.
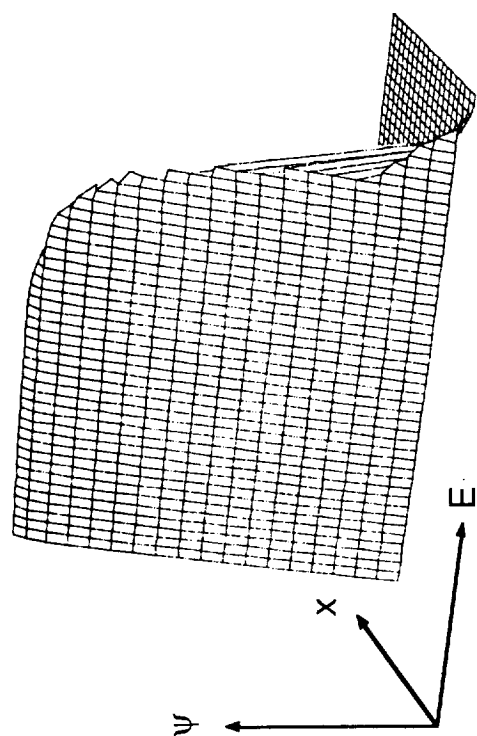
Figure A6. Numerical solution with $Q = h/2$ of proton-scaled flux for monoenergetic beam of incident protons of 100 MeV.
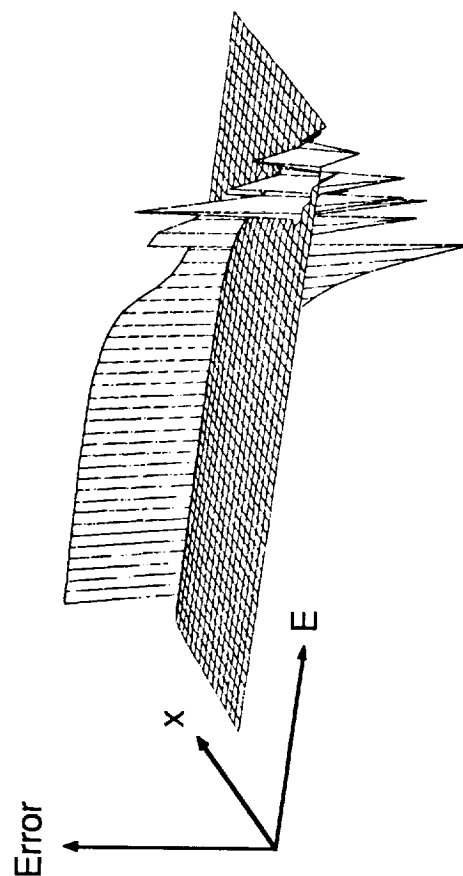
Figure A7. Front view of error in proton-scaled flux solution with $Q = h/2$.
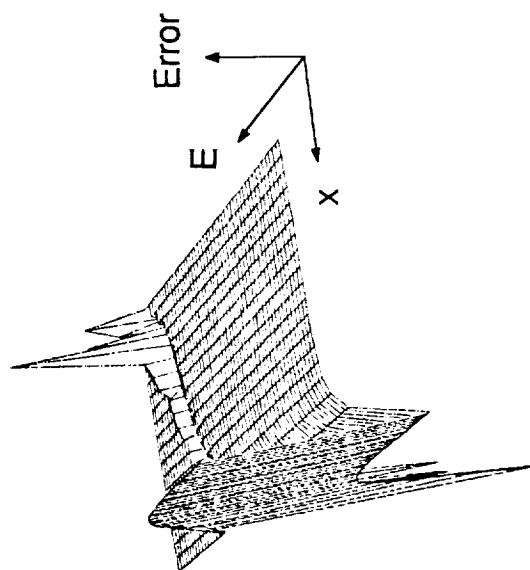
Figure A8. Back view of error in proton-scaled flux solution with $Q = h/2$.

8. References

1. Alsmiller, R. G., Jr.: High-Energy Nucleon Transport and Space Vehicle Shielding. *Nucl. Sci. & Eng.*, vol. 27, no. 2, Feb. 1967, pp. 158–189.

2. Wilson, John W.; Townsend, Lawrence W.; Chun, Sang Y.; Buck, Warren W.; Khan, Ferdous; and Cucinotta, Frank: *BRYNTRN: A Baryon Transport Computer Code—Computation Procedures and Data Base.* NASA TM-4037, 1988.

3. Wilson, John W.; and Lamkin, Stanley L.: Perturbation Theory for Charged-Particle Transport in One Dimension. *Nucl. Sci. & Eng.*, vol. 57, no. 4, Aug. 1975, pp. 292–299.

4. Wilson, John W.; and Badavi, F. F.: Methods of Galactic Heavy Ion Transport. *Radiat. Res.*, vol. 108, 1986, pp. 231–237.

5. Wilson, J. W.; Townsend, L. W.; and Badavi, F. F.: Galactic HZE Propagation Through the Earth's Atmosphere. *Radiat. Res.*, vol. 109, no. 2, Feb. 1987, pp. 173–183.

6. Walske, M. C.; and Bethe, H. A.: Asymptotic Formula for Stopping Power of K-Electrons. *Phys. Review*, vol. 83, 1951, pp. 457–458.

7. Bragg, W. H.; and Kleeman, R.: On the α Particles of Radium, and Their Loss of Range in Passing Through Various Atoms and Molecules. *Philos. Mag. & J. Sci.*, ser. 6, vol. 10, no. 57, Sept. 1905, pp. 318–340.

8. Platzman, Robert L.: On the Primary Processes in Radiation Chemistry and Biology. *Symposium on Radiobiology—The Basic Aspects of Radiation Effects on Living Systems*, James J. Nickson, ed., John Wiley & Sons, Inc., c.1952, pp. 97–116.

9. Wilson, J. W.; and Kamaratos, E.: Mean Excitation Energy for Molecules of Hydrogen and Carbon. *Phys. Lett.*, vol. 85A, no. 1, Sept. 7, 1981, pp. 27–29.

10. Wilson, J. W.; Chang, C. K.; Xu, Y. J.; and Kamaratos, E.: Ionic Bond Effects on the Mean Excitation Energy for Stopping Power. *J. Appl. Phys.*, vol. 53, no. 2, Feb. 1982, pp. 828–830.

11. Wilson, J. W.; and Xu, Y. J.: Metallic Bond Effects on Mean Excitation Energies for Stopping Power. *Phys. Lett.*, vol. 90A, no. 5, July 12, 1982, pp. 253–255.

12. Chu, W. K.; Moruzzi, V. L.; and Ziegler, J. F.: Calculations of the Energy Loss of ^{4}He Ions in Solid Elements. *J. Appl. Phys.*, vol. 46, no. 7, July 1975, pp. 2817–2820.

13. Andersen, H. H.; and Ziegler, J. F.: *Hydrogen Stopping Powers and Ranges in All Elements.* Pergamon Press, Inc., c.1977.

14. Janni, Joseph F.: *Calculations of Energy Loss, Range, Pathlength, Straggling, Multiple Scattering, and the Probability of Inelastic Nuclear Collisions for 0.1- to 1000-Mev Protons.* AFWL-TR-65-150, U.S. Air Force, Sept. 1966. (Available from DTIC as AD 643 837.)

15. Bichsel, Hans: Passage of Charged Particles Through Matter. *American Institute of Physics Handbook*, Second ed., Dwight E. Gray, ed., McGraw-Hill Book Co., Inc., 1963, pp. 8-20–8-47.

16. Ziegler, J. F.: *Helium Stopping Powers and Ranges in All Elemental Matter.* Pergamon Press, c.1977.

17. Barkas, Walter H.: *Nuclear Research Emulsions—I. Techniques and Theory.* Academic Press, Inc., 1963.

18. Lindhard, J.; Scharff, M.; and Schiott, H. E.: Range Concepts and Heavy Ion Ranges (Notes on Atomic Collisions, II). *Mat.-Fys. Medd.—K. Dan. Vid. Selske*, vol. 33, no. 14, 1963, pp. 1–42.

19. Matteson, S.; Powers, D.; and Chau, E. K. L.: Physical-State Effect in the Stopping Cross Section of H_2O Ice and Vapor for 0.3 to 2.0 MeV α Particles. *Phys. Review*, ser. A, vol. 15, no. 3, Mar. 1977, pp. 856–864.

20. Palmer, Rita B. J.; and Akhavan-Rezayat, Ahmad: Range-Energy Relations and Stopping Power of Water, Water Vapour and Tissue Equivalent Liquid for α Particles Over the Energy Range 0.5 to 8 MeV. *Sixth Symposium on Microdosimetry—Volume II*, J. Booz and H. G. Ebert, eds., Harwood Academic Publ., Ltd. (London), c.1978, pp. 739–748.

21. Northcliffe, L. C.; and Schilling, R. F.: Range and Stopping-Power Tables for Heavy Ions. *Nucl. Data, Sect. A*, vol. 7, no. 3–4, Jan. 1970, pp. 233–463.

22. Fleischer, Robert L.; Price, P. Buford; and Walker, Robert M.: *Nuclear Tracks in Solids—Principles and Applications.* Univ. of California Press, c.1975.

23. Gross, Franz: New Theory of Nuclear Forces—Relativistic Origin of the Repulsive Core. *Phys. Review D*, vol. 10, no. 1, July 1, 1974, pp. 223–242.

24. Lock, W. O.; and Measday, D. F.: *Intermediate Energy Nuclear Physics.* Methuen & Co. Ltd. (London), 1970.

25. Angeli, I.; and Csikai, J.: Total Neutron Cross Sections and the Nuclear Ramsauer Effect. *Nucl. Phys.*, vol. A158, no. 2, Dec. 14, 1970, pp. 389–392.

26. Angeli, I.; and Csikai, J.: Total Neutron Cross Sections and the Nuclear Ramsauer Effect. (II). $E_n = 0.5–42$ MeV. *Nucl. Phys.*, vol. A170, no. 3, Aug. 2, 1971, pp. 577–583.

27. Hughes, Donald J.; and Schwartz, Robert B.: Neutron Cross Sections. *BNL 325, Second ed.*, Brookhaven National Lab., July 1, 1958.

28. Townsend, Lawrence W.; Wilson, John W.; and Bidasaria, Hari B.: *Nucleon and Deuteron Scattering Cross Sections From 25 MeV/Nucleon to 22.5 GeV/Nucleon.* NASA TM-84636, 1983.

29. Letaw, John R.; Silberberg, R.; and Tsao, C. H.: Proton-Nucleus Total Inelastic Cross Sections: An Empirical Formula for $E > 10$ MeV. *Astrophys. J.*, Suppl. ser., vol. 51, no. 3, Mar. 1983, pp. 271-276.

30. Bobchenko, B. M.; Buklei, A. E.; Viasov, A. V.; Vorob'ev, I. I.; Vorob'ev, L. S.; Goryainov, N. A.; Grishuk, Yu. G.; Gushchin, O. B.; Druzhinin, B. L.; Zhurkin, V. V.; Zavrazhnov, G. N.; Kosov, M. V.; Leksin, G. A.; Stolin, V. L.; Surin, V. P.; Fedorov, V. B.; Fominykh, B. A.; Shvartsman, B. B.; Shevchenko, S. V.; and Shuvalov, S. M.: Measurement of Total Inelastic Cross Sections for Interaction of Protons With Nuclei in the Momentum Range From 5 to 9 GeV/c and for Interaction of π^- Mesons With Nuclei in the Momentum Range From 1.75 to 6.5 GeV/c. *Soviet J. Nucl. Phys.*, vol. 30, no. 6, Dec. 1979, pp. 805-813.

31. Townsend, Lawrence W.; and Wilson, John W.: *Tables of Nuclear Cross Sections for Galactic Cosmic Rays—Absorption Cross Sections.* NASA RP-1134, 1985.

32. Stehn, John R.; Goldberg, Murrey D.; Magurno, Benjamin A.; and Wiener-Chasman, Renate: Neutron Cross Sections. *Volume 1, Z = 1 to 20. BNL 325*, Second ed., Suppl. No. 2 (Physics—TID-4500, 32nd ed.), Sigma Center, Brookhaven National Lab. Associated Univ., Inc., May 1964.

33. Brodsky, Allen, ed.: *CRC Handbook of Radiation Measurement and Protection—General Scientific and Engineering Information, Volume I: Physical Science and Engineering Data.* CRC Press, Inc., c.1978.

34. Van Allen, James A.: The Nature and Intensity of the Cosmic Radiation. Chapter XIV of *Physics and Medicine of the Upper Atmosphere,* Clayton S. White and Otis O. Benson, Jr., eds., Univ. of New Mexico Press (Albuquerque), 1952, pp. 239-266.

35. Lord, J. J.: The Altitude and Latitude Variation in the Rate of Occurrence of Nuclear Disintegrations Produced in the Stratosphere by Cosmic Rays. *Phys. Review,* vol. 81, no. 6, second ser., Mar. 15, 1951, pp. 901-909.

36. Alsmiller, R. G., Jr.; Armstrong, T. W.; and Coleman, W. A.: The Absorbed Dose and Dose Equivalent From Neutrons in the Energy Range 60 to 3000 MeV and Protons in the Energy Range 400 to 3000 MeV. *Nucl. Sci. & Eng.*, vol. 42, no. 3, Dec. 1970, pp. 367-381.

37. Foelsche, Trutz; Mendell, Rosalind B.; Wilson, John W.; and Adams, Richard R.: *Measured and Calculated Neutron Spectra and Dose Equivalent Rates at High Altitudes; Relevance to SST Operations and Space Research.* NASA TN D-7715, 1974.

38. Heckman, H. H.: *Heavy Ion Fragmentation Experiments at the Bevatron.* NASA CR-142589, 1975.

39. Greiner, D. E.; Lindstrom, P. J.; Heckman, H. H.; Cork, Bruce; and Bieser, F. S.: Momentum Distributions of Isotopes Produced by Fragmentation of Relativistic ^{12}C and ^{16}O Projectiles. *Phys. Review Lett.*, vol. 35, no. 3, July 21, 1975, pp. 152-155.

40. Lindstrom, P. J.; Greiner, D. E.; Heckman, H. H.; Cork, Bruce; and Bieser, F. S.: *Isotope Production Cross Sections From the Fragmentation of ^{16}O and ^{12}C at Relativistic Energies.* LBL-3650 (NGR-05-003-513), Lawrence Berkeley Lab., Univ. of California, June 1975.

41. Serber, R.: Nuclear Reactions at High Energies. *Phys. Review,* vol. 72, no. 11, Dec. 1, 1947, pp. 1114-1115.

42. Rudstam, G.: Systematics of Spallation Yields. *Zeitschrift für Naturforschung,* vol. 21a, no. 7, July 1966, pp. 1027-1041.

43. Silberberg, R.; Tsao, C. H.; and Shapiro, M. M.: Semiempirical Cross Sections, and Applications to Nuclear Interactions of Cosmic Rays. *Spallation Nuclear Reactions and Their Applications,* B. S. P. Shen and M. Merker, eds., D. Reidel Publ. Co., c.1976, pp. 49-81.

44. Guzik, T. Gregory: The Low-Energy Galactic Cosmic Ray Carbon, Nitrogen, and Oxygen Isotopic Composition. *Astrophys. J.*, no. 2, pt. 1, Mar. 1, 1981, pp. 695-710.

45. Guzik, T. G.; Wefel, J. P.; Crawford, H. J.; Greiner, D. E.; Lindstrom, P. J.; Schimmerling, W.; and Symons, T. J. M.: Implications of New Measurements of ^{16}O $+ p \to$ ^{12,13}C, ^{14,15}N for the Abundances of C, N Isotopes at the Cosmic Ray Source. *19th International Cosmic Ray Conference, OG Sessions, Volume 2,* NASA CP-2376, 1985, pp. 80-83. (Available as OG 4.3-2.)

46. Bertini, Hugo W.; Guthrie, Miriam P.; and Culkowski, Arline H.: *Nonelastic Interactions of Nucleons and π-Mesons With Complex Nuclei at Energies Below 3 GeV.* ONRL-TM-3148, U.S. Atomic Energy Commission, Mar. 28, 1972.

47. *MECC-7 Intranuclear Cascade Code, 500-MeV Protons on 0-16. I4C Analysis Codes* (Programmed for H. W. Bertini). Available from Radiation Shielding Information Center, Oak Ridge National Lab., 1968.

48. Hellwege, K.-H., ed.: *Landolt-Börnstein Numerical Data and Functional Relationships in Science and Technology—Group I: Nuclear and Particle Physics, Volume 7, Elastic and Charge Exchange Scattering of Elementary Particles.* Springer-Verlag, 1973.

49. Hess, Wilmot N.: Summary of High-Energy Nucleon-Nucleon Cross-Section Data. *Reviews Modern Phys.*, vol. 30, no. 2, pt. I, Apr. 1958, pp. 368-401.

50. Wilson, John W.; and Costner, Christopher M.: *Nucleon and Heavy-Ion Total and Absorption Cross Section for Selected Nuclei.* NASA TN D-8107, 1975.

51. Fernbach, S.: Nuclear Radii as Determined by Scattering of Neutrons. *Reviews Modern Phys.*, vol. 30, no. 2, pt. 1, Apr. 1958, pp. 414–418.

52. Goldberg, Murrey D.; May, Victoria M.; and Stehn, John R.: *Angular Distributions in Neutron-Induced Reactions. Volume I, Z = 1 to 22.* BNL 400, Second ed., Vol. I, Sigma Center, Brookhaven National Lab., Oct. 1962.

53. Alsmiller, R. G., Jr.; Barish, J.; and Leimdorfer, M.: Analytic Representation of Nonelastic Cross Sections and Particle-Emission Spectra From Nucleon-Nucleus Collisions in the Energy Range 25 to 400 MeV. *Protection Against Space Radiation*, NASA SP-169, 1968, pp. 495–515.

54. Ranft, J.: The FLUKA and KASPRO Hadronic Cascade Codes. *Computer Techniques in Radiation Transport and Dosimetry*, Walter R. Nelson and Theodore M. Jenkins, eds., Plenum Press, c.1980, pp. 339–371.

55. Feshbach, H.; and Huang, K.: Fragmentation of Relativistic Heavy Ions. *Phys. Lett.*, vol. 47B, no. 4, Nov. 26, 1973, pp. 300–302.

56. Goldhaber, A. S.: Statistical Models of Fragmentation Processes. *Phys. Lett.*, vol. 53B, no. 4, Dec. 23, 1974, pp. 306–308.

57. Wilson, John W.: *Analysis of the Theory of High-Energy Ion Transport.* NASA TN D-8381, 1977.

58. Irving, D. C.; Alsmiller, R. G.; and Moran, H. S.: *Tissue Current-to-Dose Conversion Factors for Neutrons With Energies From 0.5 to 60 MeV.* ORNL-4032, U.S. Atomic Energy Commission, Aug. 1967.

59. Zerby, C. D.; and Kinney, W. E.: *Calculated Tissue Current-to-Dose Conversion Factors for Nucleons Below 400 MeV.* ORNL-TM-1038 (Contract No. W-7405-eng-26), Oak Ridge National Lab., May 1965.

60. Wilson, John W.; Townsend, Lawrence W.; Ganapol, Barry; Chun, Sang Y.; and Buck, Warren W.: Charged-Particle Transport in One Dimension. *Nucl. Sci. & Eng.*, vol. 99, no. 3, July 1988, pp. 285–287.

61. Ganapol, Barry D.; Wilson, John W.; and Townsend, Lawrence W.: Benchmark Solutions for the Galactic Ion Transport Equations. *Trans. American Nuclear Soc.*, vol. 56, 1988, pp. 276–277.

62. Wilson, John W.; Townsend, Lawrence W.; Ganapol, Barry D.; and Lamkin, Stanley L.: Methods for High Energy Hadronic Beam Transport. *Trans. American Nucl. Soc.*, vol. 56, June 1988, pp. 271–272.

63. Wilson, John W.: Environmental Geophysics and SPS Shielding. *Workshop on the Radiation Environment of the Satellite Power System*, Walter Schimmerling and Stanley B. Curtis, eds., LBL-8581 (Contract W-7405-ENG-48), Univ. of California, Sept. 15, 1978, pp. 33–116.

64. Adams, J. H., Jr.; Silberberg, R.; and Tsao, C. H.: *Cosmic Ray Effects on Microelectronics. Part 1: The Near-Earth Particle Environment.* NRL-MR-4506-PT-1, Naval Research Lab., Aug. 1981. (Available from DTIC as AD A103 897.)

65. Nealy, John E.; Wilson, John W.; and Townsend, Lawrence W.: *Solar-Flare Shielding With Regolith at a Lunar Base Site.* NASA TP-2869, 1989.

Table 3.4.1. Present Correction Factors for Rudstam's Formula

ΔA	Correction factor for—	
	^{12}C	^{16}O
1	1.3	1.5
2	.5	1.0
3	.3	1.0
4	.1	1.0
5	1.0	1.5
6	.35	.5
7		.5
8		.1
9		2.5
10		1.0

Table 3.4.2. Comparison of Oxygen Fragmentation Cross Sections σ of Reference 46 With Experiments of Reference 40 and Parametric Results of References 42 and 43

A_F	Fragmentation cross sections, σ, mb, from—			
	Bertini (ref. 46)	LBL (ref. 40)	Rudstam (ref. 42)	NRL (ref. 43)
16	7.0	0.02	8.7	
15	85.1	61.5	61.0	59.4
14	39.0	35.4	32.6	32.2
13	13.9	22.8	29.7	17.7
12	28.1	34.1	27.9	36.0
11	5.0	26.4	31.4	19.9
10	9.1	12.7	12.0	11.0
9	1.0	5.2	7.1	12.1
8	.2	1.23	2.1	14.7
7	1.1	22.2	27.8	19.4
6	3.8	13.9	18.0	16.7
Total	193.3	235.5	258.3	239.1

Table 3.4.3. Comparison of Carbon Fragmentation Cross Sections σ Measured in Experiments of Reference 40 With Two Simple Parameterizations

(a) ^{12}C at 1000A MeV

| A_F | Fragmentation cross sections, σ, mb, from— | | |
	LBL (ref. 40)	Rudstam (ref. 42)	NRL (ref. 43)
12	0.1	6.7	0
11	55.3	63.2	69.0
10	22.7	28.0	22.0
9	5.8	10.0	15.2
8	1.4	4.8	26.0
7	18.9	21.7	20.7
6	12.4	14.7	16.9
Total	116.6	149.1	169.8

(b) ^{12}C at 2000A MeV

| A_F | Fragmentation cross sections, σ, mb, from— | | |
	LBL (ref. 40)	Rudstam (ref. 42)	NRL (ref. 43)
12	0.09	6.2	0
11	57.0	60.4	58.5
10	22.7	27.8	20.5
9	6.20	10.4	14.2
8	1.6	5.2	24.1
7	20.49	24.4	19.9
6	14.8	17.2	16.7
Total	122.9	151.6	153.9

Table 3.5.1. Number of Evaporation Nucleons Produced in Nuclear Collisions

[Values in parentheses are modified and used in the code]

	Number of nucleons produced at—					
	25 MeV	200 MeV	400 MeV	1000 MeV	2000 MeV	3000 MeV
$A_t = 12$:						
$p \rightarrow p$	0.51	0.54	0.50	0.72	0.75	0.84
$p \rightarrow n$	0.026	0.32	0.35	0.79	0.79	0.79
$n \rightarrow p$	0.052	0.30	0.35	0.73	0.73	0.80
$n \rightarrow n$	0.43	0.57	0.52	0.77 (0.71)	0.71 (0.71)	0.73
$A_t = 16$:						
$p \rightarrow p$	0.62	0.73	0.71	0.84	0.89	0.98 (0.93)
$p \rightarrow n$	0.87	0.36	0.441	0.11 (0.87)	0.93 (0.87)	0.82 (0.87)
$n \rightarrow p$	0.12	0.47	0.53	0.86	0.86	0.89
$n \rightarrow n$	0.55	0.60	0.59	0.79	0.79	0.81
$A_t = 27$:						
$p \rightarrow p$	0.54	0.99	1.03	1.36	1.49	1.86
$p \rightarrow n$	0.37	0.61	0.62	1.29	2.03 (1.92)	1.52 (1.92)
$n \rightarrow p$	0.14	0.78	0.82	1.29	1.60	1.74
$n \rightarrow n$	0.75	0.76	0.71	1.34	1.51	1.60
$A_t = 40$:						
$p \rightarrow p$	0.50	1.03	1.06	1.74	2.32	2.93
$p \rightarrow n$	0.53	1.12	1.24	2.63	3.36	3.64
$n \rightarrow p$	0.12	0.74	0.84	1.60	2.29	2.67
$n \rightarrow n$	0.89	1.39	1.44	2.76	3.25	3.54
$A_t = 65$:						
$p \rightarrow p$	0.18	0.75	0.91	2.11	3.15	4.00
$p \rightarrow n$	1.04	2.33	2.65	3.97	4.79	5.37
$n \rightarrow p$	0.03	0.49	0.66	1.90	2.98	3.61
$n \rightarrow n$	1.46	2.77	2.90	4.17	4.99	5.49
$A_t = 80$:						
$p \rightarrow p$	0.10	0.60	1.07	2.2	3.18	4.89
$p \rightarrow n$	1.29	2.20	3.18	3.72	5.07	6.77
$n \rightarrow p$	0.02	0.53	0.79	1.87	2.91	4.53
$n \rightarrow n$	1.58	3.19	3.43	4.07	5.35	6.91
$A_t = 100$:						
$p \rightarrow p$	0.03	0.46	1.28	2.96	4.56	5.78
$p \rightarrow n$	1.53	1.97	3.72	5.46	7.04	8.17
$n \rightarrow p$	0.004	0.59	0.96	2.71	4.27	5.44
$n \rightarrow n$	1.67	3.60	3.97	5.63	7.31	8.33
$A_t = 132$:						
$p \rightarrow p$	0.01	0.61	1.03	2.68	4.51	6.32
$p \rightarrow n$	1.91	4.11	5.25	8.76	11.34	12.31
$n \rightarrow p$	0.001	0.47	0.81	2.51	4.47	5.98
$n \rightarrow n$	1.96	4.73	5.59	8.93	10.6	12.42
$A_t = 164$:						
$p \rightarrow p$	0.003	0.42	0.76	2.38	4.68	6.86
$p \rightarrow n$	2.17	5.79	7.07	12.09	15.7	16.45
$n \rightarrow p$	0.003	0.28	0.58	2.30	4.68	6.52
$n \rightarrow n$	2.26	5.96	7.07	12.3	14.6	16.51
$A_t = 207$:						
$p \rightarrow p$	0.001	0.21	0.44	2.23	5.19	7.39
$p \rightarrow n$	2.29	7.22	9.24	15.3	17.81	20.6
$n \rightarrow p$	0.00	0.10	0.30	2.10	4.88	7.05
$n \rightarrow n$	2.29	7.38	9.53	15.6	18.2	20.6

Table 3.5.2. Number of Cascade Nucleons Produced in Nuclear Collisions

	Number of nucleons produced at—					
	0.25 MeV	200 MeV	400 MeV	1000 MeV	2000 MeV	3000 MeV
$A_t = 12$:						
$p \to p$	0.58	1.43	1.63	1.95	2.15	2.48
$p \to n$	0.41	0.86	0.93	1.42	1.66	2.08
$n \to p$	0.42	0.90	0.92	1.43	1.65	1.91
$n \to n$	0.56	1.42	1.69	1.95	2.27	2.57
$A_t = 16$:						
$p \to p$	0.56	1.41	1.72	2.05	2.39	2.60
$p \to n$	0.38	0.90	0.98	1.47	1.86	2.19
$n \to p$	0.38	0.91	0.96	1.49	1.85	2.01
$n \to n$	0.54	1.43	1.70	2.05	2.52	2.70
$A_t = 27$:						
$p \to p$	0.46	1.38	1.67	2.29	2.86	3.19
$p \to n$	0.34	0.97	1.16	1.86	2.54	3.25
$n \to p$	0.32	0.93	1.01	1.69	2.28	2.71
$n \to n$	0.49	1.48	1.81	2.42	3.22	3.71
$A_t = 40$:						
$p \to p$	0.40	1.33	1.69	2.32	3.01	3.53
$p \to p$	0.30	1.04	1.24	2.46	3.52	4.48
$n \to p$	0.28	0.89	1.08	1.79	2.51	3.06
$n \to n$	0.45	1.49	1.88	2.99	4.13	4.83
$A_t = 65$:						
$p \to p$	0.30	1.21	1.69	2.35	3.16	3.87
$p \to n$	0.28	1.09	1.46	3.06	4.49	5.72
$n \to p$	0.21	0.86	1.08	1.88	2.75	3.41
$n \to n$	0.40	1.53	2.00	3.55	5.03	5.95
$A_t = 80$:						
$p \to p$	0.27	1.18	1.57	2.32	3.18	3.95
$p \to n$	0.25	1.08	1.45	3.27	4.92	6.35
$n \to p$	0.19	0.81	1.04	1.86	2.78	3.54
$n \to n$	0.36	1.51	1.98	3.78	5.40	6.64
$A_t = 100$:						
$p \to p$	0.25	1.15	1.55	2.29	3.20	4.04
$p \to n$	0.22	1.06	1.52	3.47	5.35	6.98
$n \to p$	0.17	0.78	1.08	1.84	2.44	3.67
$n \to n$	0.31	1.47	2.03	3.96	5.76	7.33
$A_t = 132$:						
$p \to p$	0.20	1.00	1.46	2.21	3.17	3.87
$p \to n$	0.20	1.11	1.57	3.31	5.20	7.91
$n \to p$	0.13	0.70	1.00	1.79	2.69	3.52
$n \to n$	0.28	1.45	2.10	3.86	6.86	8.29
$A_t = 164$:						
$p \to p$	0.16	0.90	1.36	2.13	3.15	3.69
$p \to n$	0.18	1.11	1.60	3.16	5.06	8.86
$n \to p$	0.11	0.63	0.88	1.72	2.55	3.39
$n \to n$	0.26	1.42	2.11	3.56	7.94	9.25
$A_t = 208$:						
$p \to p$	0.14	0.82	1.27	2.05	7.74	3.51
$p \to n$	0.16	1.03	1.71	2.97	7.23	9.77
$n \to p$	0.09	0.58	0.87	1.67	2.41	3.24
$n \to n$	0.23	1.36	2.10	3.36	7.63	10.21

Table 3.5.3. Evaporated Ion Yields From Nucleon-Nucleus Collisions

[Values in parentheses are for proton reactions]

| | Ion yields at— | | | |
	500 MeV	1000 MeV	2000 MeV	3000 MeV
$A_t = 16$:				
d	0.111 (0.094)	0.199 (0.237)	0.257 (0.265)	0.304 (0.311)
t	0.022 (0.029)	0.024 (0.025)	0.033 (0.025)	0.029 (0.029)
he	0.018 (0.034)	0.035 (0.043)	0.037 (0.052)	0.037 (0.048)
α	0.664 (0.400)	0.720 (0.696)	0.664 (0.624)	0.640 (0.667)
$A_t = 27$:				
d	0.126 (0.130)	0.245 (0.269)	0.380 (0.396)	0.442 (0.433)
t	0.028 (0.023)	0.048 (0.052)	0.063 (0.065)	0.072 (0.069)
he	0.042 (0.035)	0.067 (0.074)	0.073 (0.091)	0.083 (0.092)
α	0.370 (0.400)	0.550 (0.566)	0.597 (0.582)	0.577 (0.577)
$A_t = 65$:				
d	0.150 (0.171)	0.379 (0.390)	0.748 (0.766)	0.935 (0.987)
t	0.031 (0.035)	0.075 (0.068)	0.145 (0.145)	0.177 (0.191)
he	0.013 (0.014)	0.039 (0.056)	0.112 (0.124)	0.166 (0.177)
α	0.124 (0.137)	0.231 (0.231)	0.373 (0.377)	0.431 (0.441)
$A_t = 100$:				
d	0.174 (0.183)	0.456 (0.475)	1.01 (1.02)	1.44 (1.48)
t	0.028 (0.029)	0.080 (0.081)	0.207 (0.192)	0.269 (0.273)
he	0.012 (0.017)	0.055 (0.060)	0.162 (0.185)	0.249 (0.262)
α	0.158 (0.156)	0.320 (0.339)	0.490 (0.467)	0.549 (0.540)
$A_t = 207$:				
d	0.131 (0.152)	0.536 (0.565)	1.51 (1.57)	2.54 (2.54)
t	0.038 (0.037)	0.152 (0.163)	0.415 (0.424)	0.641 (0.644)
he	0.001 (0.002)	0.017 (0.017)	0.112 (0.106)	0.211 (0.239)
α	0.053 (0.063)	0.195 (0.210)	0.527 (0.514)	0.751 (0.746)

Table 3.5.4. Mean Energies of Light Nuclear Fragments Produced in Nucleon-Nucleus Collisions

[Values in parentheses are for proton reactions]

	Mean energies at—			
	500 MeV	1000 MeV	2000 MeV	3000 MeV
$A_t = 16$:				
n	5.55 (6.19)	7.91 (7.89)	9.55 (9.81)	11.1 (9.80)
p	6.10 (6.40)	8.33 (8.69)	9.71 (10.2)	10.3 (11.2)
d	8.53 (7.64)	12.2 (10.7)	14.9 (14.8)	16.3 (13.0)
t	6.40 (7.83)	10.6 (10.4)	12.5 (9.74)	13.7 (10.1)
he	12.1 (8.76)	11.8 (11.2)	11.1 (13.1)	12.9 (10.3)
α	9.36 (6.24)	12.6 (12.3)	13.1 (14.6)	13.6 (13.8)
$A_t = 27$:				
n	5.08 (5.09)	7.34 (7.48)	9.91 (10.5)	11.6 (12.0)
p	6.87 (6.90)	8.61 (8.92)	11.1 (11.9)	13.5 (13.7)
d	9.57 (9.42)	10.8 (11.2)	14.3 (14.8)	17.2 (17.4)
t	9.16 (9.54)	10.8 (11.1)	13.0 (13.9)	16.6 (13.7)
he	10.5 (10.8)	12.5 (12.8)	13.4 (14.1)	14.4 (14.5)
α	12.7 (13.4)	13.2 (13.6)	13.8 (13.8)	14.5 (14.6)
$A_t = 65$:				
n	4.24 (4.32)	5.67 (5.70)	7.92 (7.91)	9.67 (9.58)
p	8.25 (8.30)	9.66 (9.76)	12.1 (12.3)	14.4 (14.2)
d	9.88 (10.1)	13.5 (11.8)	13.8 (14.2)	15.6 (15.9)
t	10.0 (10.0)	11.7 (11.6)	13.7 (13.8)	15.1 (15.9)
he	14.6 (14.1)	16.4 (16.2)	17.5 (19.3)	19.5 (19.2)
α	12.7 (13.4)	13.2 (13.6)	13.8 (13.8)	14.5 (14.6)
$A_t = 100$:				
n	3.90 (3.90)	5.13 (5.16)	7.11 (7.04)	8.61 (8.74)
p	9.63 (9.62)	11.0 (11.0)	12.9 (13.2)	14.6 (14.7)
d	11.0 (11.1)	12.5 (12.6)	14.4 (15.0)	16.1 (16.0)
t	11.3 (11.7)	12.6 (13.0)	14.7 (14.3)	15.5 (16.5)
he	17.8 (18.7)	18.6 (18.8)	20.9 (20.6)	21.8 (22.2)
α	16.5 (16.5)	16.8 (16.9)	17.5 (17.5)	17.6 (17.6)
$A_t = 207$:				
n	3.28 (3.27)	4.37 (4.33)	5.83 (5.78)	6.90 (6.95)
p	12.5 (12.5)	12.2 (13.4)	14.9 (14.9)	16.2 (16.3)
d	13.2 (13.2)	14.4 (14.2)	16.0 (16.8)	17.4 (17.8)
t	13.6 (13.8)	5.0 (15.3)	16.6 (16.8)	17.4 (17.8)
he	24.1 (27.0)	26.2 (26.5)	28.0 (27.8)	29.1 (28.5)
α	25.3 (25.7)	26.0 (26.3)	26.4 (26.3)	25.9 (26.4)

Table 3.5.5. σ_p for ^{16}O Fragments Produced by 2.1 GeV Protons

| Fragment | Value of σ_p, MeV/c, from— | | |
	Experiments (ref. 39)	Present work	Greiner (ref. 39)
^{15}O	94 ± 3	80.0	83.8
^{14}O	99 ± 6	109.5	113.1
^{13}O	143 ± 14	129.2	133.5
^{16}N	54 ± 11	55.0	
^{15}N	95 ± 3	80.0	82.8
^{14}N	112 ± 3	109.5	113.0
^{13}N	134 ± 2	129.2	133.5
^{12}N	153 ± 11	143.4	148.1
^{15}C	125 ± 19	80.0	82.8
^{14}C	125 ± 3	109.5	113.10
^{13}C	130 ± 3	129.2	133.5
^{12}C	120 ± 4	143.36	148.09
^{11}C	162 ± 5	153.45	158.5
^{10}C	190 ± 9	160.3	165.6
^{13}B	166 ± 10	129.2	133.5
^{12}B	163 ± 8	143.4	148.1
^{11}B	160 ± 2	153.5	158.5
^{10}B	175 ± 7	160.3	165.6
^{8}B	175 ± 22	165.5	171.0
^{11}Be	197 ± 20	153.5	158.5
^{10}Be	159 ± 6	160.0	165.0
^{9}Be	166 ± 7	164.24	169.66
^{7}Be	166 ± 2	164.24	169.66
^{9}Li	188 ± 15	164.24	169.66
^{8}Li	170 ± 13	165.4	171.0
^{7}Li	163 ± 4	164.24	169.66
^{6}Li	141 ± 7	160.0	169.66
^{6}He	167 ± 20	160.0	165.0

Table 3.5.6. Average Recoil Energy $\overline{E}$ of ^{16}O Fragments Produced by 2.1 GeV Protons

| Fragment | Average energy value, $\overline{E}$, MeV, from— | | |
	Bertini (ref. 46)	Present results	Experiments (ref. 39)
^{16}F	2.65	1.01	
^{15}F	4.19	.69	
^{16}O	1.05	1.01	1.01
^{15}O	.52	.69	.88
^{14}O	1.82	1.37	1.12
^{13}O	4.24	2.05	2.51
^{16}N	1.11	1.01	.30
^{15}N	.63	.69	.96
^{14}N	1.12	1.37	1.42
^{13}N	1.84	2.05	2.20
^{12}N	3.85	2.74	3.11
^{11}N	5.95	3.42	3.64
^{14}C	1.62	1.34	1.78
^{13}C	1.97	2.05	2.07
^{12}C	2.64	2.74	1.91
^{11}C	4.70	3.42	3.81
^{10}C	5.58	4.11	5.76
^{9}C	4.41	4.79	5.10
^{13}B	2.35	2.05	3.38
^{12}B	3.43	2.74	3.53
^{11}B	4.33	3.71	3.42
^{10}B	4.79	4.11	4.89
^{9}B	1.19	4.79	
^{10}Be	4.53	4.11	4.03
^{9}Be	8.76	4.79	4.89
^{10}Li	4.61	4.11	
^{9}Li	2.26	4.79	6.27
^{8}Li	4.41	5.48	5.76
^{7}Li	4.75	6.16	6.06
^{6}Li	5.76	6.85	5.29

Table 3.5.7. Comparison of Fragment Energy-Transfer Cross Sections
$E\sigma$ of Bertini With Experiments of Greiner/Lindstrom and Present Results

A_F	Energy transfer cross sections, $E\sigma$, MeV-mb, from—		
	Bertini (ref. 46)	Greiner/Lindstrom (refs. 39 and 40)	Present results
16	5.04	0.0006	0.26
15	60.6	56.9	56.4
14	48.8	51.7	47.6
13	37.6	48.3	62.9
12	85.8	68.2	55.8
11	37.9	99.1	117.9
10	52.8	62.0	58.6
9	6.5	25.7	35.1
8	2.5	7.1	12.1
7	6.11	121.7	152.4
6	31.4	73.4	95.1
Total	375.1	614.1	694.2

Table 4.1.1. Ratio of Numerical Solution to Analytic Solution of Equation (4.1.23)
for 500-MeV Protons on a Water Shield

E, MeV	Ratio for shield thickness, x, g/cm^2, of—				
	10	20	40	60	80
0.1	1.000	1.000	1.004	0.998	1.023
19.5	1.000	.999	1.004	.997	1.024
120.9	1.000	.999	1.002	1.008	1.046
333.3	1.003	.994	1.037	.963	
454.1	1.031				

Table 4.1.2. Ratio of Numerical Solution to Analytic Solution of Equation (4.1.26)
for Continuous "Space" Proton Spectral Input on a Water Shield

E, MeV	Ratio for shield thickness, x, g/cm^2, of—				
	10	20	40	60	80
0.1	0.994	0.995	0.998	0.999	0.999
11.2	.994	.996	.999	1.001	1.000
36.3	.997	.998	1.002	1.003	1.005
118.1	1.001	1.003	1.005	1.006	1.004
383.9	.997	1.000	.991	1.000	.996

Table 5.1. Energy Deposition of 0.5–10 MeV Neutrons

[Values in parentheses are from present calculations]

Incident energy, MeV	Depth, cm	Energy deposition from Monte Carlo and present calculations, MeV			
		Proton		Heavy ion	
0.5	0-1 (1)	0.1107	(0.0856)	0.0073	(0.0076)
	1-2	.0986		.0066	
	4-5 (5)	.0418	(.0135)	.0028	(.0026)
	5-6	.0331		.0018	
	9-10 (10)	.0074	(.0018)	.0003	(.0006)
	10-11	.0059		.0002	
	14-15 (15)	.0006	(.0013)		(.0001)
	15-16	.0007			
	19-20 (20)	.0002	(.0002)		
	20-21	.0001			
2	0-1 (1)	0.2138	(0.1887)	0.0147	(0.0135)
	1-2	.1984		.0133	
	4-5 (5)	.1539	(.0818)	.0110	(.0092)
	5-6	.1349		.0105	
	9-10 (10)	.0770	(.0298)	.0054	(.0050)
	10-11	.0741		.0061	
	14-15 (15)	.0301	(.0226)	.0026	(.0024)
	15-16	.0240		.0019	
	19-20 (20)	.0091	(.0097)	.0008	(.0011)
	20-21	.0114		.0009	
10	0-1 (1)	0.3520	(0.3377)	0.0339	(0.0358)
	1-2	.3284		.0342	
	4-5 (5)	.3220	(.2539)	.0345	(.0288)
	5-6	.2977		.0266	
	9-10 (10)	.2674	(.1759)	.0257	(.0214)
	10-11	.2661		.0225	
	14-15 (15)	.2161	(.1411)	.0203	(.0156)
	15-16	.2211		.0198	
	19-20 (20)	.1635	(.1010)	.0150	(.0111)
	20-21	.1291		.0149	
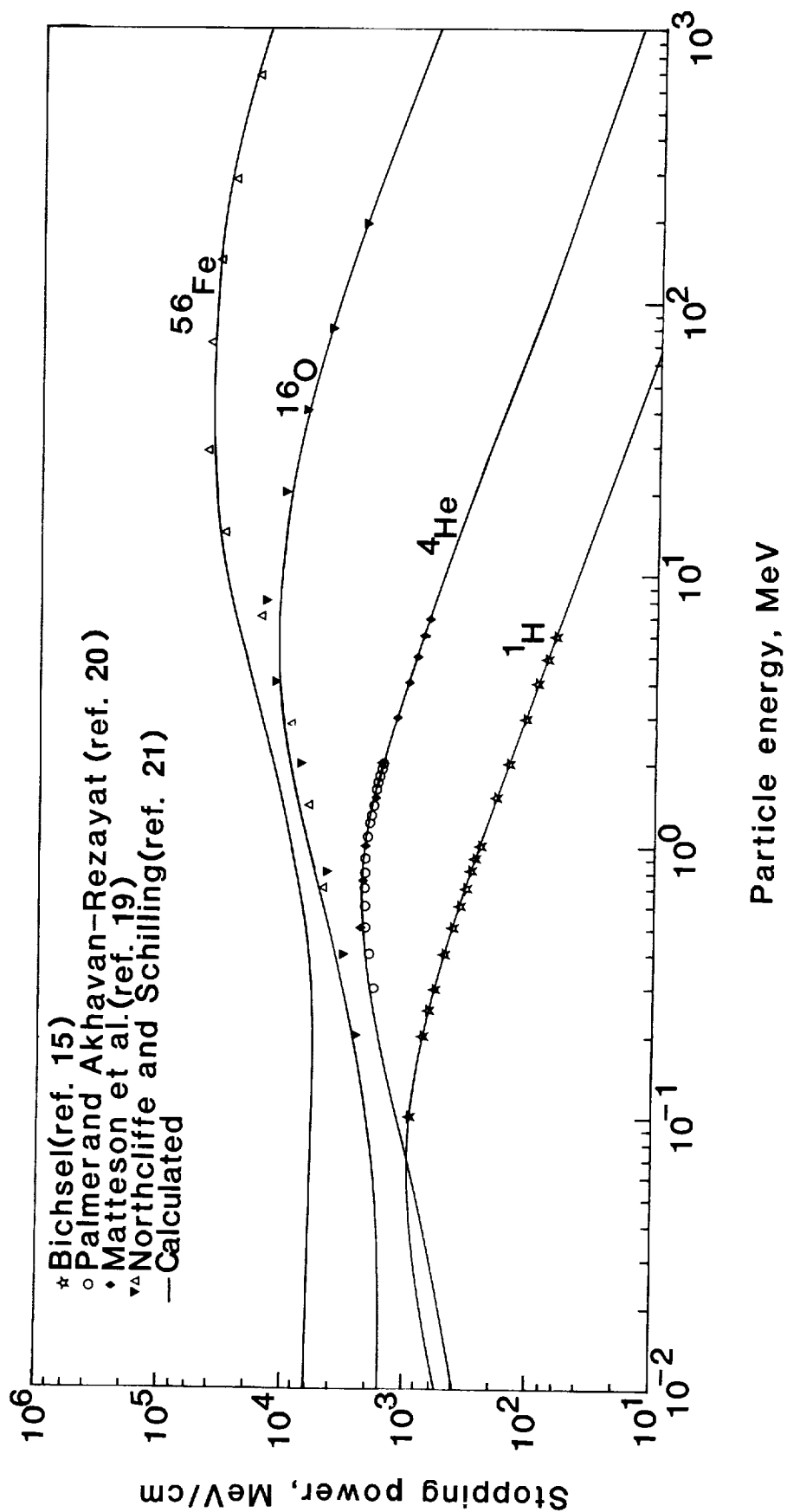
Figure 1. Calculated and experimental stopping powers in water for typical cosmic ray ions as a function of kinetic energy.
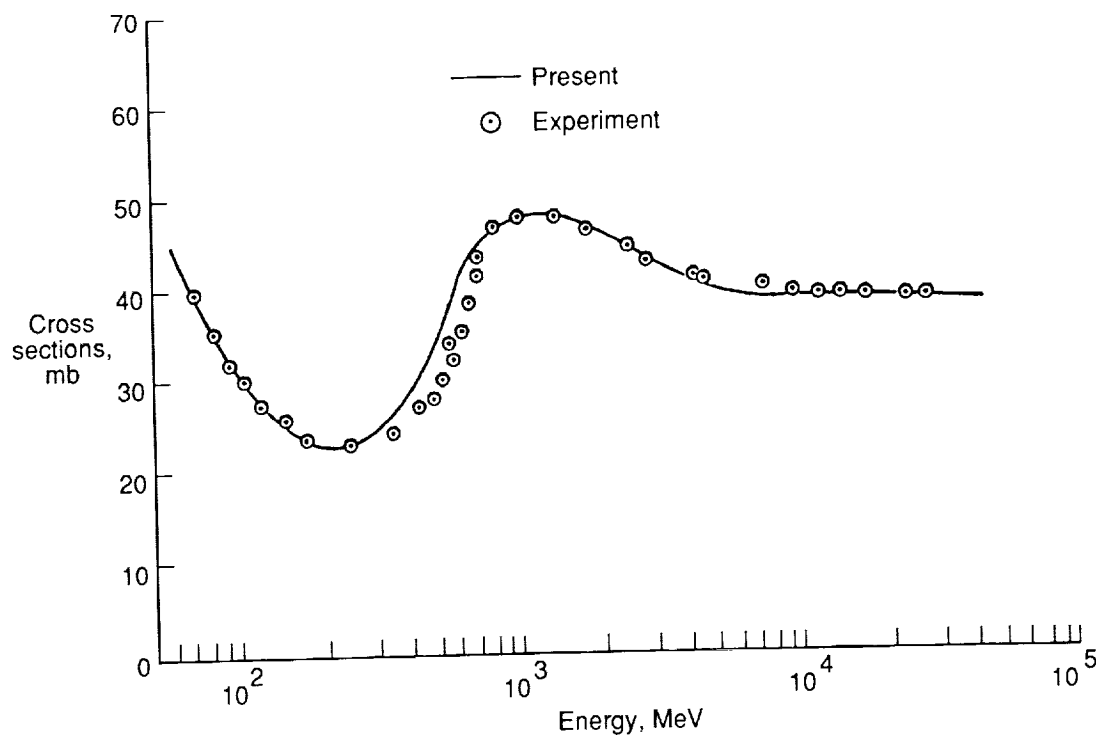
Figure 2. The total proton-proton cross section of the present formalism compared with various experiments.
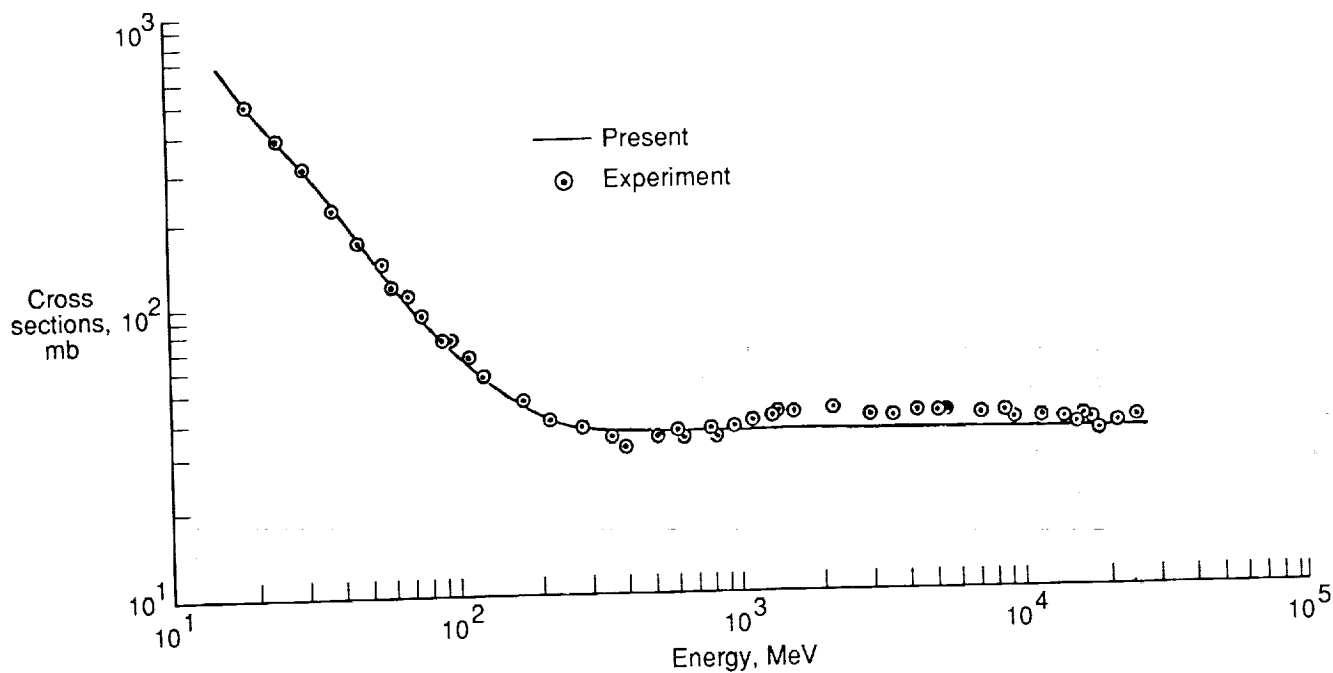
Figure 3. The total neutron-proton cross section of the present formalism compared with various experiments.
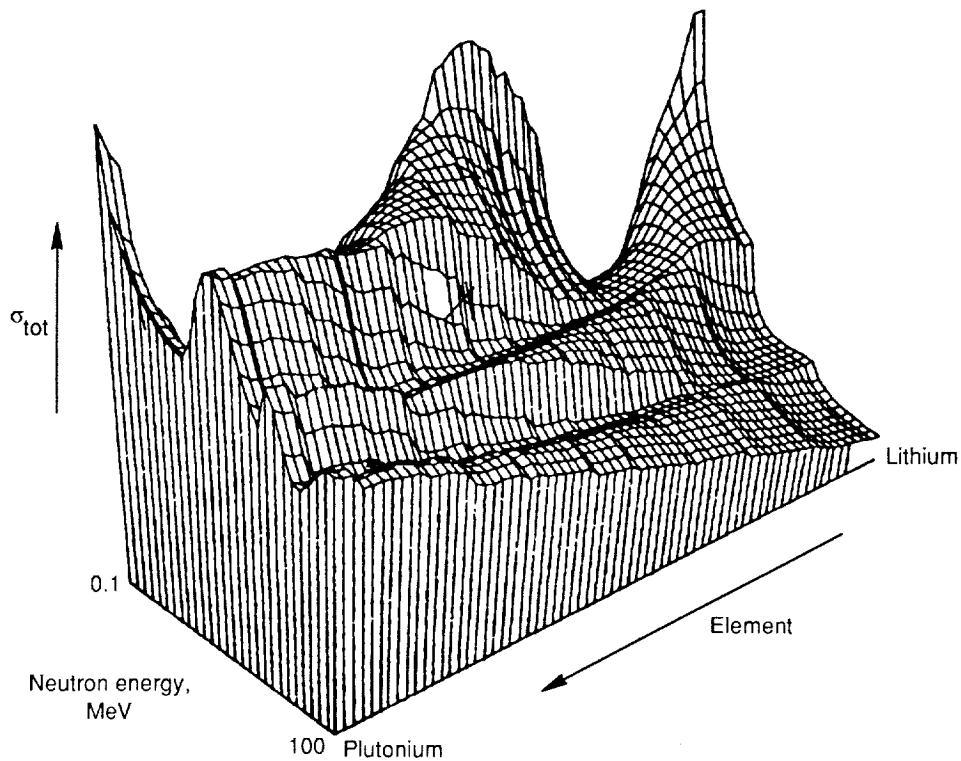
Figure 4. The total neutron-nucleus cross section according to the Ramsauer resonance formalism.
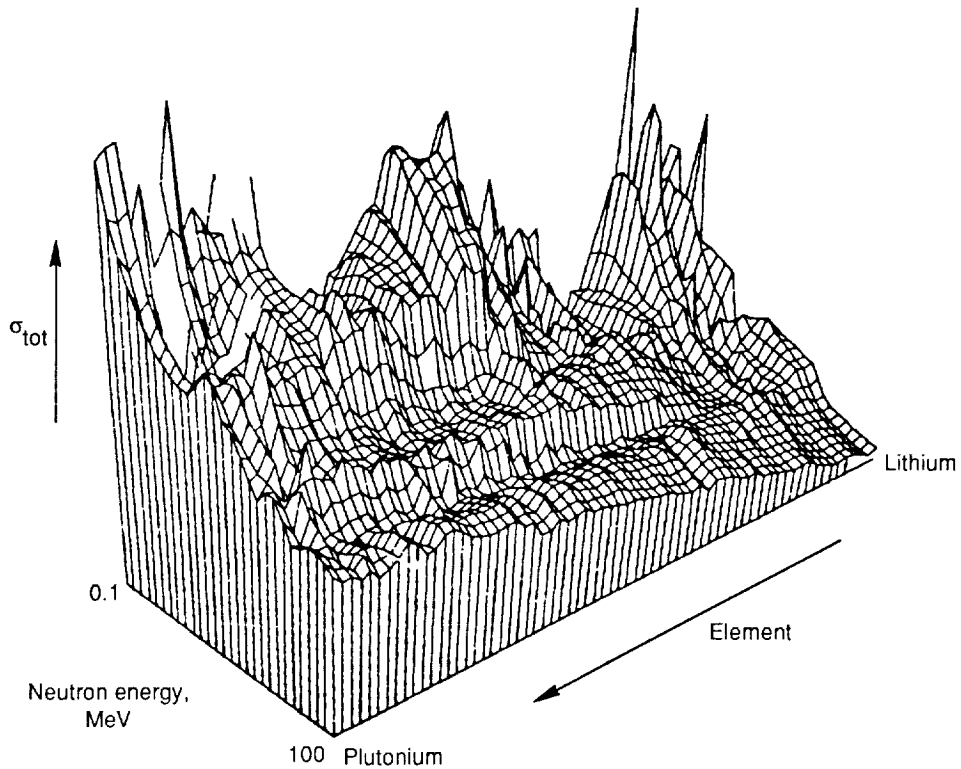
Figure 5. The total neutron cross section according to reference 27.
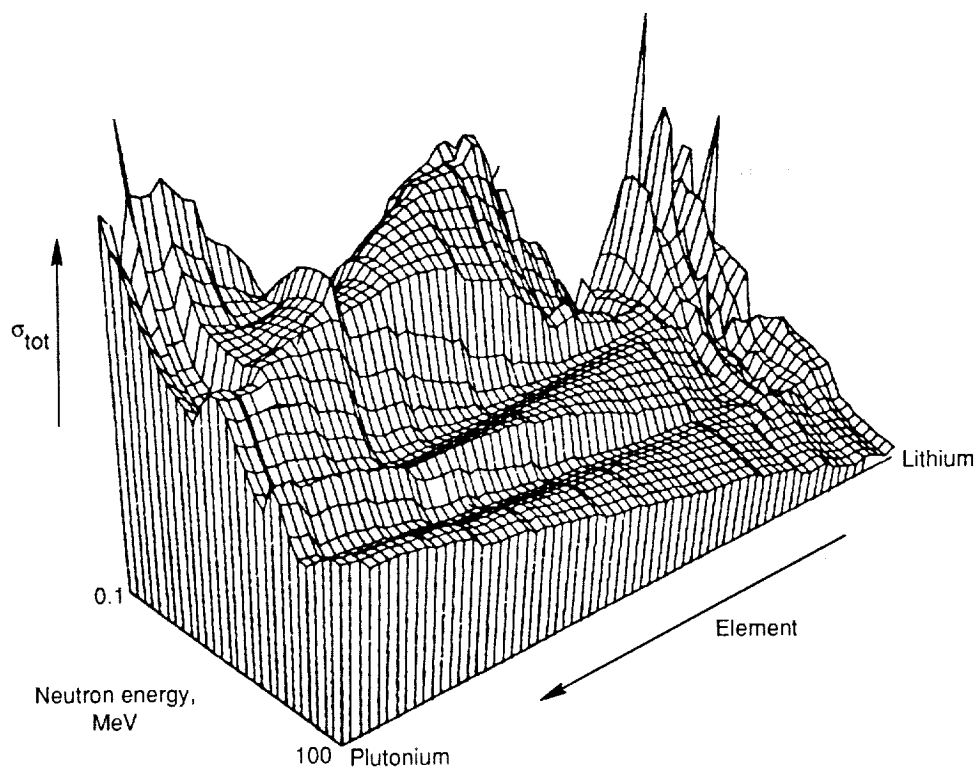
Figure 6. The total neutron-nucleus cross section according to the present formalism.
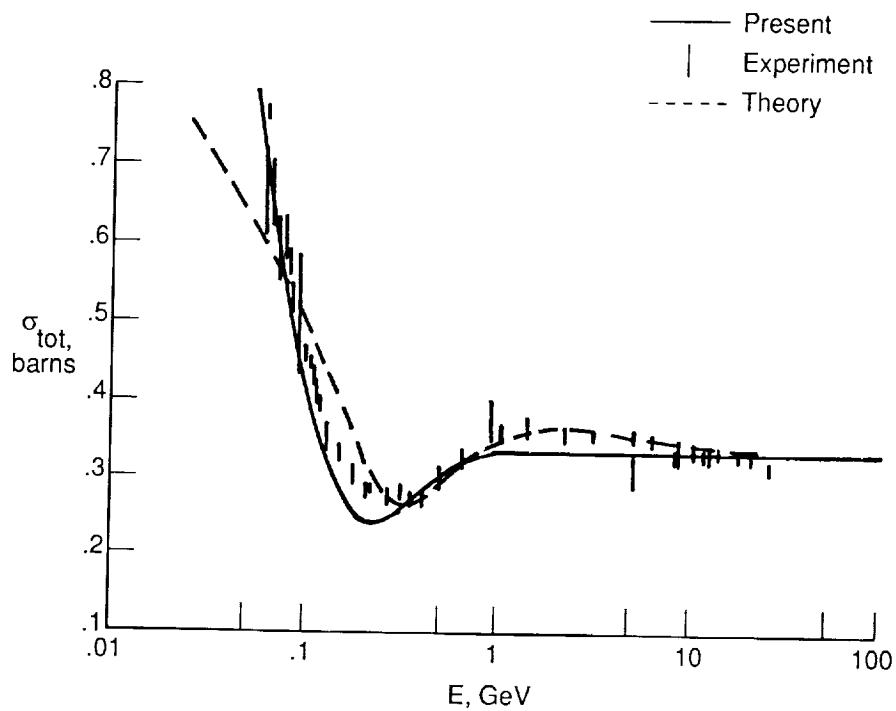
Figure 7. The total nucleon-carbon cross section according to the present formalism, the theory of Townsend, Wilson, et al. (ref. 28), and various experiments.
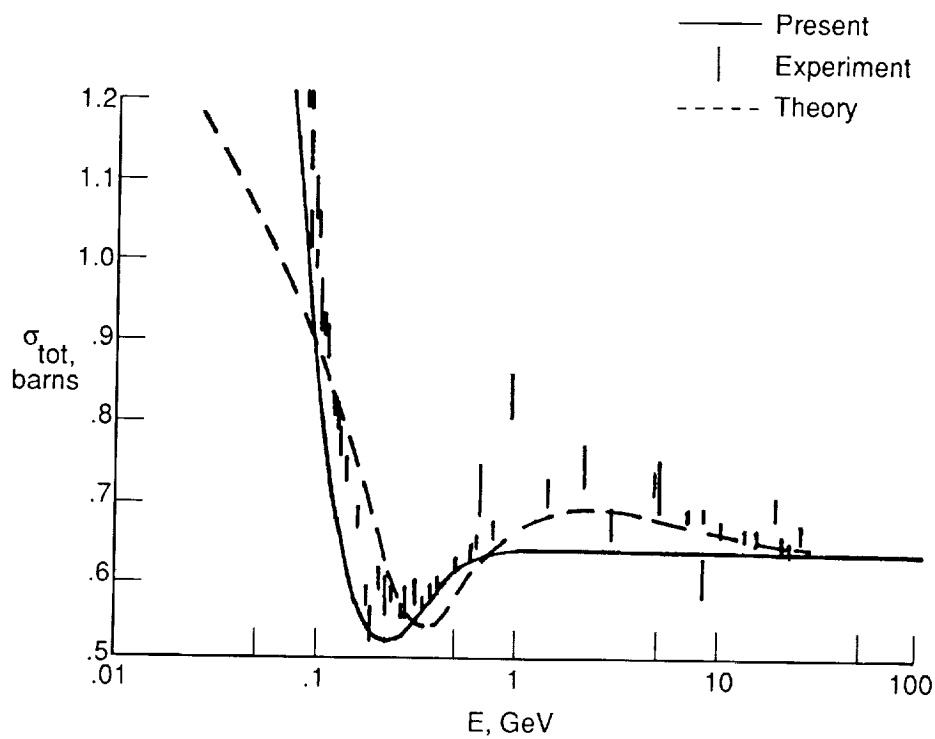
Figure 8. The total nucleon-aluminum cross section according to the present formalism, the theory of Townsend, Wilson, et al. (ref. 28), and various experiments.
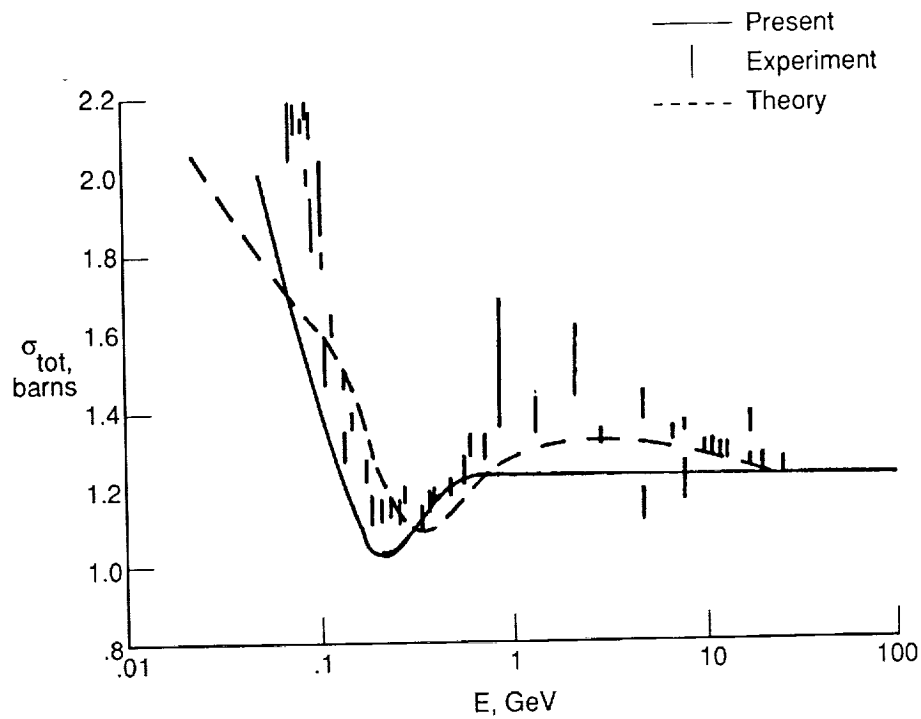
Figure 9. The total nucleon-copper cross section according to the present formalism, the theory of Townsend, Wilson, et al. (ref. 28), and various experiments.
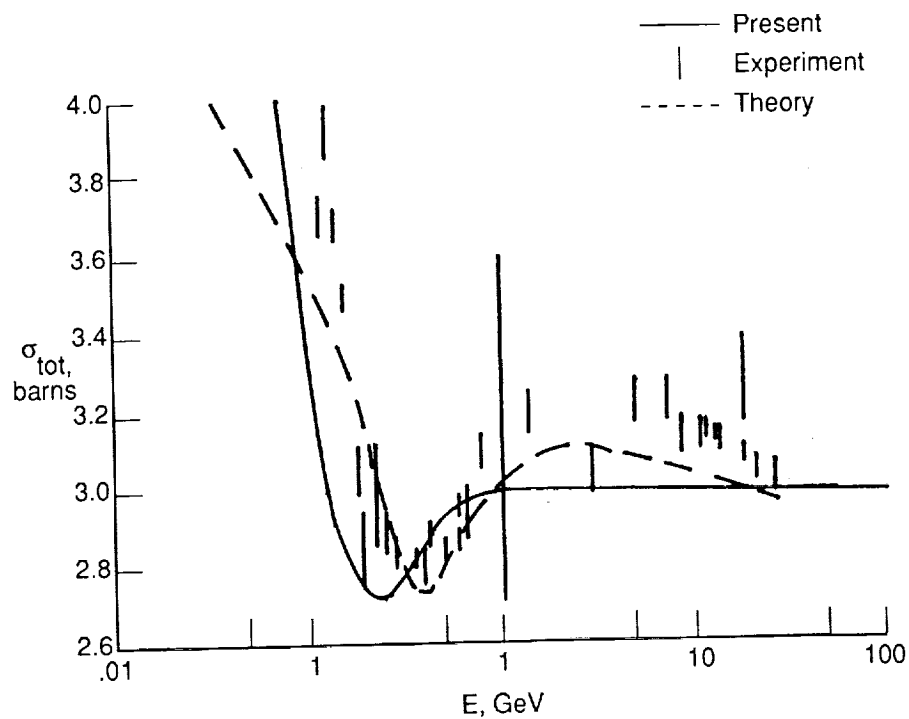
Figure 10. The total nucleon-lead cross section according to the present formalism, the theory of Townsend, Wilson, et al. (ref. 28), and various experiments.

46
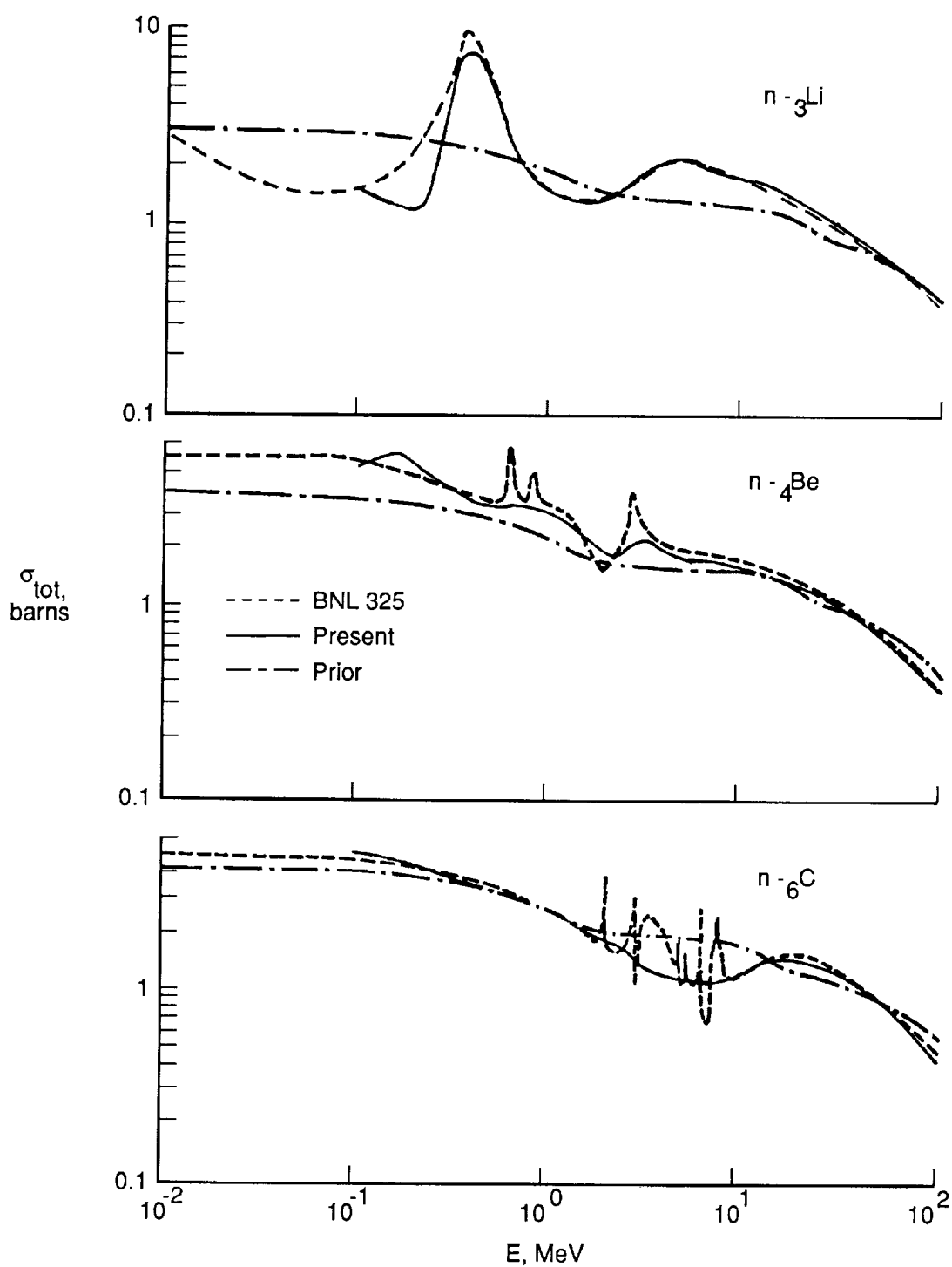
Figure 11. The total neutron-nucleus cross sections of $_3$Li, $_4$Be, and $_6$C according to the prior data base (ref. 1), the present formalism, and an evaluated data base (ref. 27).
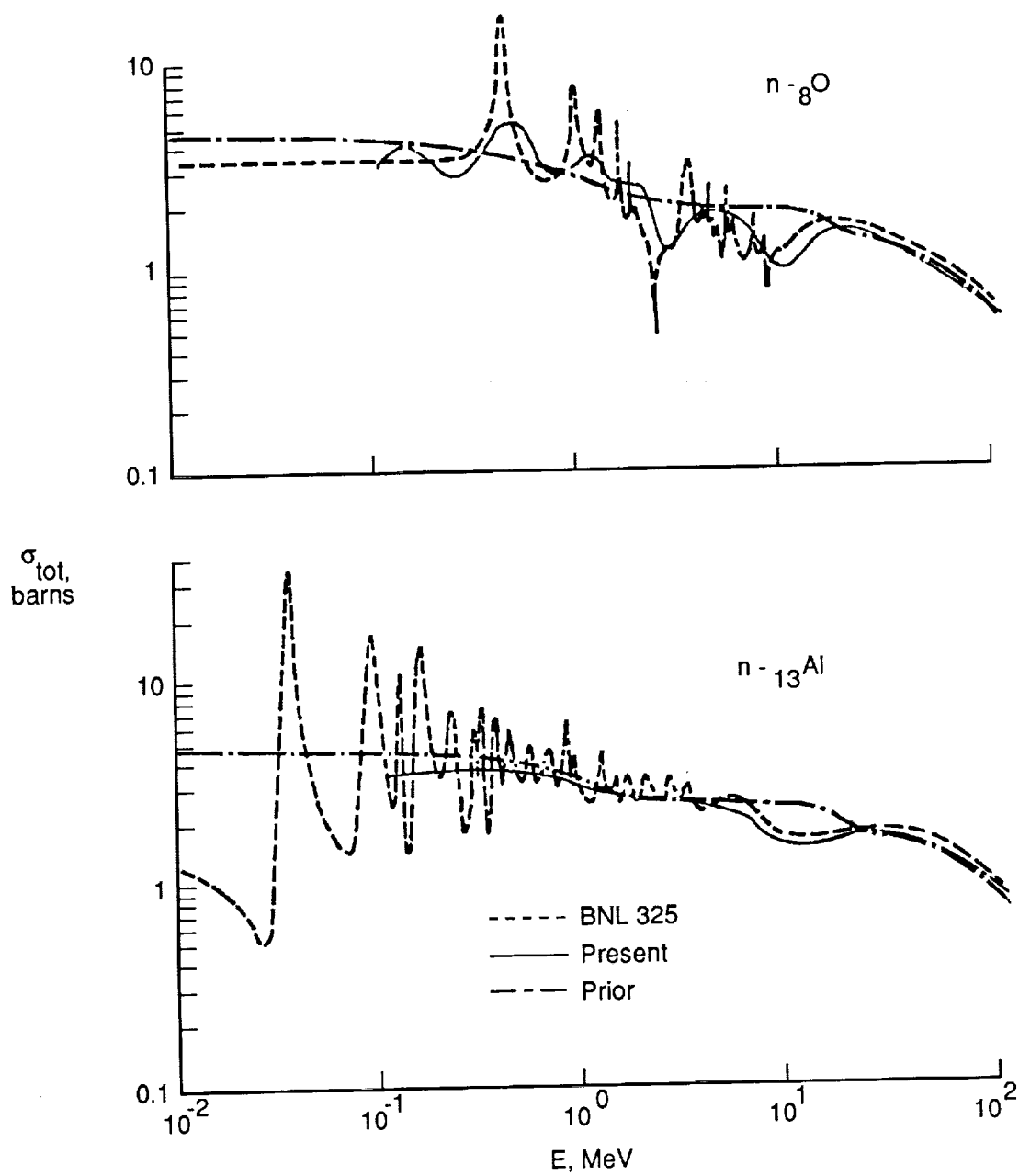
Figure 12. The total neutron-nucleus cross sections of $_8$O and $_{13}$Al according to the prior data base (ref. 1) the present formalism, and an evaluated data base (ref. 27).
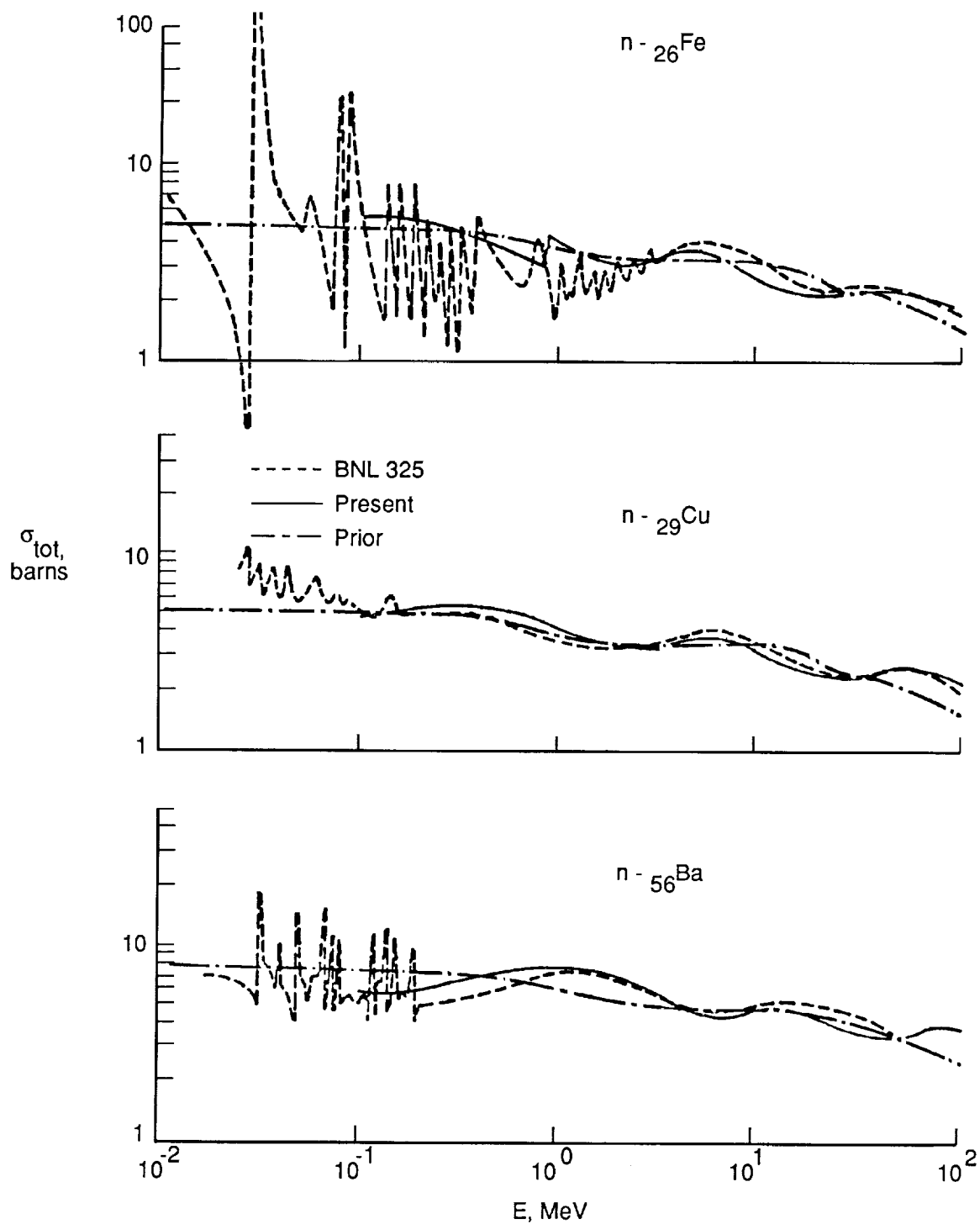
Figure 13. The total neutron-nucleus cross sections of $_{26}$Fe, $_{29}$Cu, and $_{56}$Ba according to the prior data base (ref. 1), the present formalism, and an evaluated data base (ref. 27).
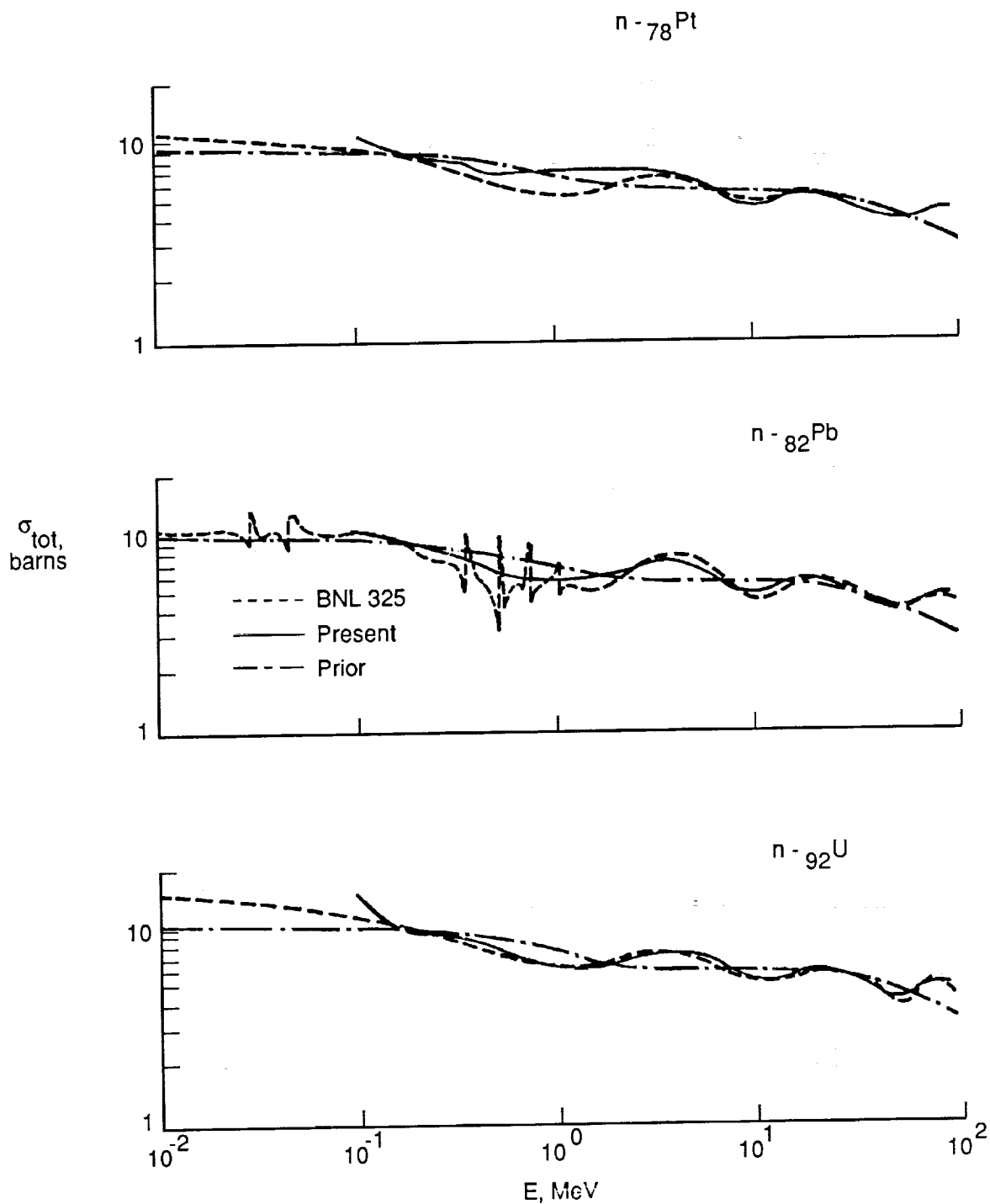
Figure 14. The total neutron-nucleus cross sections of $_{78}$Pt, $_{82}$Pb, and $_{92}$U according to the prior data base (ref. 1), the present formalism, and an evaluated data base (ref. 27).
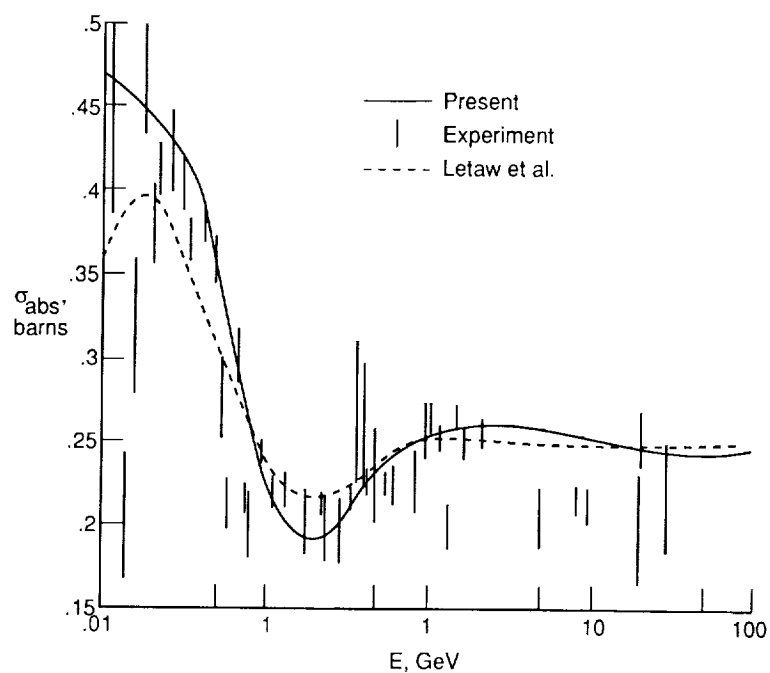
Figure 15. The neutron-carbon absorption cross section according to the present formalism compared with Letaw et al. (ref. 29) and various experiments.
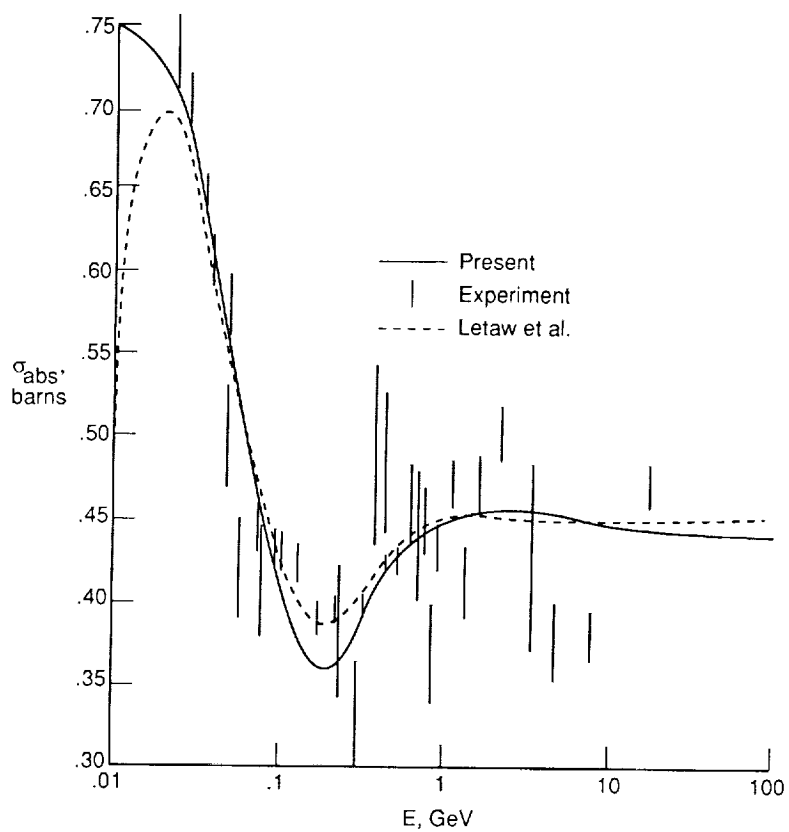
Figure 16. The neutron-aluminum absorption cross section according to the present formalism compared with Letaw et al. (ref. 29) and various experiments.
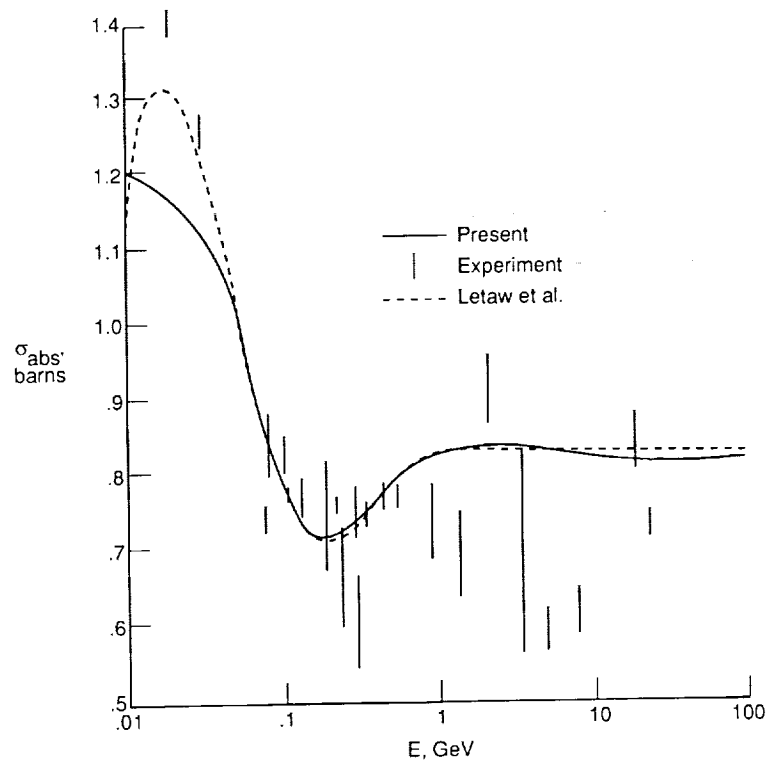
Figure 17. The neutron-copper absorption cross section according to the present formalism compared with Letaw et al. (ref. 29) and various experiments.
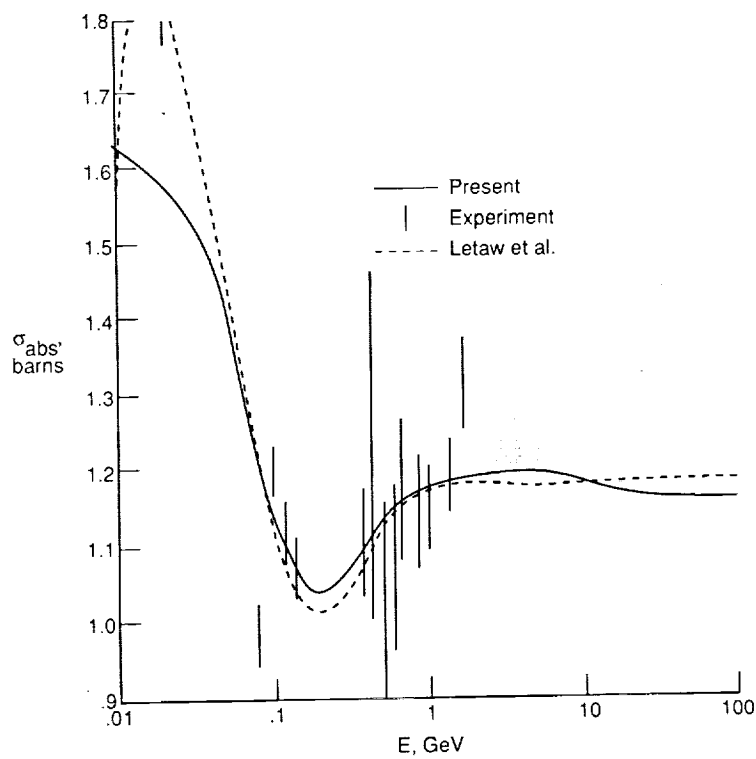
Figure 18. The neutron-silver absorption cross section according to the present formalism compared with Letaw et al. (ref. 29) and various experiments.
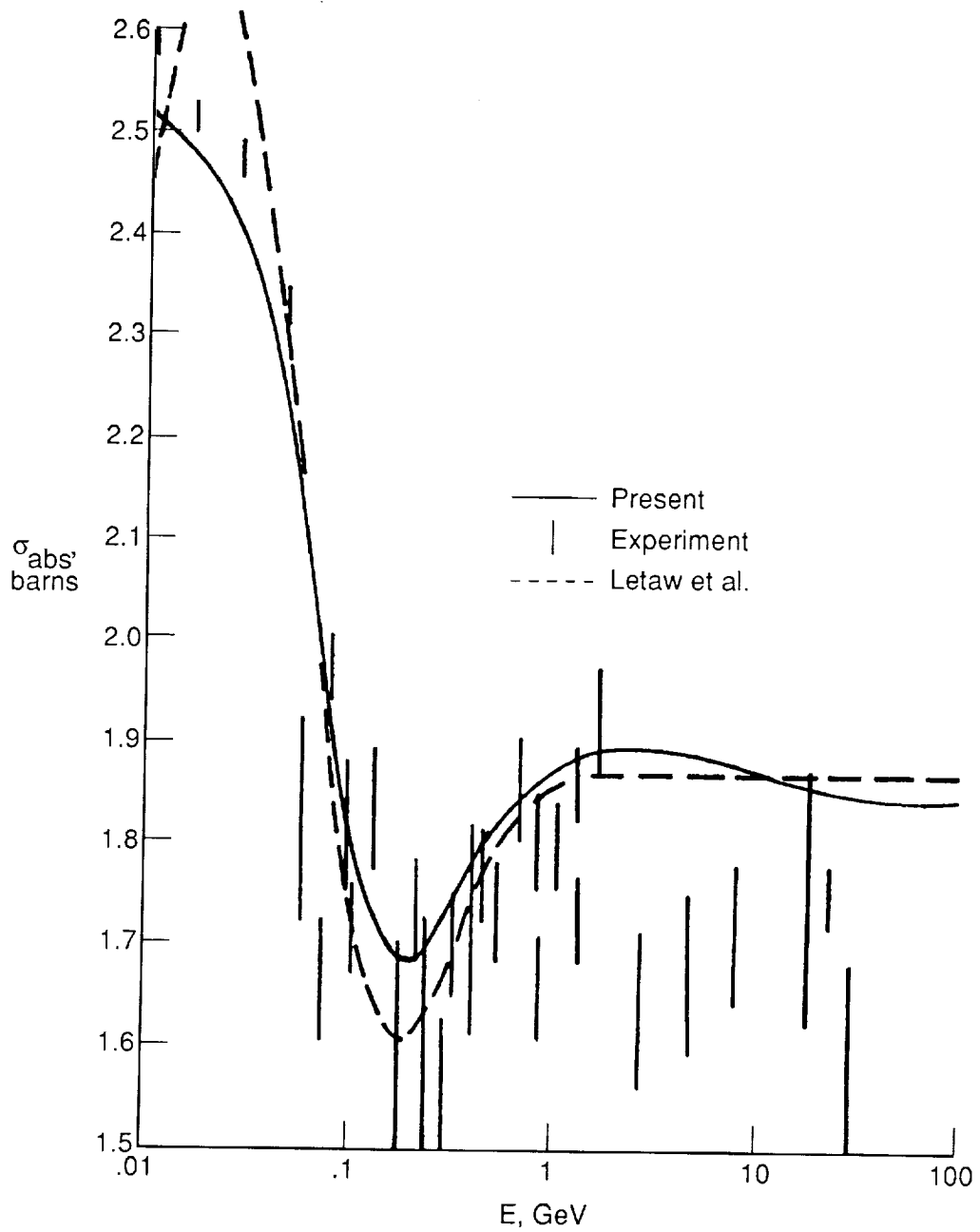
Figure 19. The neutron-lead absorption cross section according to the present formalism compared with Letaw et al. (ref. 29) and various experiments.
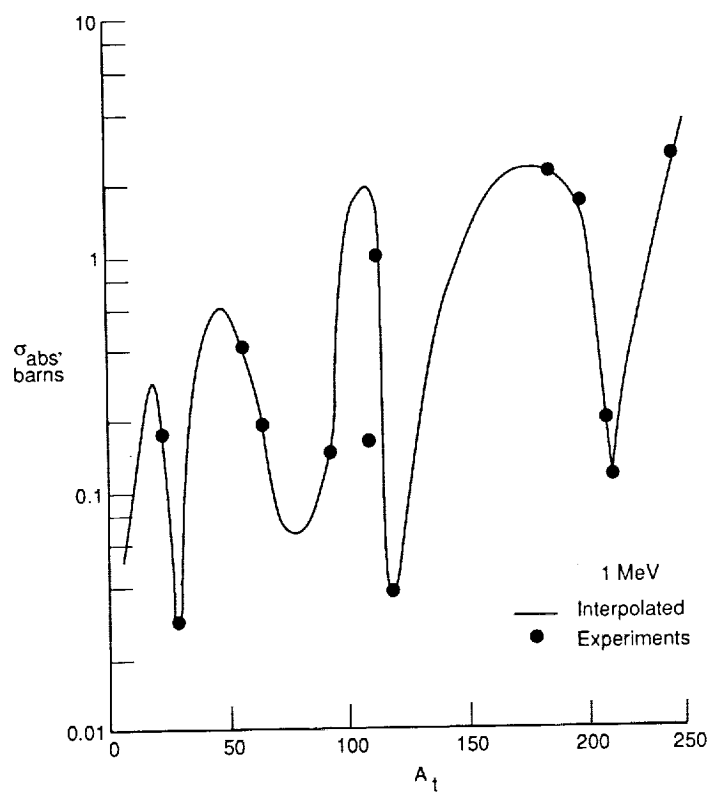
Figure 20. The neutron-nucleus absorption cross sections at 1 MeV of the present formalism compared with various experiments.
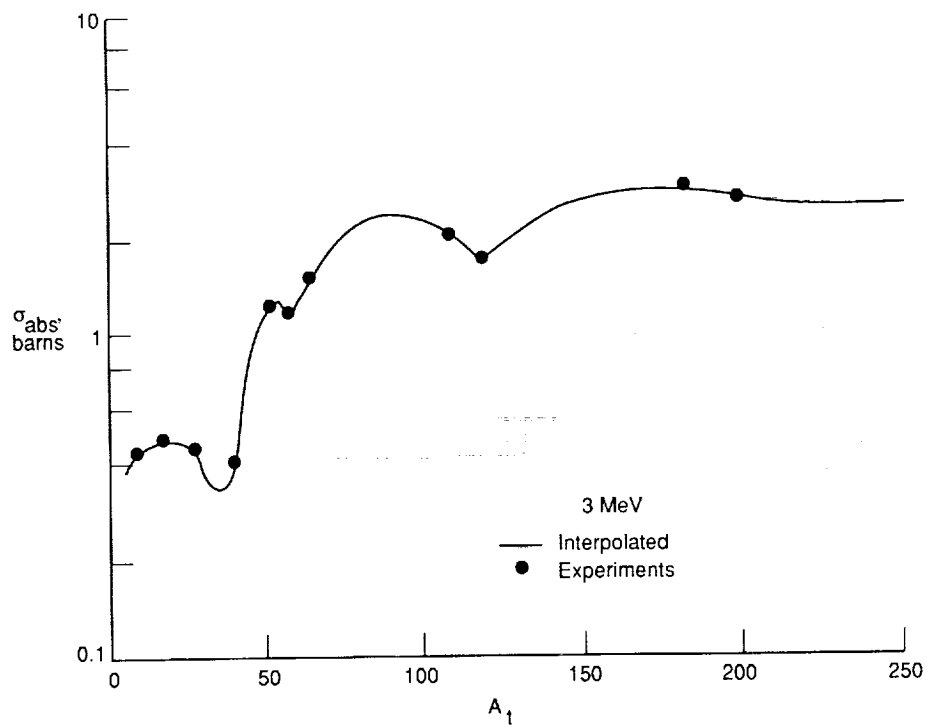
Figure 21. The neutron-nucleus absorption cross sections at 3 MeV of the present formalism compared with various experiments.
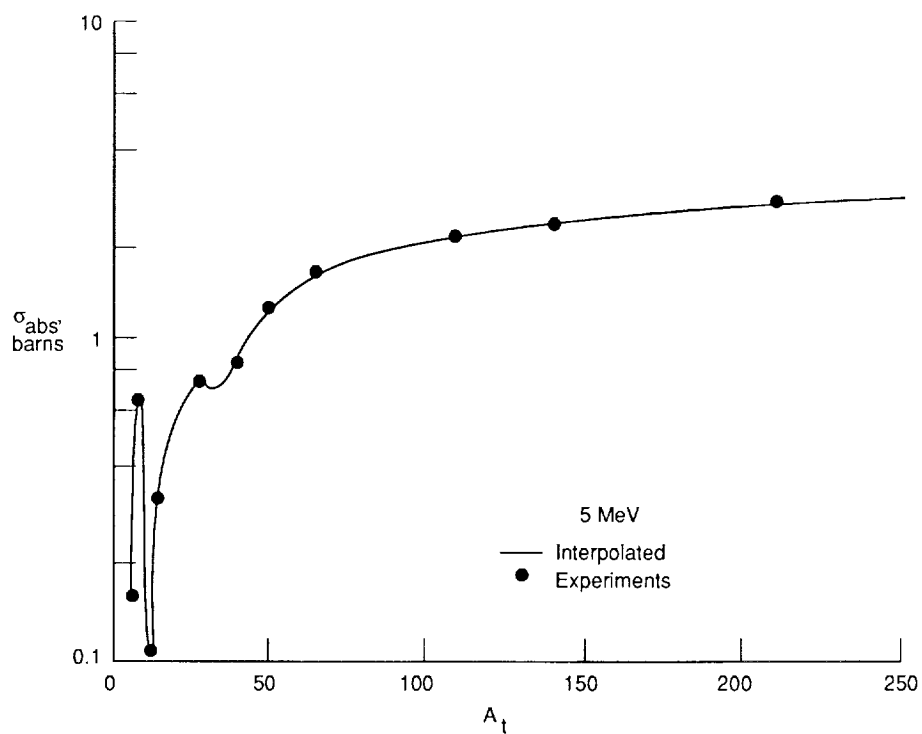
Figure 22. The neutron-nucleus absorption cross sections at 5 MeV of the present formalism compared with various experiments.
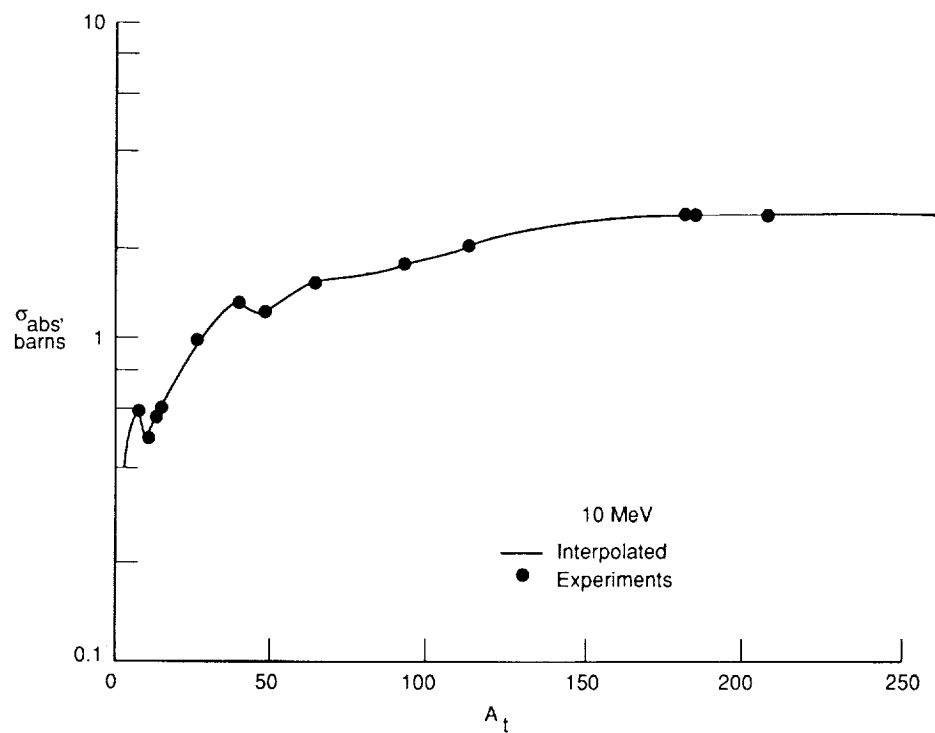
Figure 23. The neutron-nucleus absorption cross sections at 10 MeV of the present formalism compared with various experiments.
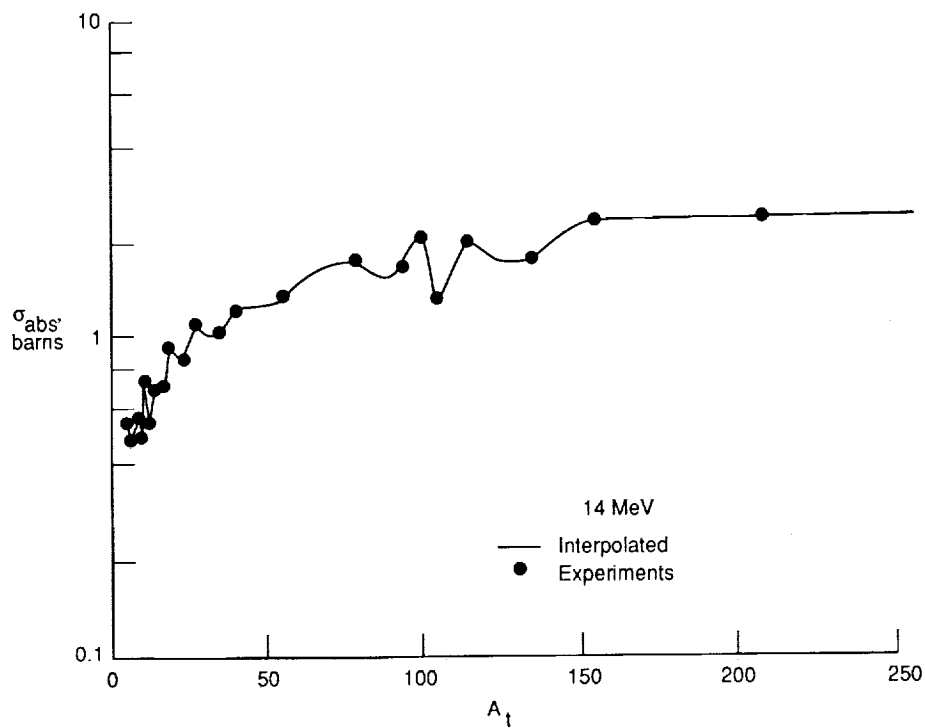
Figure 24. The neutron-nucleus absorption cross sections at 14 MeV of the present formalism compared with various experiments.
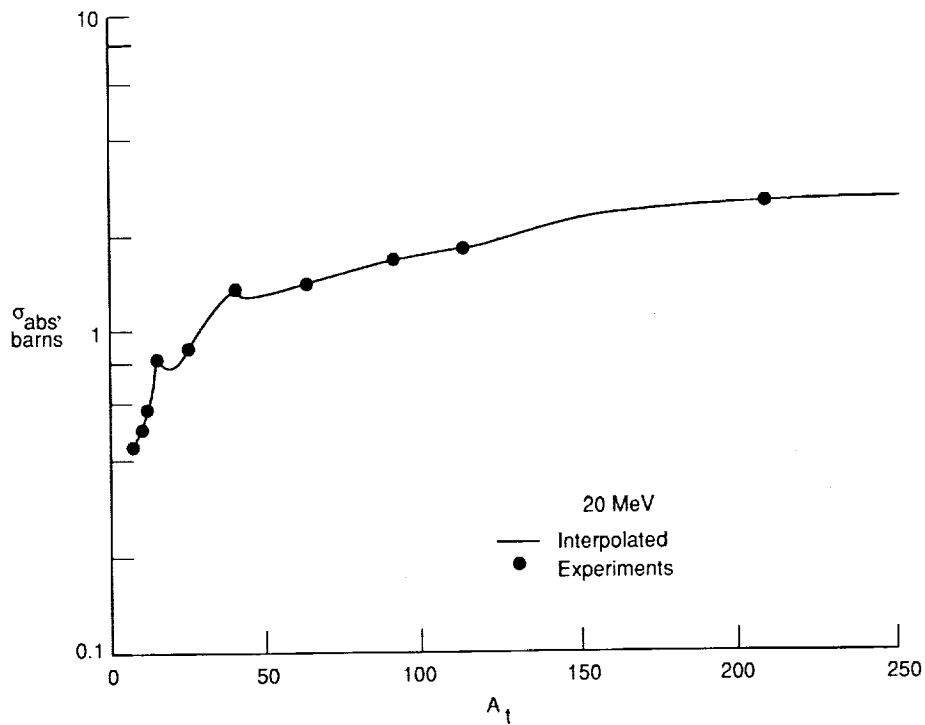
Figure 25. The neutron-nucleus absorption cross sections at 20 MeV of the present formalism compared with various experiments.
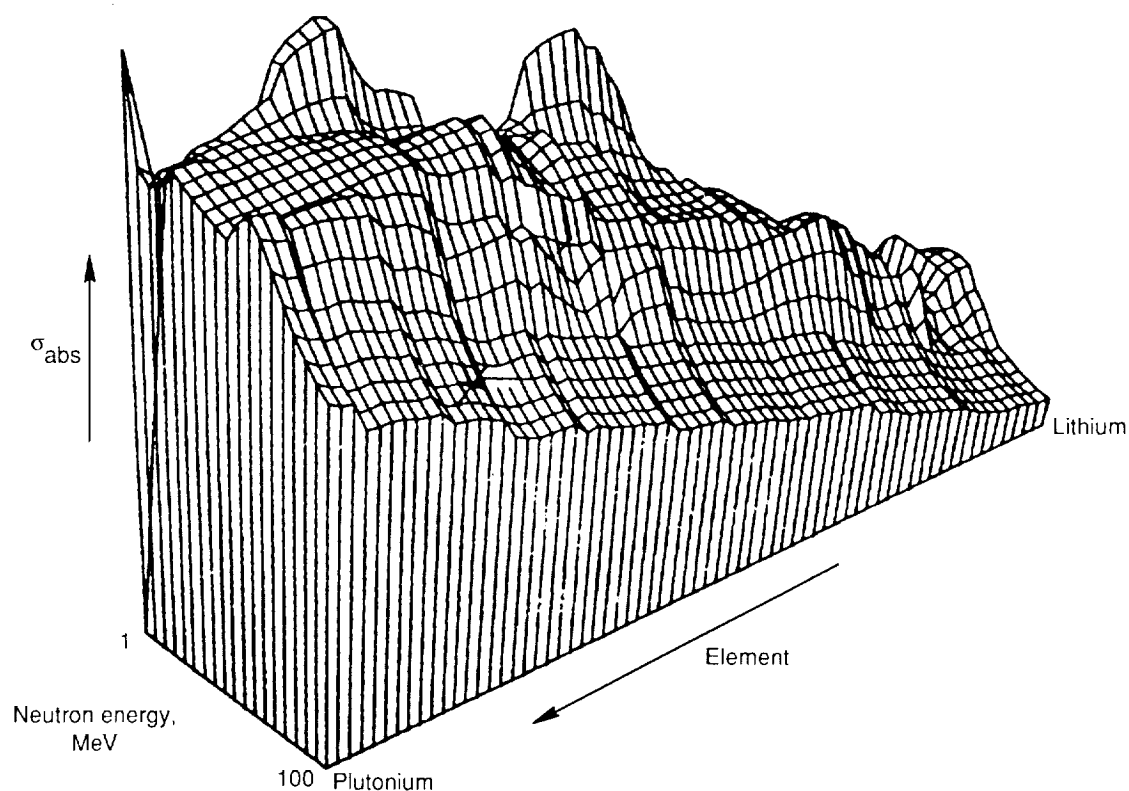
Figure 26. The neutron-nucleus absorption cross section according to the present formalism.
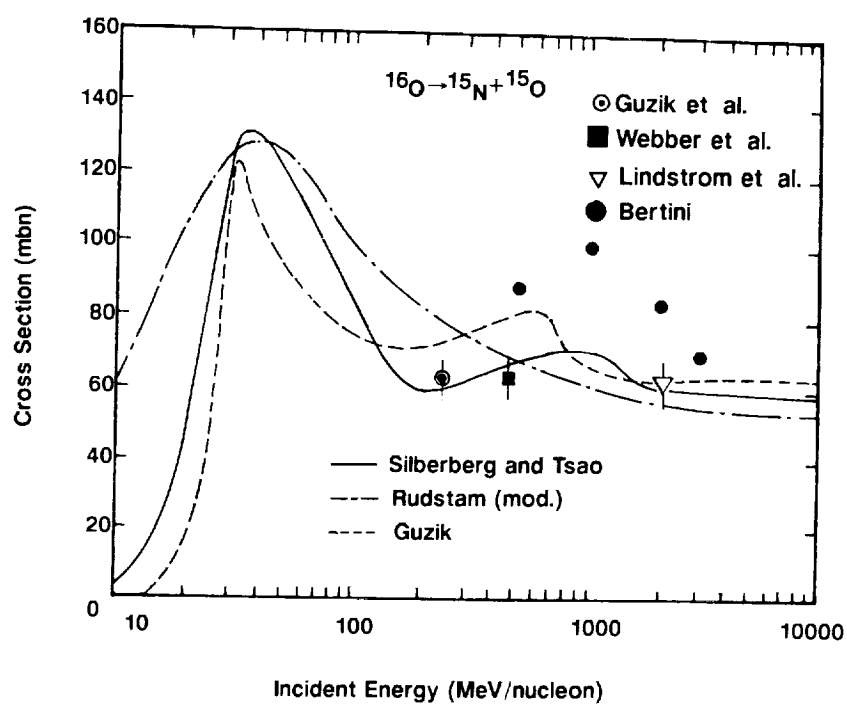
Figure 27. Oxygen fragmentation cross sections for baryon-15 isobars in proton collisions.
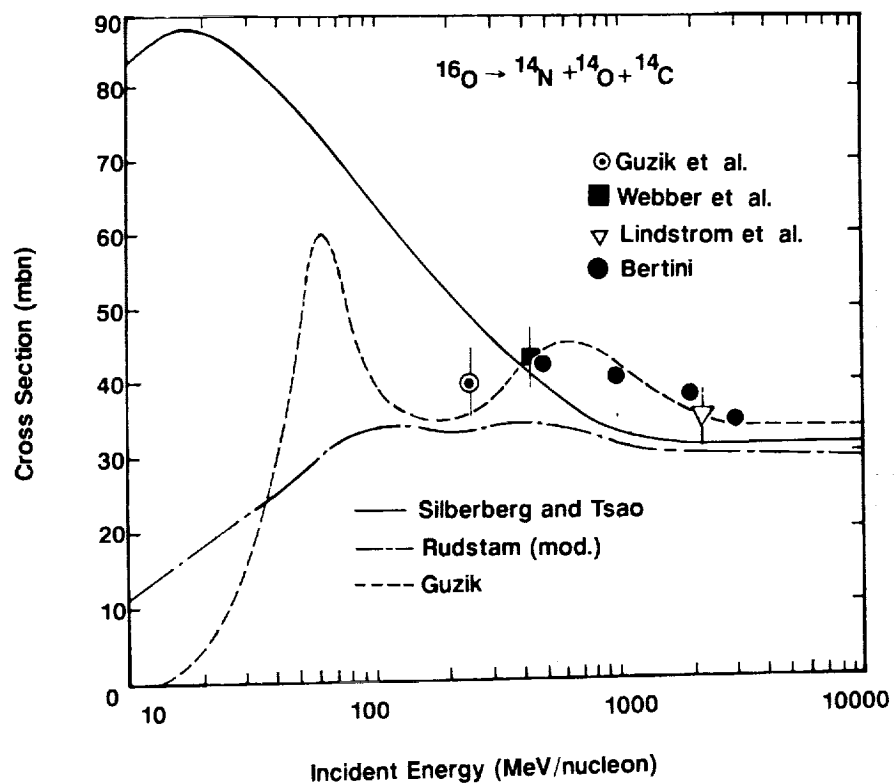
Figure 28. Oxygen fragmentation cross sections for baryon-14 isobars in proton collisions.
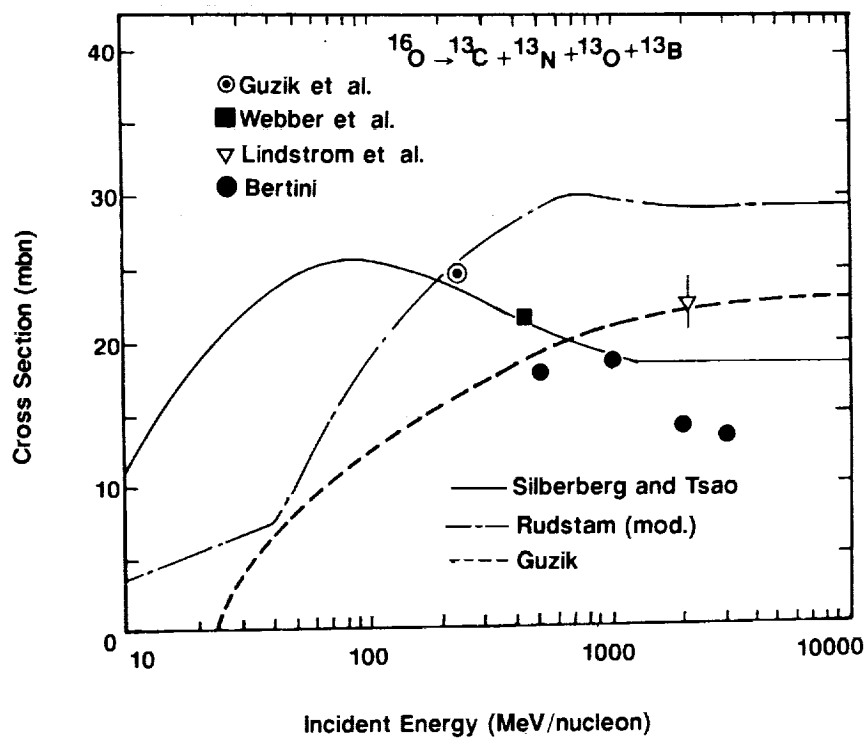
Figure 29. Oxygen fragmentation cross sections for baryon-13 isobars in proton collisions.
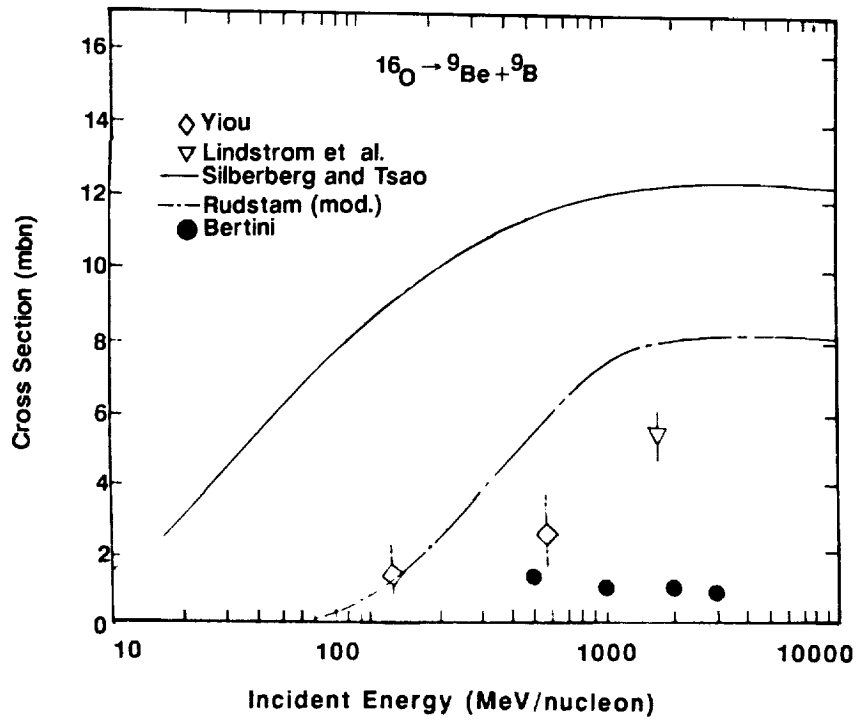
Figure 30. Oxygen fragmentation cross sections for baryon-9 isobars in proton collisions.
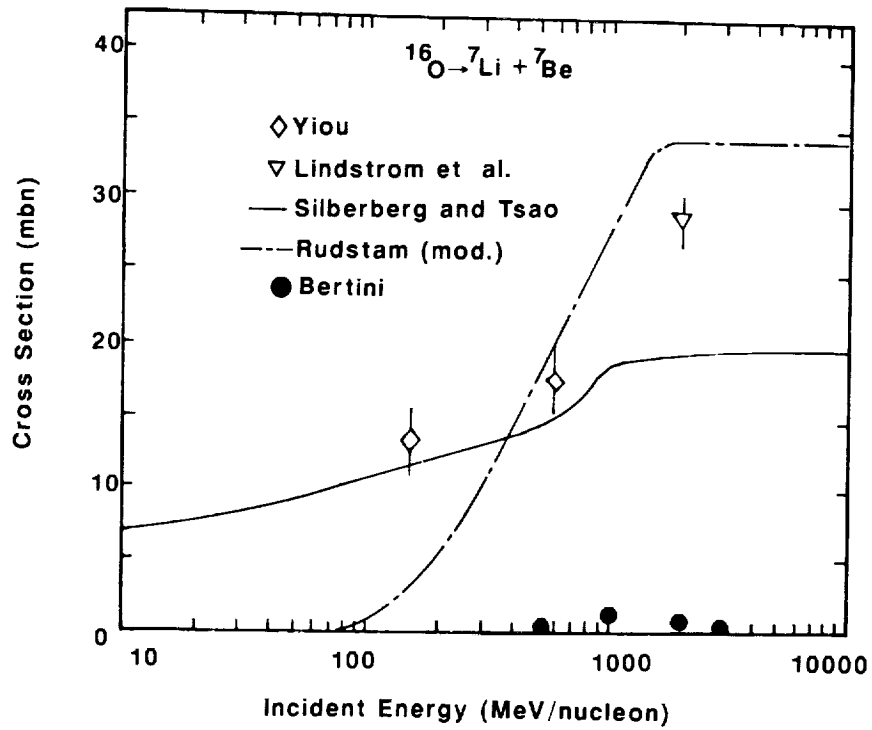
Figure 31. Oxygen fragmentation cross sections for baryon-7 isobars in proton collisions.
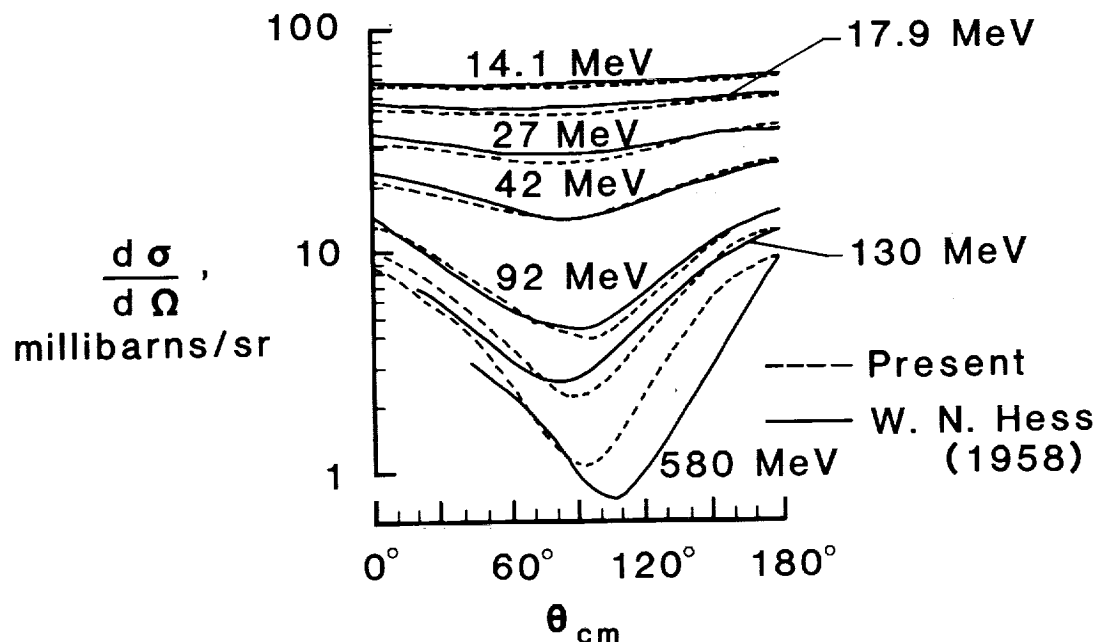
Figure 32. Neutron-proton differential elastic scattering cross section of present model compared with experiment.
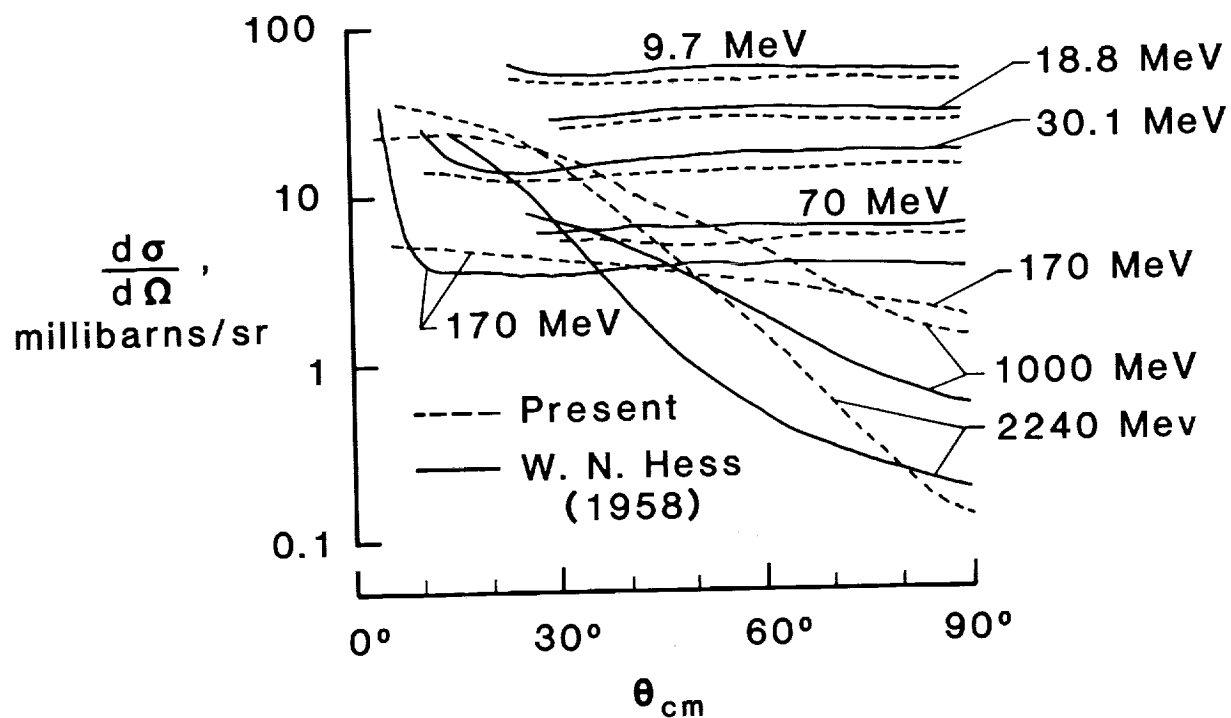
Figure 33. Proton-proton elastic scattering differential cross sections of present model compared with experiment.
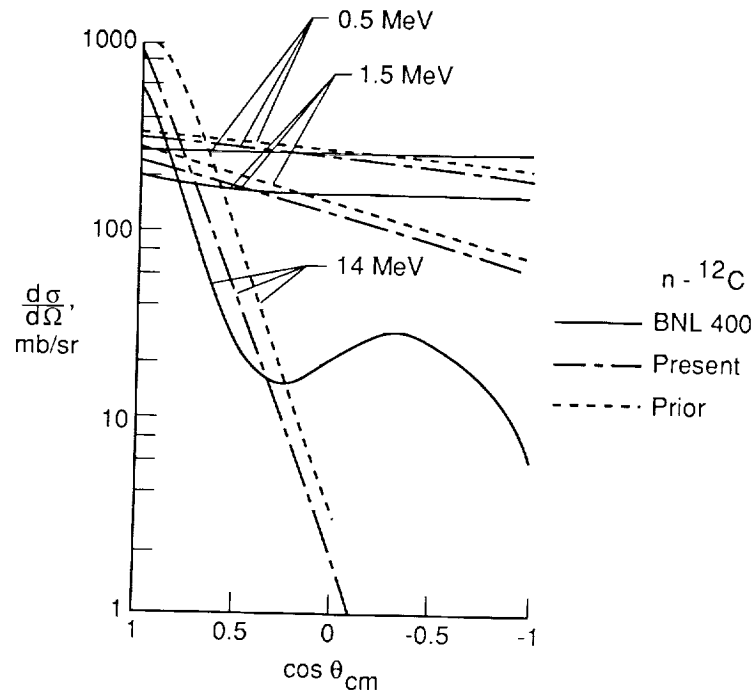
Figure 34. Neutron carbon scattering cross section according to present formalism, prior formalism (ref. 1), and evaluated data (ref. 52).
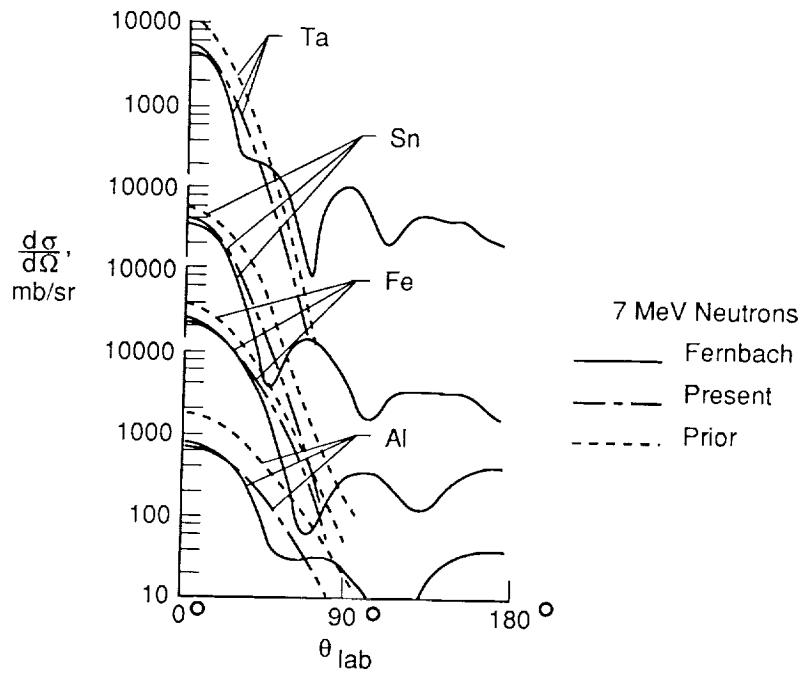
Figure 35. Neutron scattering cross section for several elements according to present formalism, prior formalism (ref. 1), and calculations of Fernbach (ref. 51) for 7 MeV neutrons.
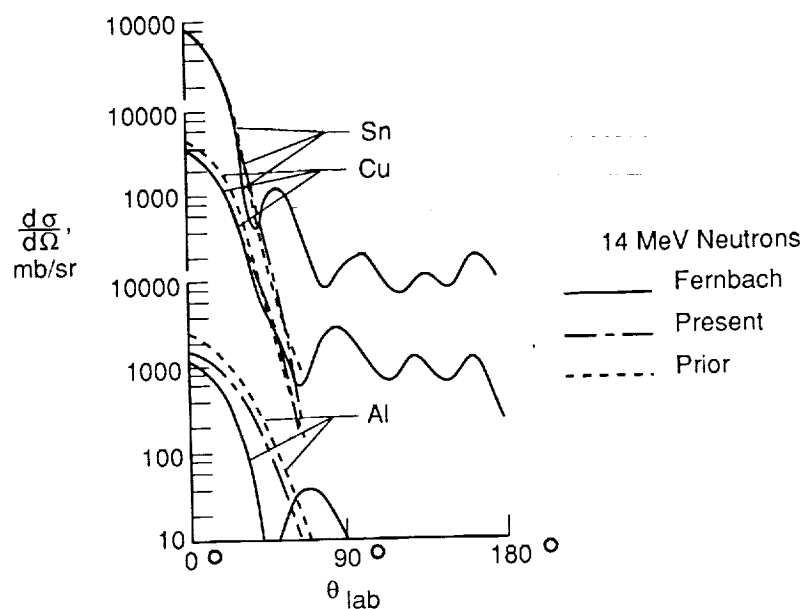
Figure 36. Neutron scattering cross section for several elements according to present formalism, prior formalism (ref. 1), and calculations of Fernbach (ref. 51) for 14 MeV neutrons.
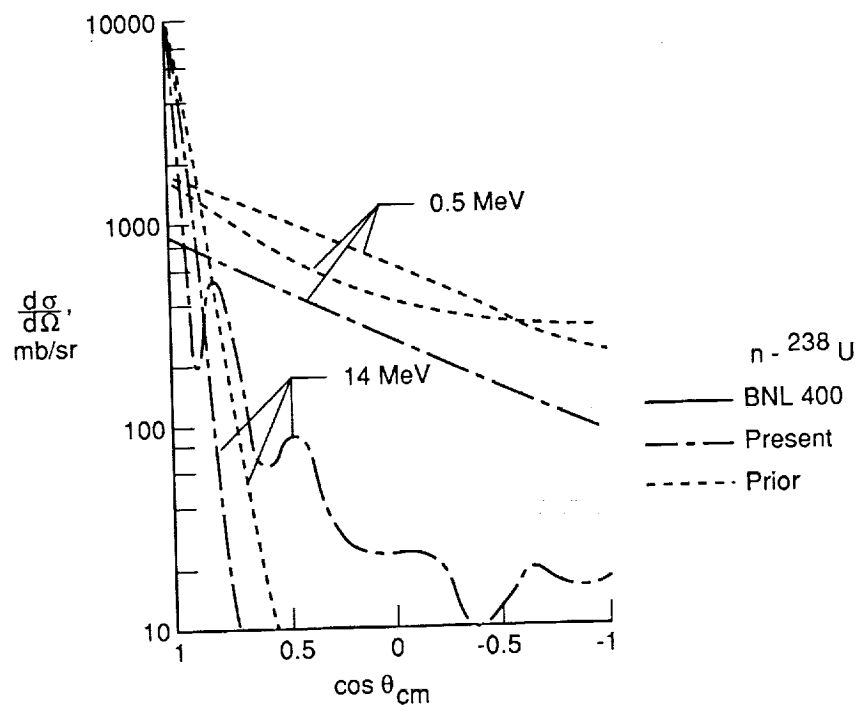
Figure 37. Neutron-uranium scattering cross section according to present formalism, prior formalism (ref. 1), and evaluated data (ref. 52).
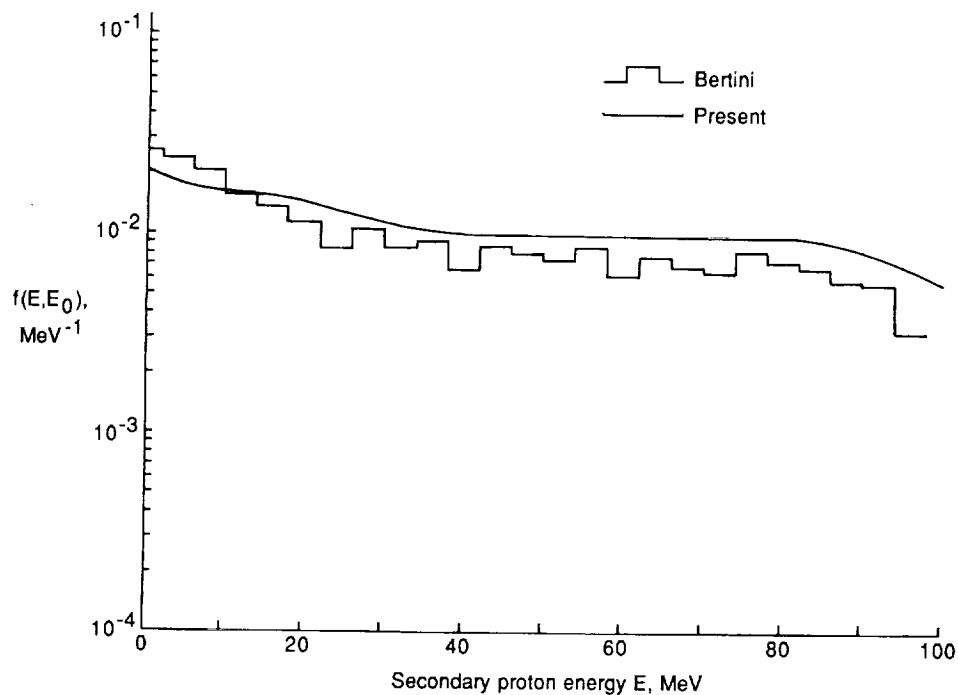
Figure 38. Nucleon cascade spectrum of Bertini compared with cascade spectrum used in present work for protons produced by 100 MeV protons on oxygen.
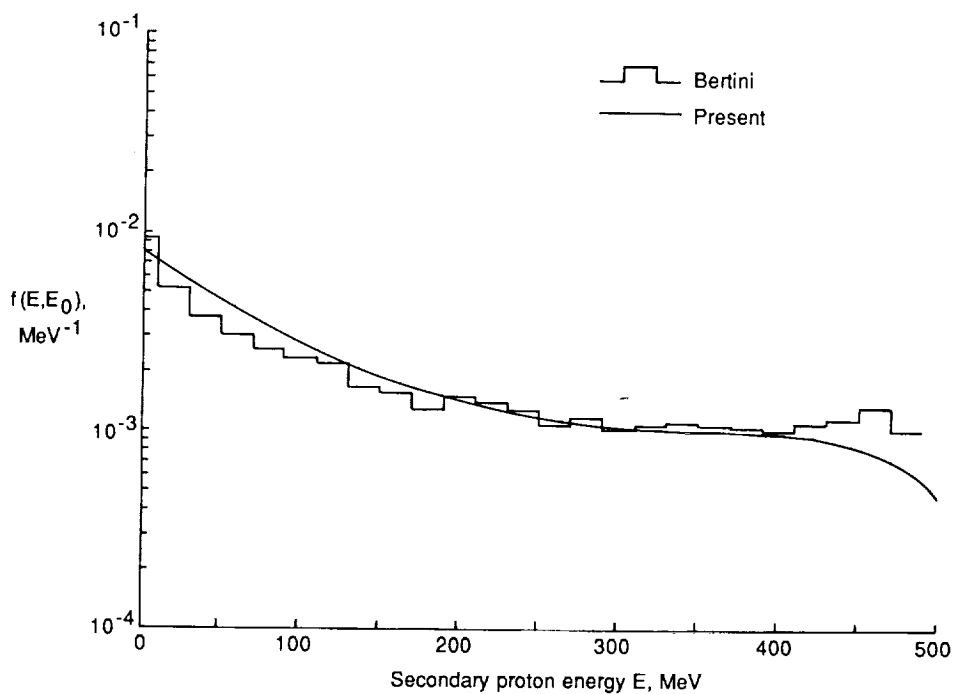
Figure 39. Nucleon cascade spectrum of Bertini compared with cascade spectrum used in present work for protons produced by 500 MeV protons on oxygen.
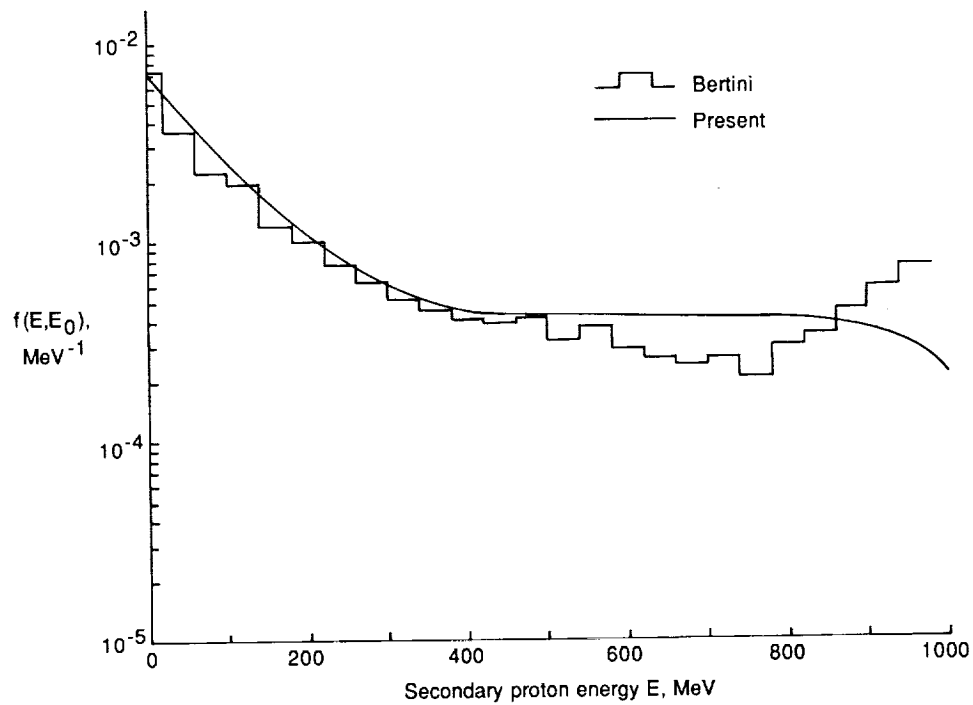
Figure 40. Nucleon cascade spectrum of Bertini compared with cascade spectrum used in present work for protons produced by 1000 MeV protons on oxygen.
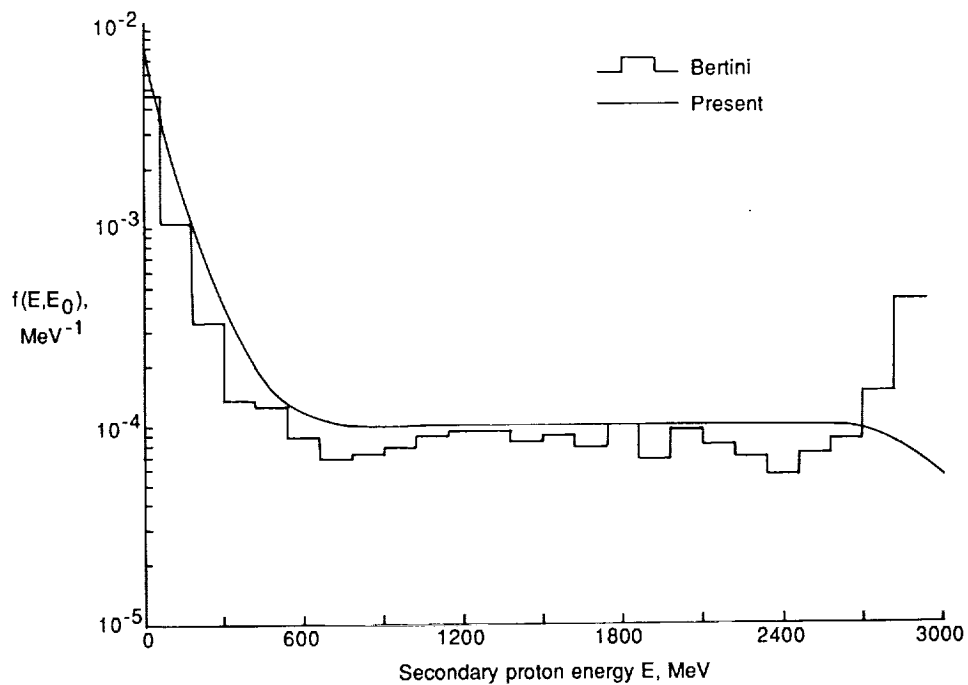
Figure 41. Nucleon cascade spectrum of Bertini compared with cascade spectrum used in present work for protons produced by 3000 MeV protons on oxygen.
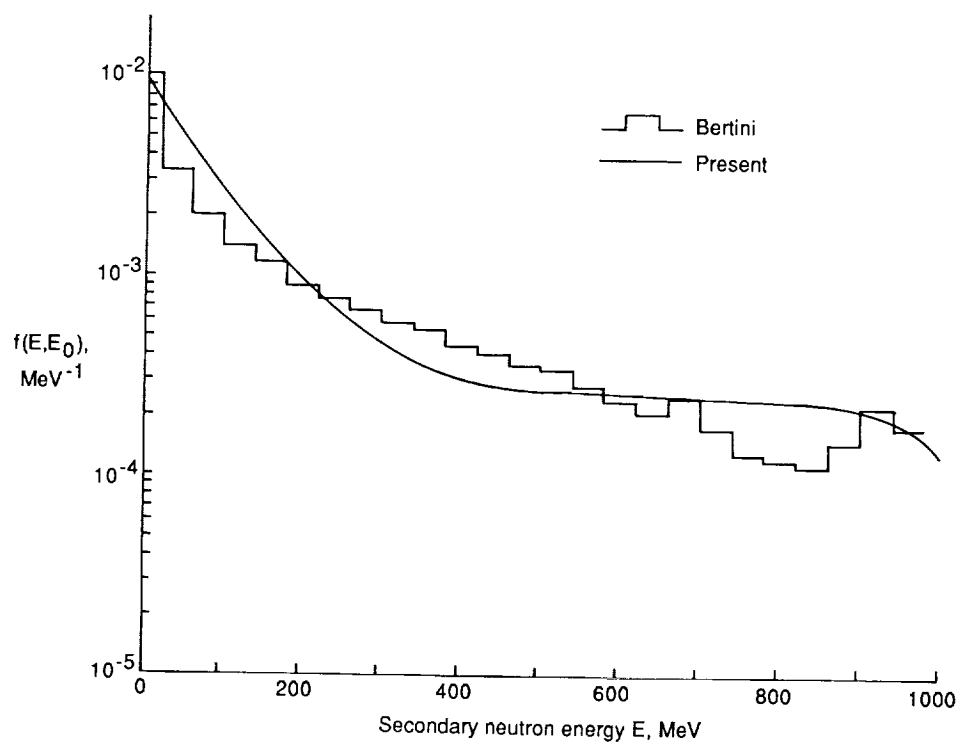
Figure 42. Nucleon cascade spectrum of Bertini compared with present work for neutrons produced by 1000 MeV protons on oxygen.
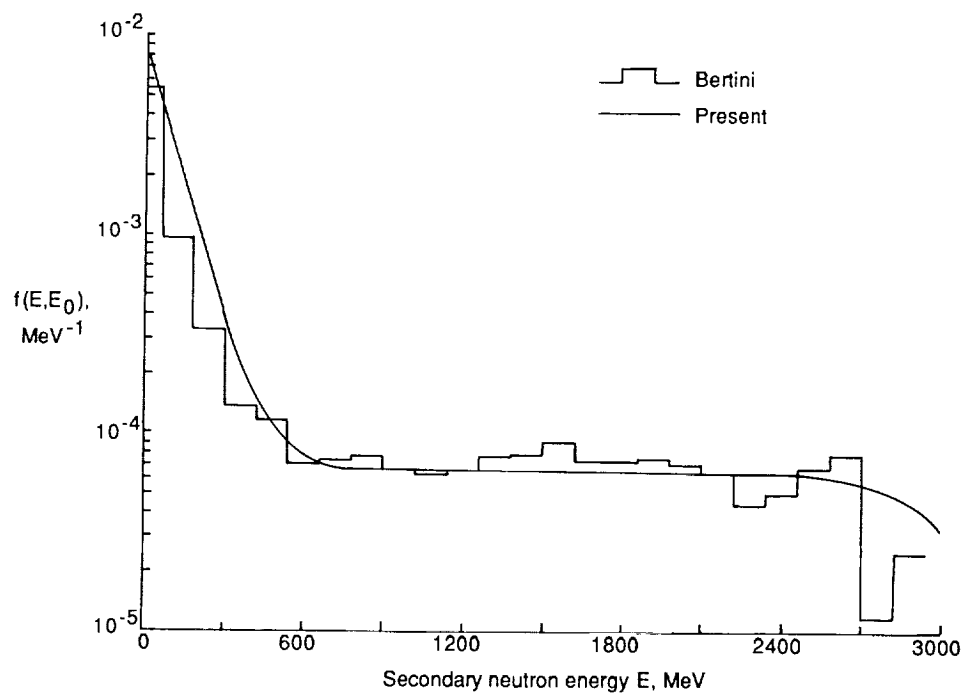
Figure 43. Nucleon cascade spectrum of Bertini compared with present work for neutrons produced by 3000 MeV protons on oxygen.
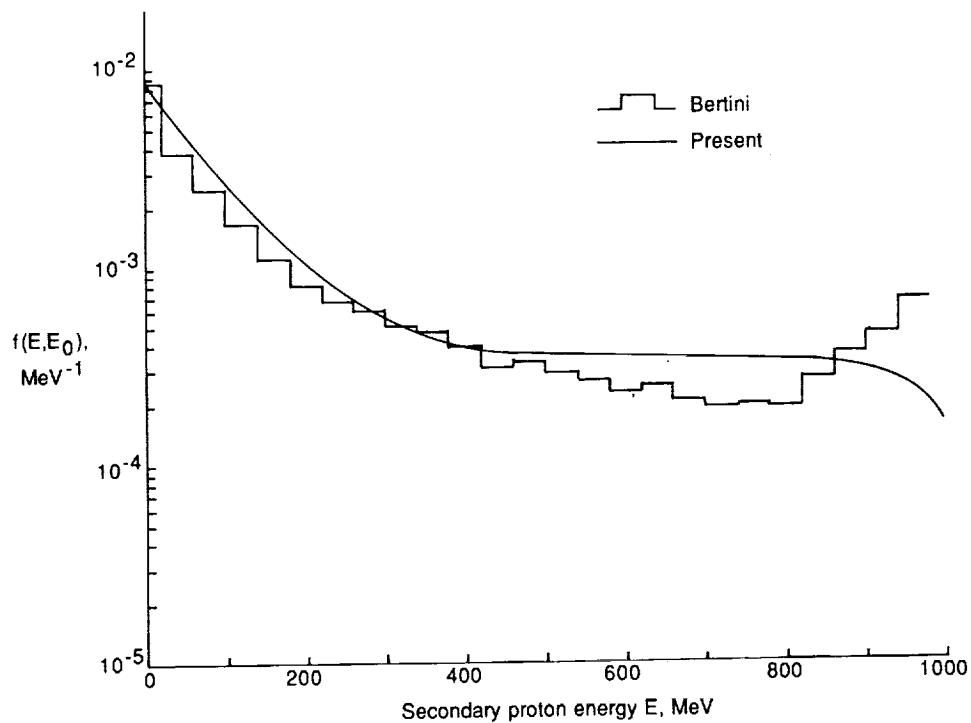
Figure 44. Nucleon cascade spectrum of Bertini compared with cascade spectrum used in present work for protons produced by 1000 MeV protons on aluminum.
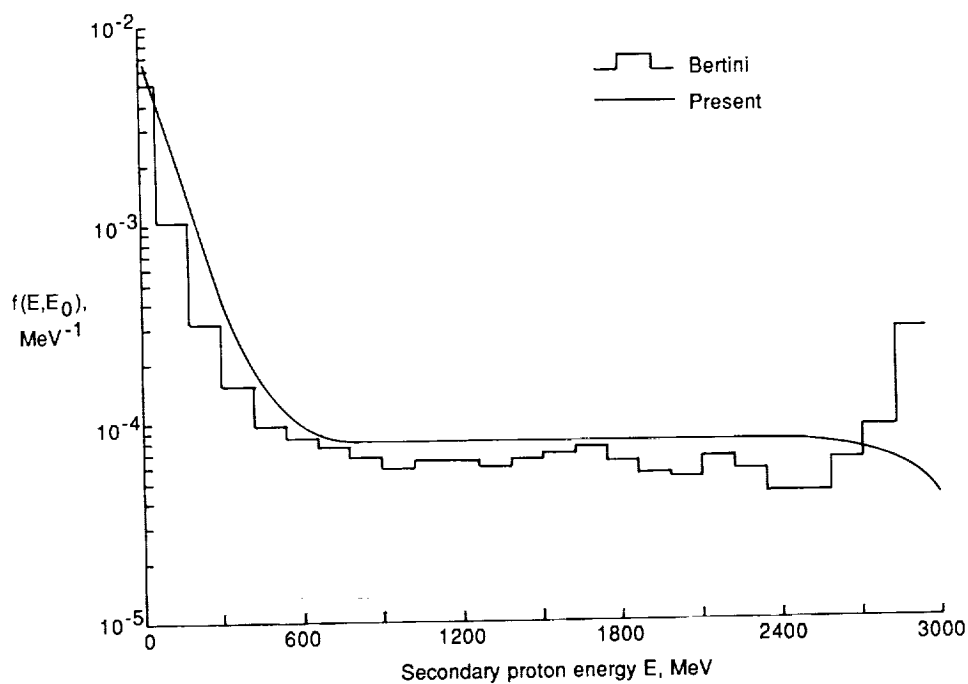
Figure 45. Nucleon cascade spectrum of Bertini compared with cascade spectrum used in present work for protons produced by 3000 MeV protons on aluminum.
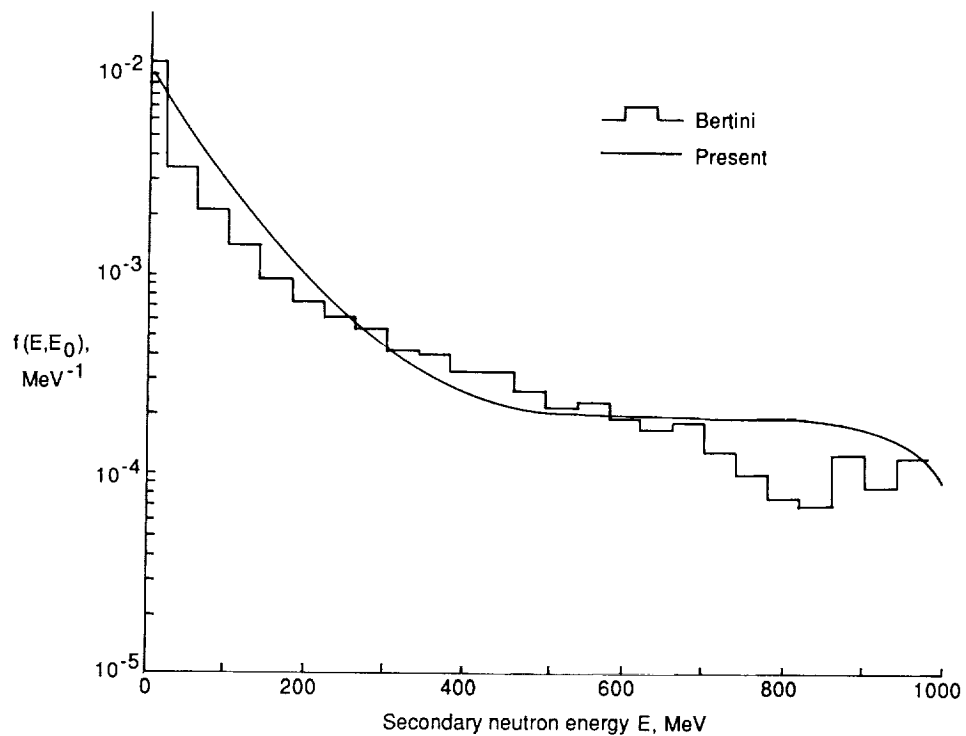
Figure 46. Nucleon cascade spectrum of Bertini compared with present work for neutrons produced by 1000 MeV protons on aluminum.
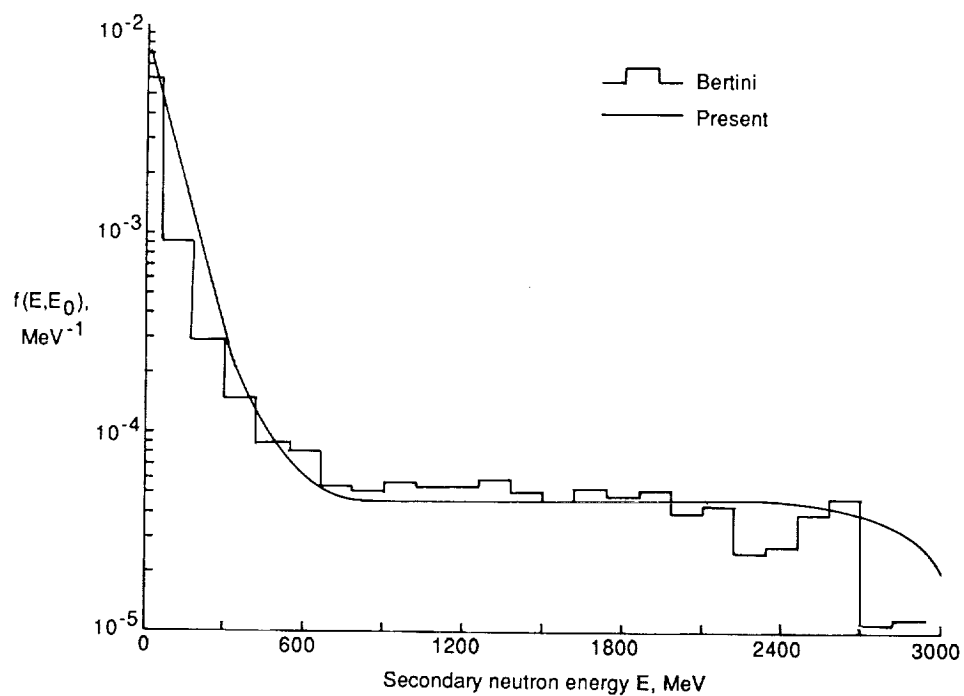
Figure 47. Nucleon cascade spectrum of Bertini compared with present work for neutrons produced by 3000 MeV protons on aluminum.
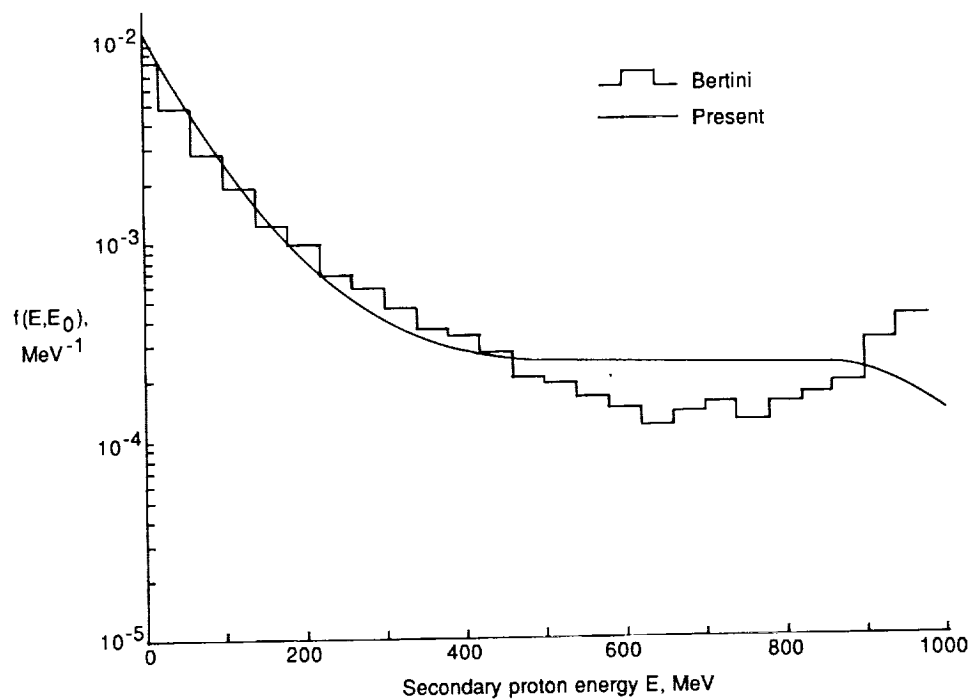
Figure 48. Nucleon cascade spectrum of Bertini compared with cascade spectrum used in present work for protons produced by 1000 MeV protons on lead.
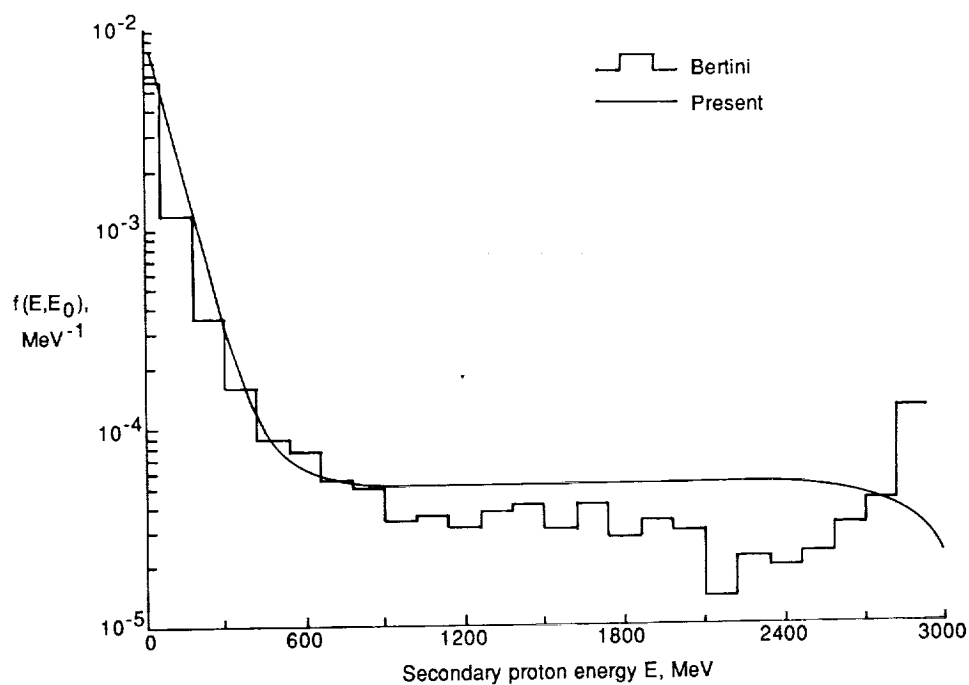
Figure 49. Nucleon cascade spectrum of Bertini compared with cascade spectrum used in present work for protons produced by 3000 MeV protons on lead.
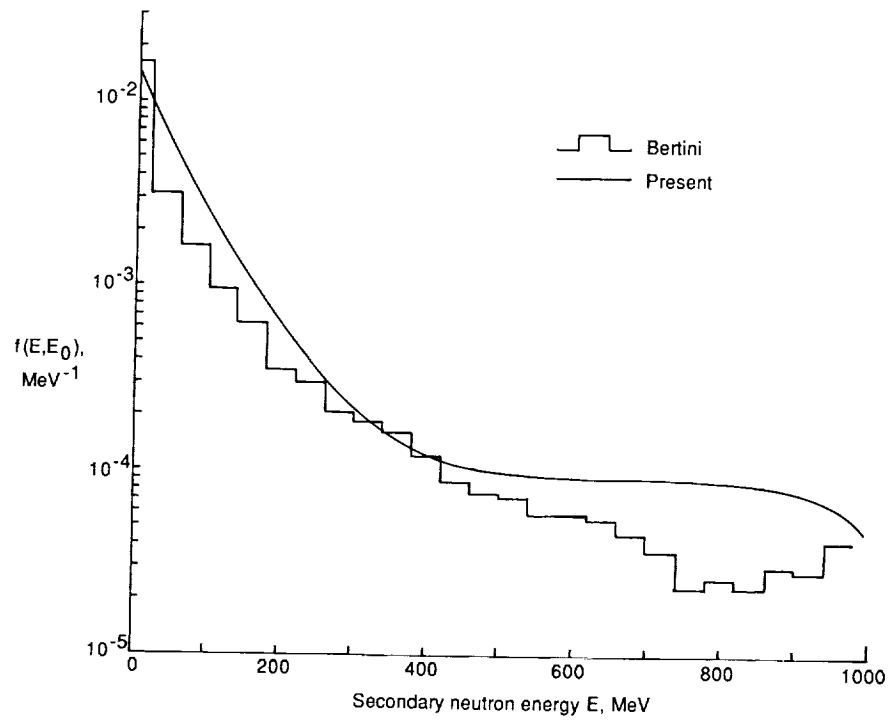
Figure 50. Nucleon cascade spectrum of Bertini compared with present work for neutrons produced by 1000 MeV protons on lead.
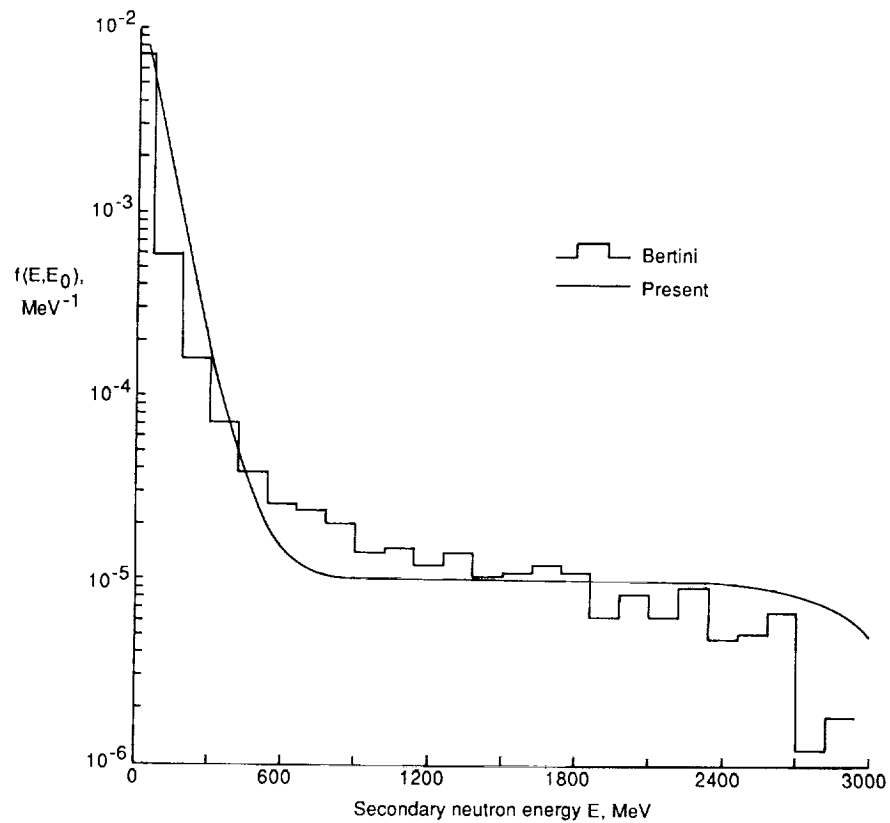
Figure 51. Nucleon cascade spectrum of Bertini compared with present work for neutrons produced by 3000 MeV protons on lead.
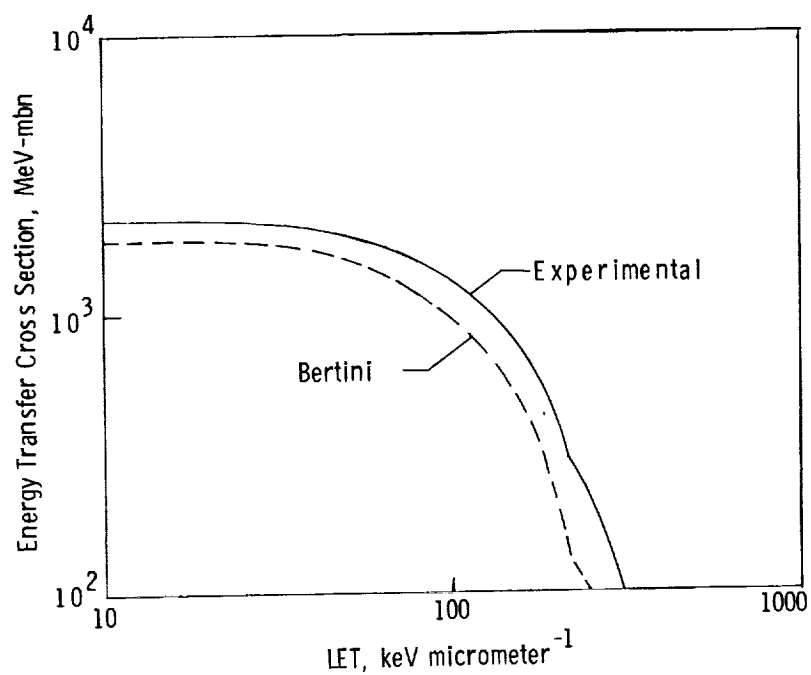
Figure 52. Linear energy transfer (LET) cross section for fragmenting oxygen nucleus in water.
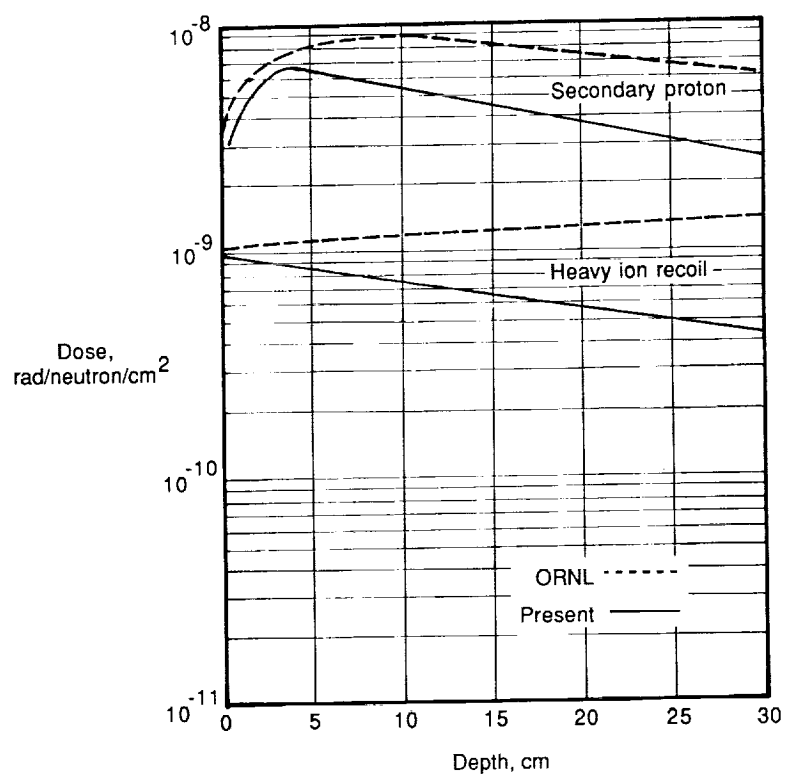
Figure 53. Dose in tissue to normal incident 60 MeV neutrons.
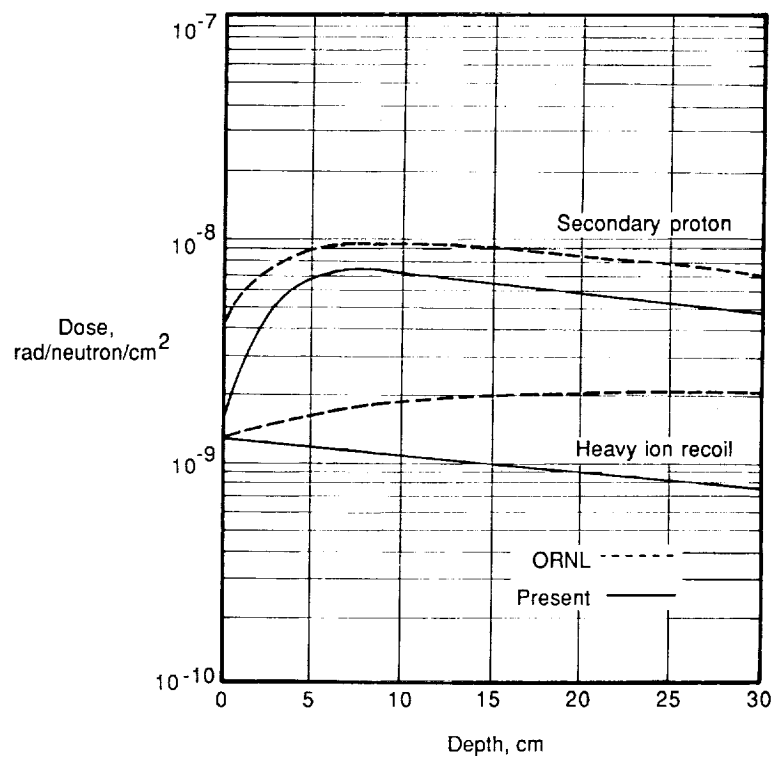
Figure 54. Dose in tissue to normal incident 100 MeV neutrons.
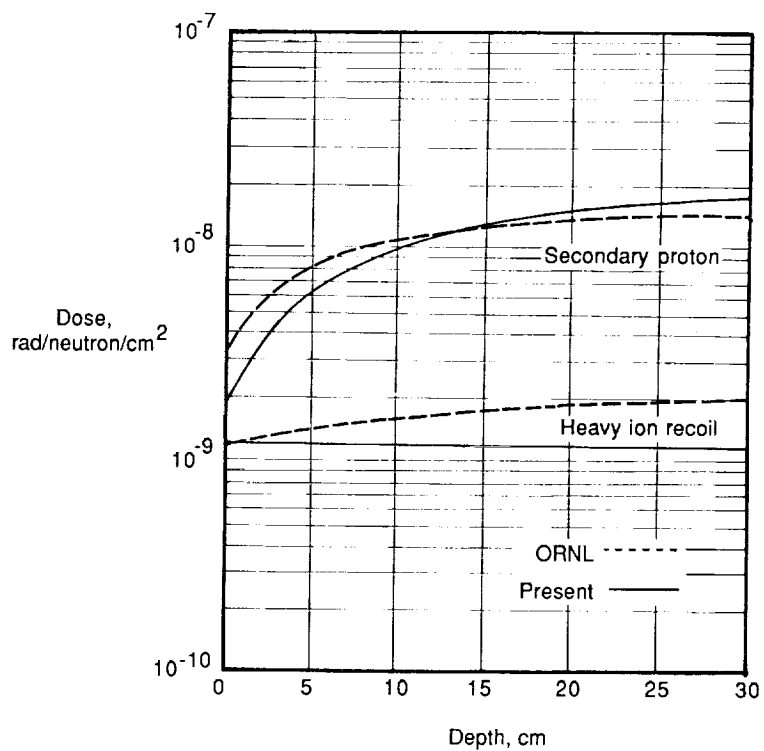
Figure 55. Dose in tissue to normal incident 200 MeV neutrons.
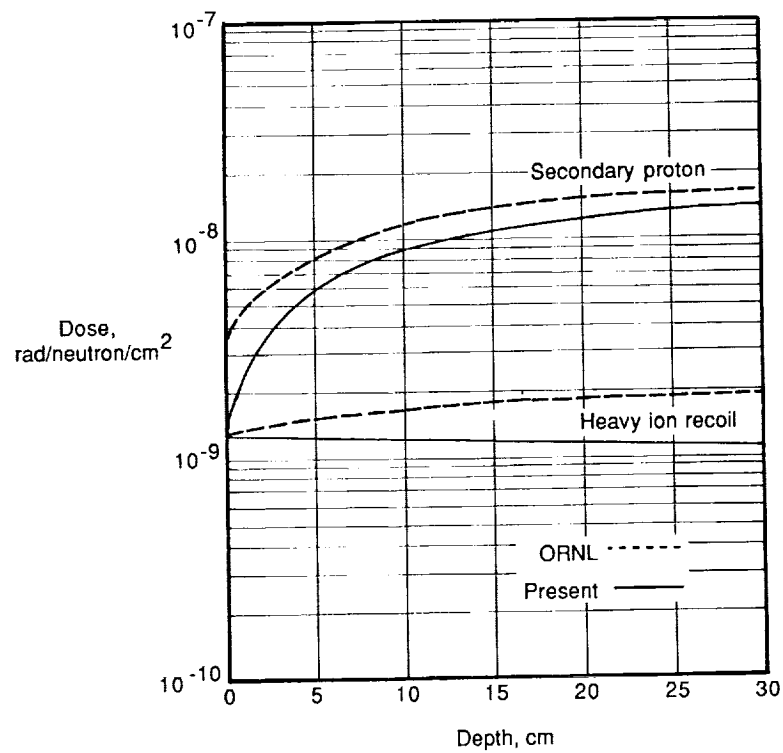
Figure 56. Dose in tissue to normal incident 300 MeV neutrons.
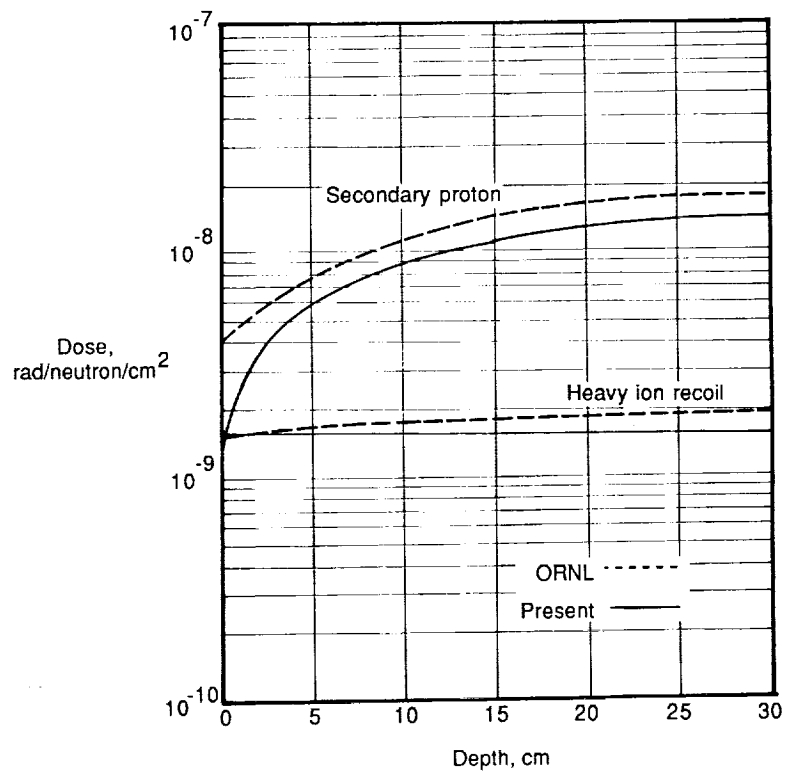
Figure 57. Dose in tissue to normal incident 400 MeV neutrons.

72
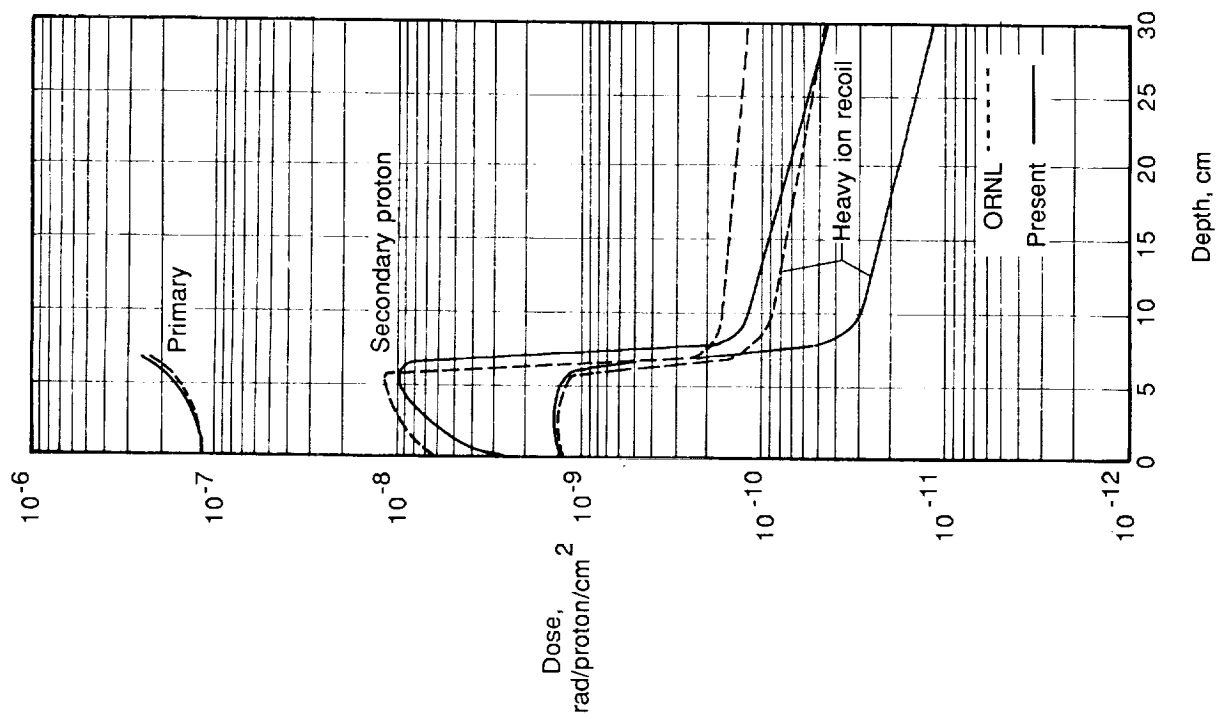
Figure 58. Dose in tissue to normal incident 100 MeV protons.
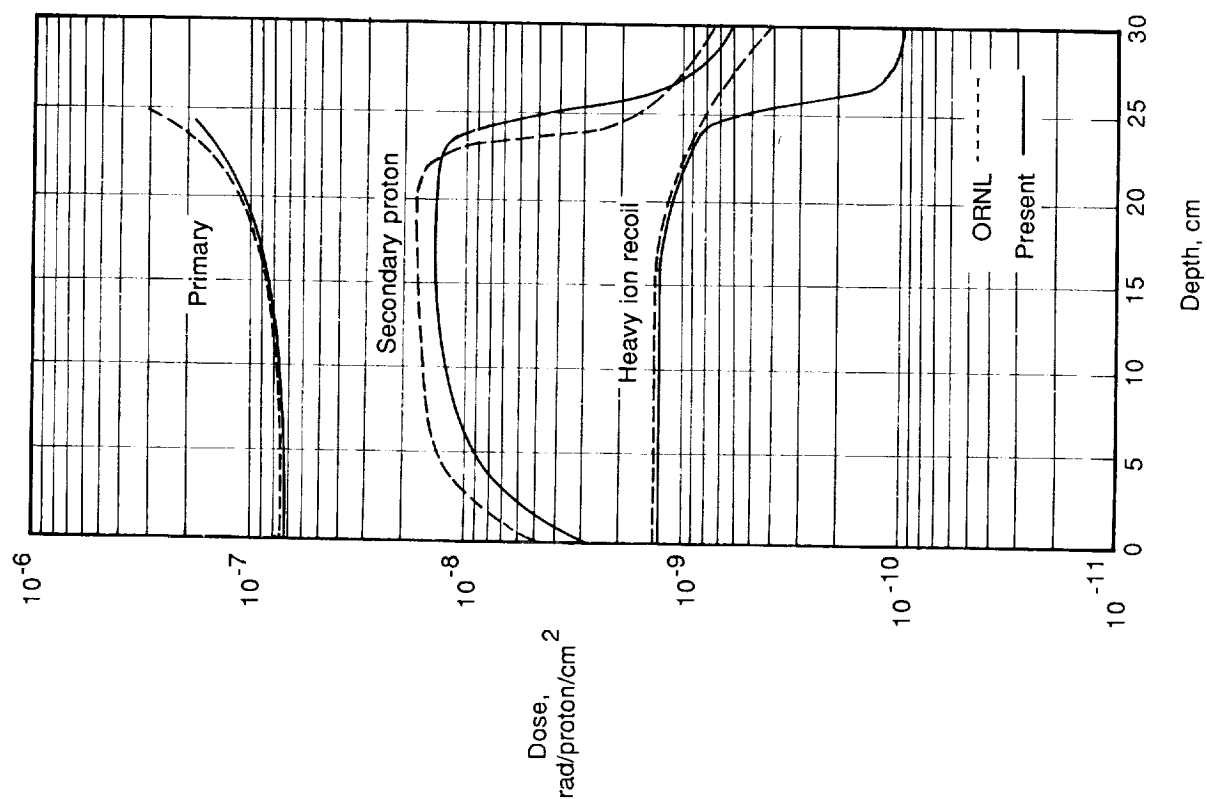
Figure 59. Dose in tissue to normal incident 200 MeV protons.

73
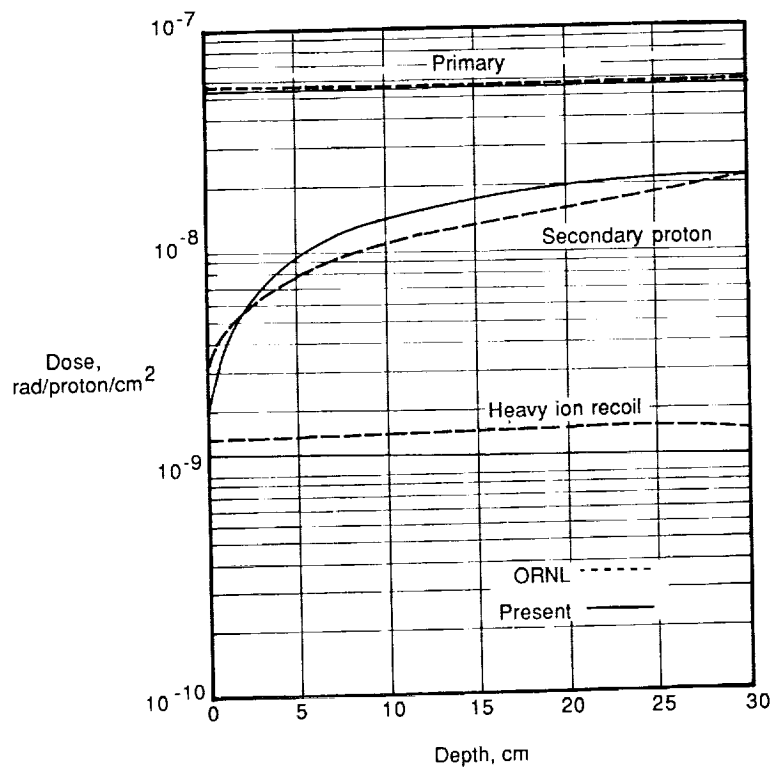
Figure 60. Dose in tissue to normal incident 300 MeV protons.
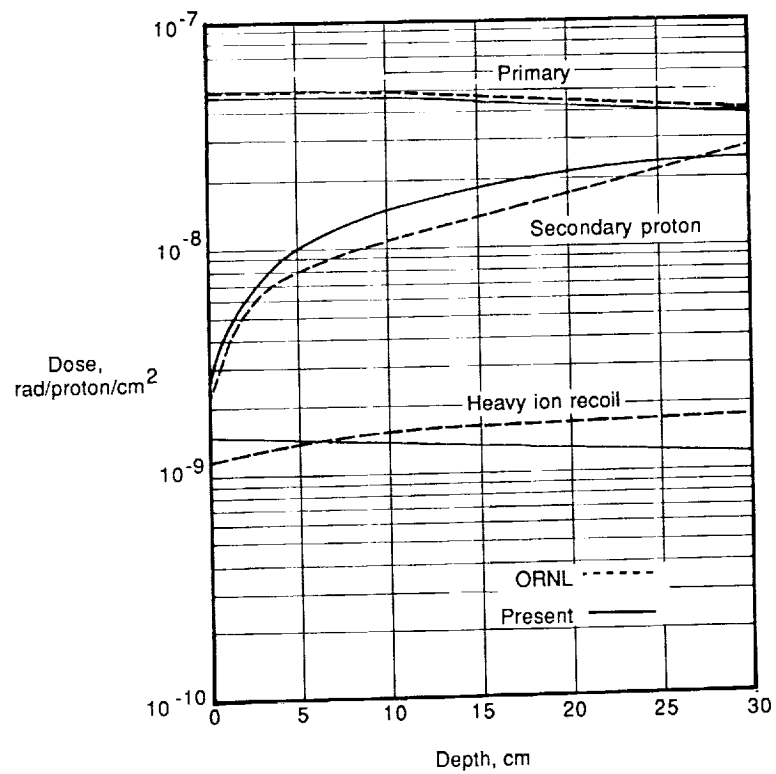
Figure 61. Dose in tissue to normal incident 400 MeV protons.
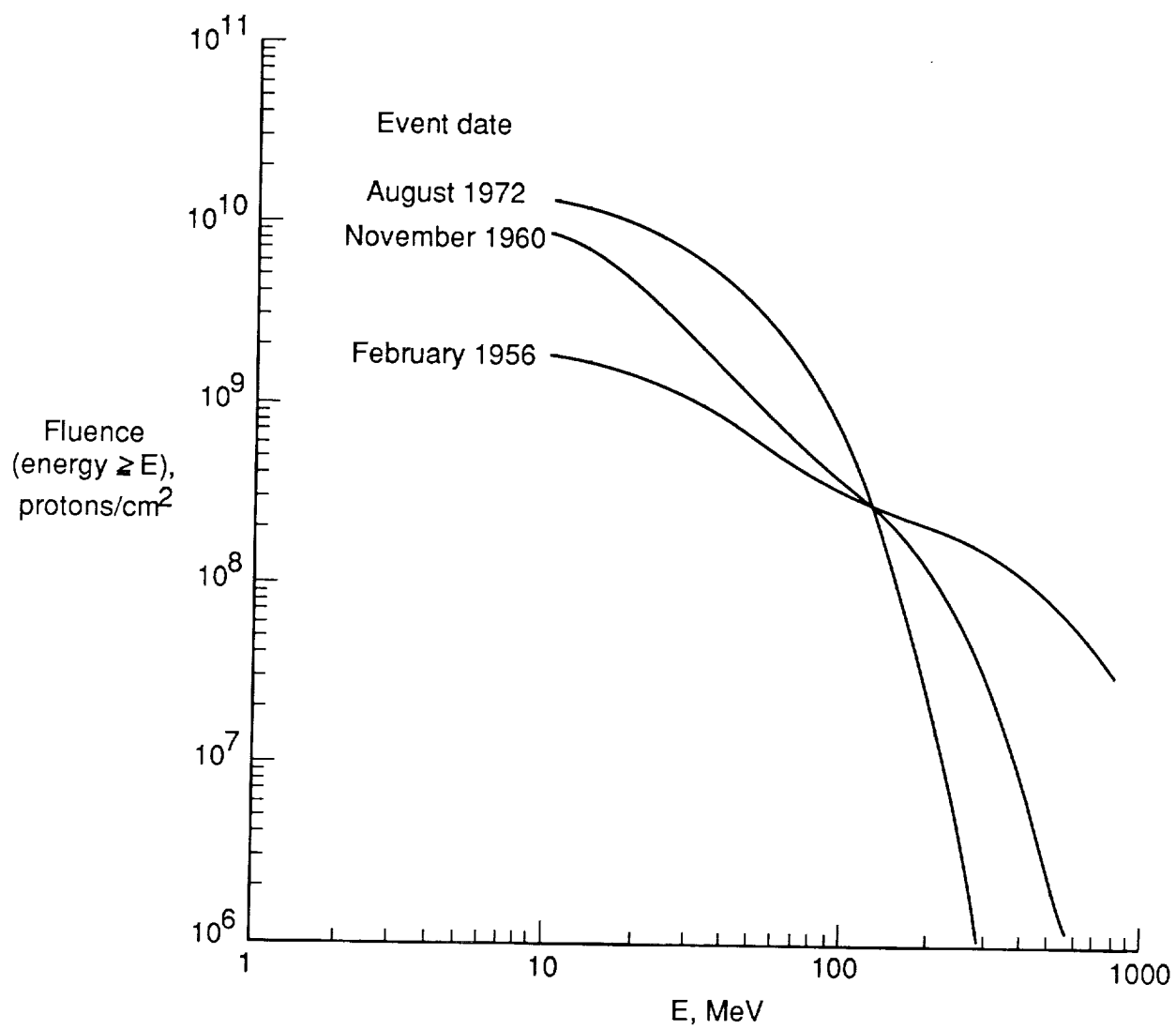
Figure 62. Time-integrated proton flux spectra for three anomalously large solar proton events.
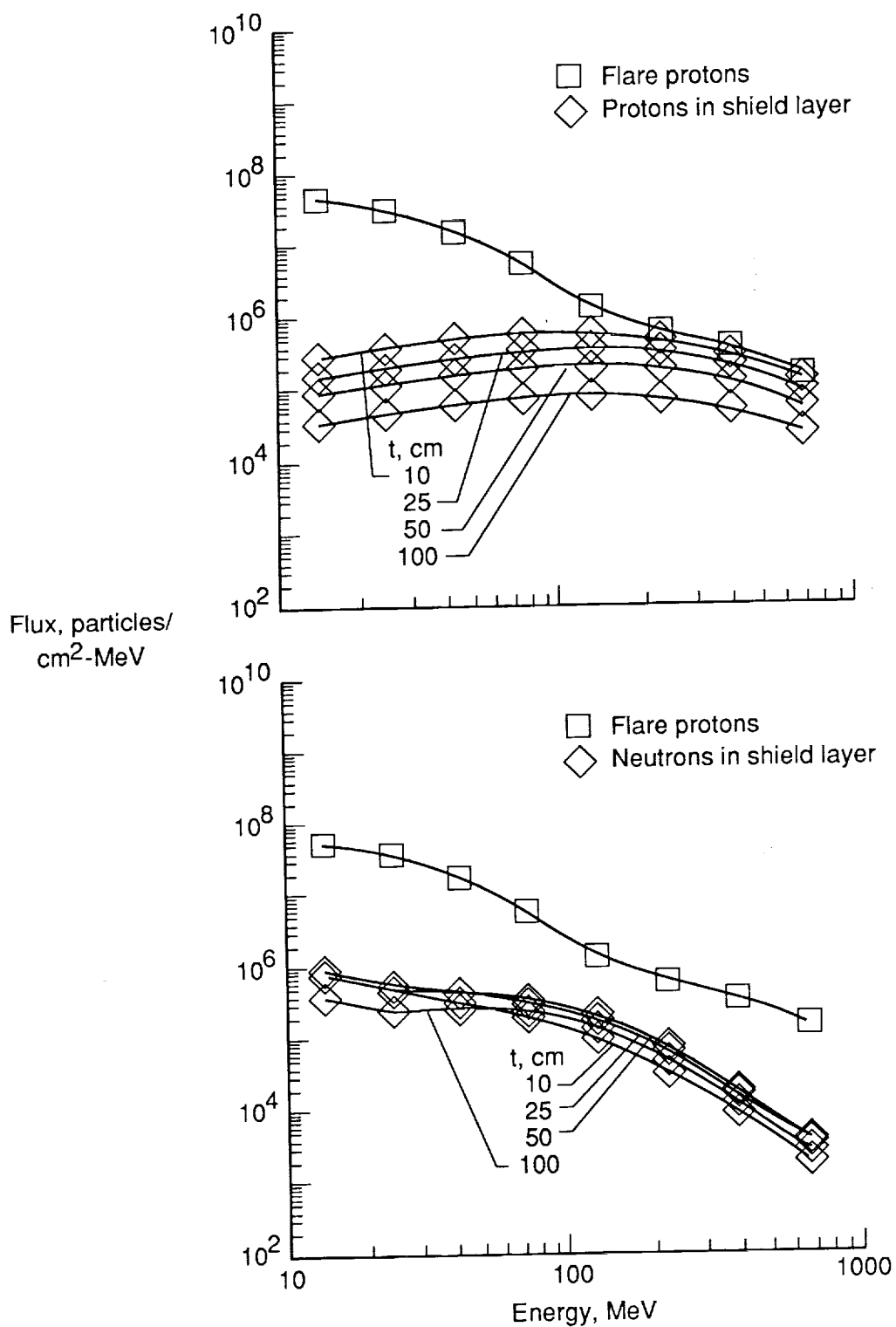
Figure 63. Nucleon flux variation with energy for indicated t-values of regolith thickness for proton event of February 1956 (denoted by flare protons □).
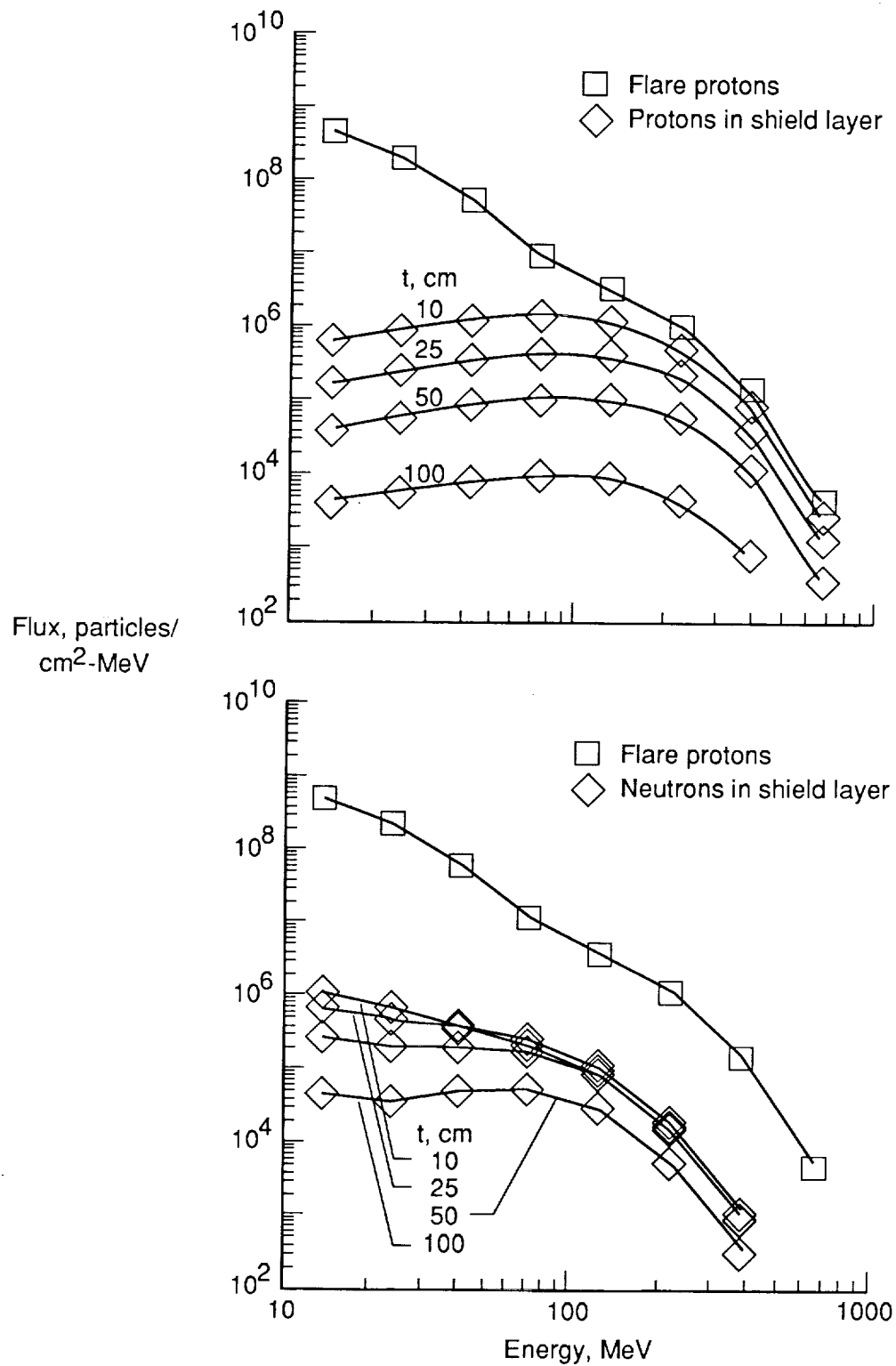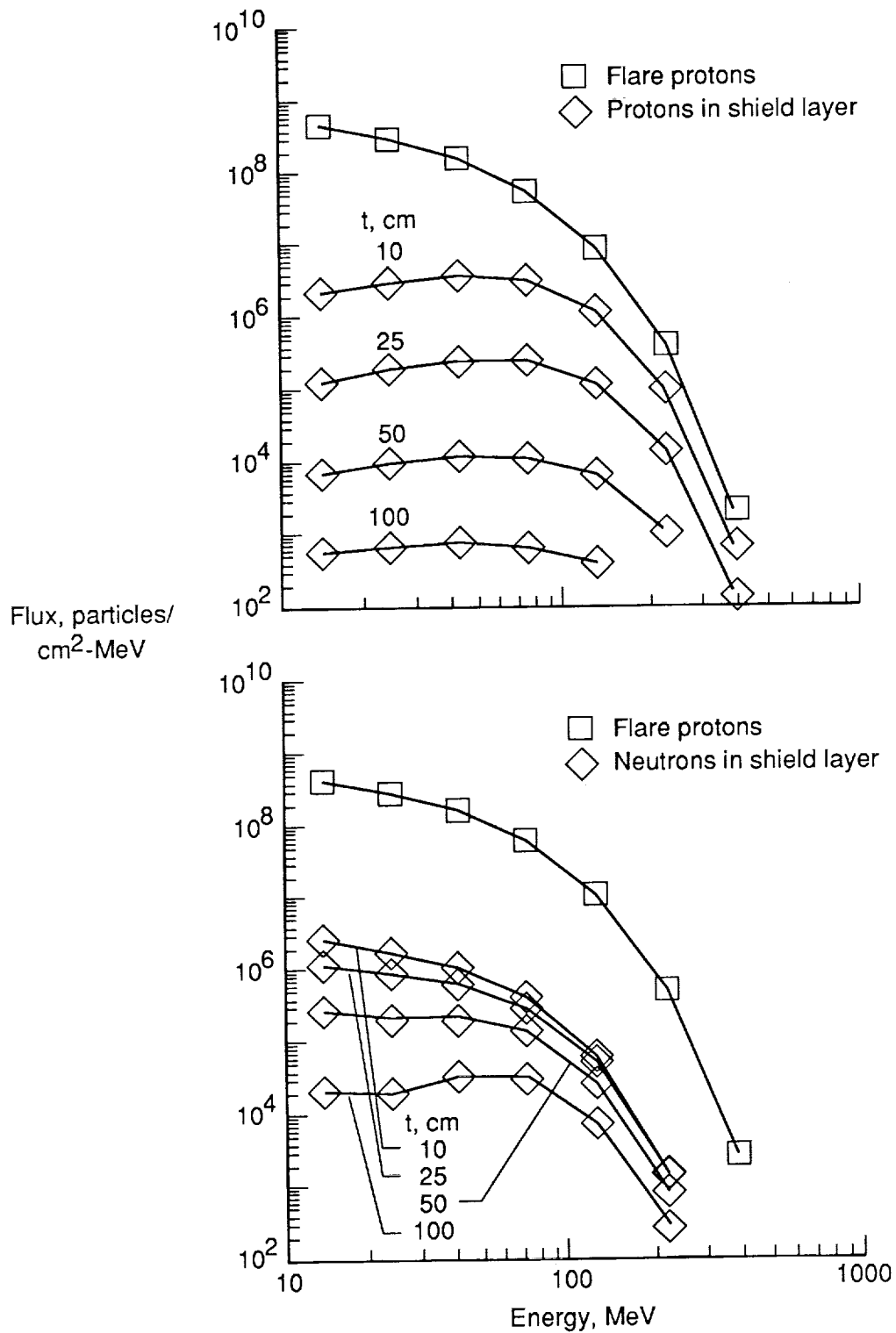
Figure 64. Nucleon flux variation with energy for indicated t-values of regolith thickness for proton event of November 1960 (denoted by flare protons □).

Figure 65. Nucleon flux variation with energy for indicated t-values of regolith thickness for proton event of August 1972 (denoted by flare protons □).
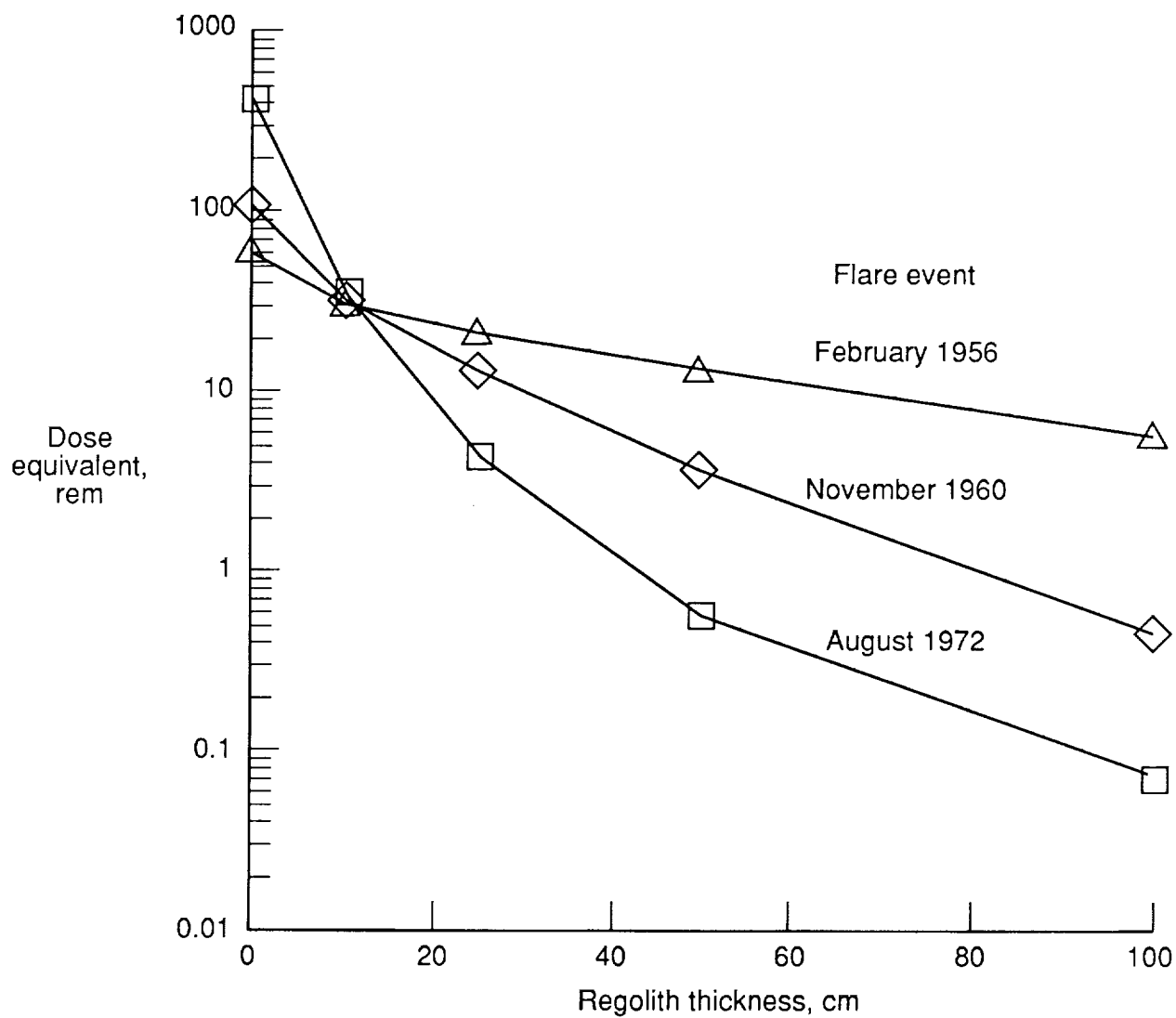
78

Figure 66. Predicted 5-cm tissue dose equivalents for slab thicknesses between 0 and 100 cm in simulated lunar regolith.
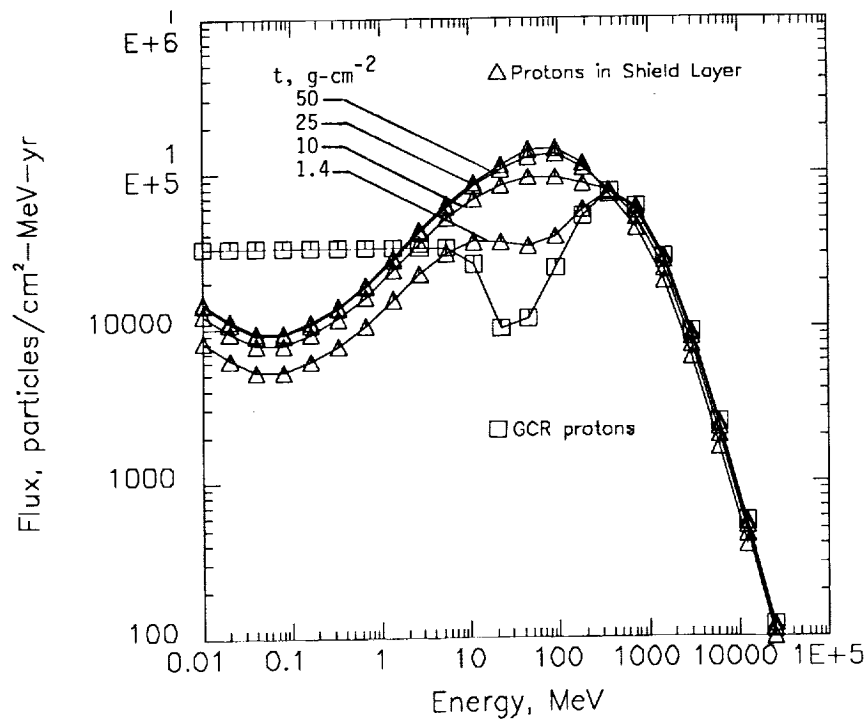
Figure 67. Galactic cosmic ray (GCR) proton flux variation with energy due to incident GCR protons for indicated t-values of depth in aluminum.
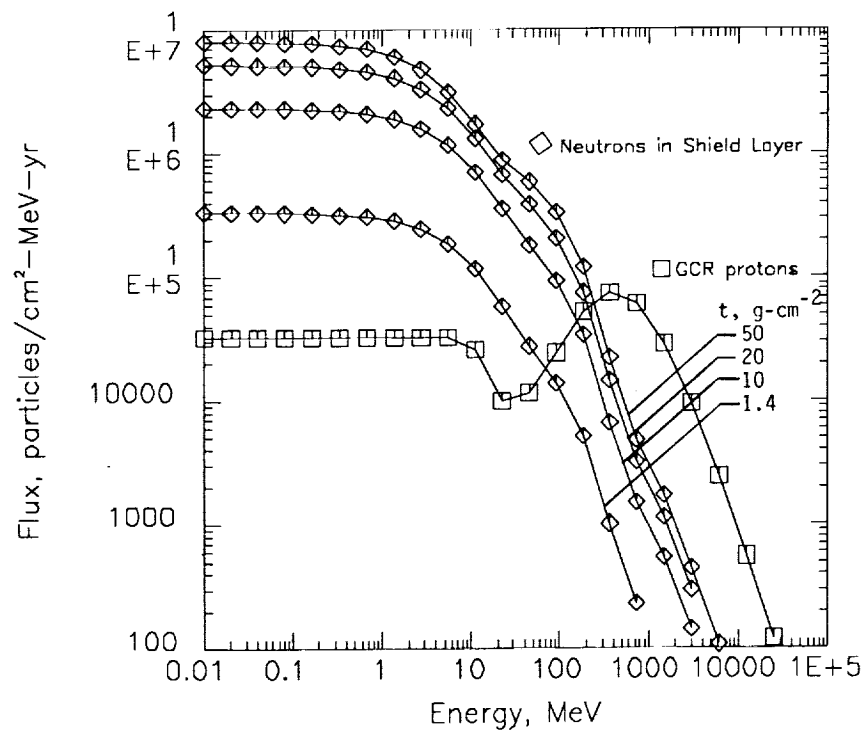

Figure 68. Neutron flux variation with energy due to incident GCR protons for incident t-values of depth in aluminum.
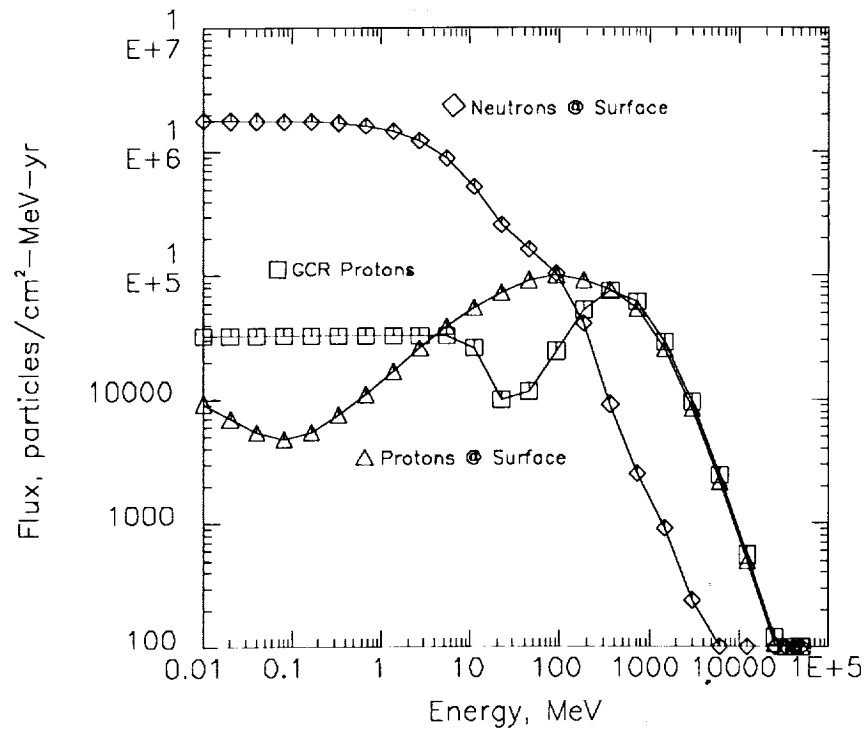
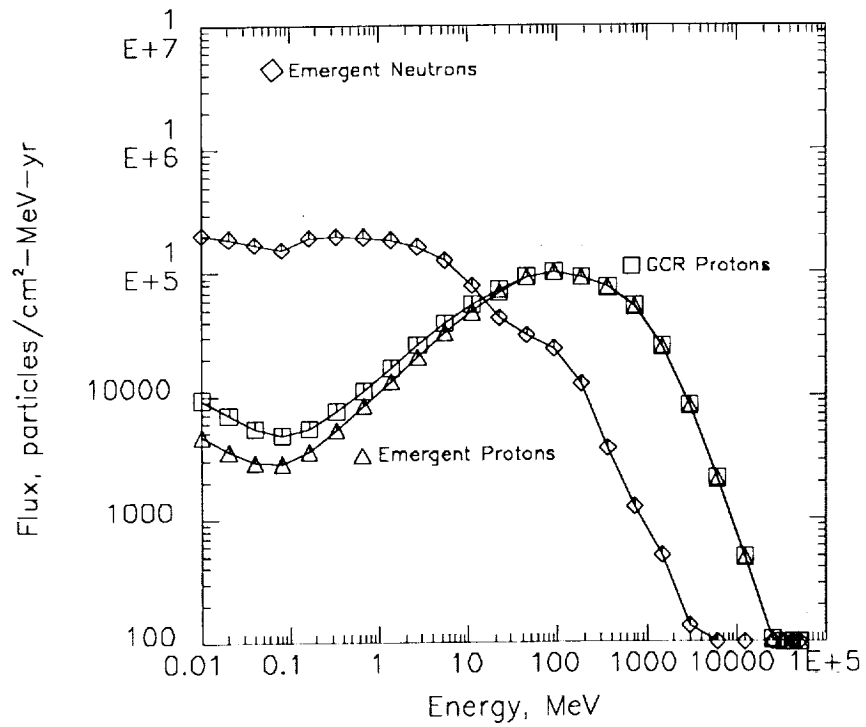Figure 69. Nucleon vertical flux at martian surface due to incident GCR protons.

Figure 70. Attenuated surface neutron flux using a 2-g/cm² polyethylene shield.

NASA
National Aeronautics and
Space Administration

Report Documentation Page

1. Report No. NASA TP-2887	2. Government Accession No.	3. Recipient's Catalog No.
4. Title and Subtitle BRYNTRN: A Baryon Transport Model		5. Report Date March 1989
		6. Performing Organization Code
7. Author(s) John W. Wilson, Lawrence W. Townsend, John E. Nealy, Sang Y. Chun, B. S. Hong, Warren W. Buck, L. S. Lamkin, Barry D. Ganapol, Ferdous Khan, and Francis A. Cucinotta		8. Performing Organization Report No. L-16512
9. Performing Organization Name and Address NASA Langley Research Center Hampton, VA 23665-5225		10. Work Unit No. 199-22-76-01
		11. Contract or Grant No.
12. Sponsoring Agency Name and Address National Aeronautics and Space Administration Washington, DC 20546-0001		13. Type of Report and Period Covered Technical Paper
		14. Sponsoring Agency Code

15. Supplementary Notes

John W. Wilson, Lawrence W. Townsend, and John E. Nealy: Langley Research Center,
Hampton, Virginia.
Sang Y. Chun, B. S. Hong, and Warren W. Buck: Hampton University, Hampton, Virginia.
S. L. Lamkin: PRC Kentron, Inc., Aerospace Technologies Division, Hampton, Virginia.
Barry D. Ganapol: University of Arizona, Tucson, Arizona.
Ferdous Khan and Francis A. Cucinotta: Old Dominion University, Norfolk, Virginia.

16. Abstract

This report describes the development of an interaction data base and a numerical solution to the transport of baryons through an arbitrary shield material based on a straight ahead approximation of the Boltzmann equation. The code is most accurate for continuous-energy boundary values but gives reasonable results for discrete spectra at the boundary using even a relatively coarse energy grid (30 points) and large spatial increments (1 cm in H_2O). The resulting computer code is self-contained, efficient, and easy to use. The code requires only a very small fraction of the computer resources required for Monte Carlo codes.

17. Key Words (Suggested by Authors(s)) High-energy transport Data bases Neutron-nucleus Cross sections	18. Distribution Statement Unclassified—Unlimited Subject Category 93

19. Security Classif. (of this report) Unclassified	20. Security Classif. (of this page) Unclassified	21. No. of Pages 82	22. Price A05